MULTISCALE ANALYSIS OF WAVE PROPAGATION IN HETEROGENEOUS STRUCTURES

A Dissertation
Presented to
The Academic Faculty

by

Filippo Casadei

In Partial Fulfillment
of the Requirements for the Degree
Doctor of Philosophy in
Aerospace Engineering

School of Aerospace Engineering
Georgia Institute of Technology
August 2012

MULTISCALE ANALYSIS OF WAVE PROPAGATION IN HETEROGENEOUS STRUCTURES

Approved by:

Professor Massimo Ruzzene, Advisor
School of Aerospace Engineering, and
School of Mechanical Engineering
Georgia Institute of Technology

Professor Michael J. Leamy
School of Mechanical Engineering
Georgia Institute of Technology

Professor Julian J. Rimoli
School of Aerospace Engineering
Georgia Institute of Technology

Professor George Kardomateas
School of Aerospace Engineering
Georgia Institute of Technology

Professor Dewey H. Hodges
School of Aerospace Engineering
Georgia Institute of Technology

Date Approved: June 29 2012

To my family

ACKNOWLEDGEMENTS

I would like to express my deepest gratitude to my advisor Dr. Massimo Ruzzene for his trust and extraordinary guidance throughout my doctoral study. Since I started as a visiting student he has been a constant source of inspiration both professionally and personally. I am particularly grateful for his efforts in providing me with challenges and opportunities that constantly motivated me to improve. The path toward this doctoral degree would not have been so fascinating without an advisor like him.

A special thank is for Dr. Julian Rimoli for his invaluable support, technical guidance, and constant enthusiasm that were instrumental for the completion of the present work. As I always say, I only wish you had joined the department a bit earlier.

I have also greatly appreciated the time dedicated by the committee members for the careful revision of this thesis, and for their critical comments that contributed to greatly improve this work.

I must thank all my current and former labmates for the beautiful time spent together both inside and outside the Vibration and Wave Propagation Lab.

The achievement of this doctoral degree would not have been possible without the incredible patience and tremendous support that I received from my wife Maria. Since the beginning, she supported my decision to join the Ph.D. program at Tech and she decided to follow me along this journey. I dedicate this thesis to her and to my son Pietro whom I also thank for always providing laughter and joy.

A huge thank, and a big hug, goes to all the friends that shared with me many beautiful moments and sustained me during the inevitable hard times. I am deeply grateful for the privilege of having shared these years with you all.

TABLE OF CONTENTS

LIST OF TABLES

LIST OF FIGURES

SUMMARY

The analysis of wave propagation in solids with complex microstructures, and local heterogeneities finds extensive applications in areas such as material characterization, structural health monitoring (SHM), and metamaterial design. Within continuum mechanics, sources of heterogeneities are typically associated to localized defects in structural components, or to periodic microstructures in phononic crystals and acoustic metamaterials. Numerical analysis of this class of solids often requires computational meshes which are refined enough to resolve the wavelengths of propagating waves and to properly capture the fine geometrical features of the heterogeneities. It is common for the size of the microstructure to be small compared to the dimensions of the structural component under investigation, which suggests multiscale analysis as an effective approach to minimize computational costs while retaining predictive accuracy.

The objective of this research is to develop a multiscale framework for the efficient analysis of the dynamic behavior of heterogeneous solids. The proposed method, called Geometric Multiscale Finite Element Method (GMsFEM), is based on the formulation of multi-node elements with numerically computed shape functions. Such shape functions are capable of explicitly modeling the geometry of heterogeneities at sub-elemental length scales, and are computed to automatically satisfy compatibility of the solution across boundaries of adjacent elements. Numerical examples first illustrate the approach and validate it through comparison with available analytical and numerical solutions. The developed methodology is then applied to the analysis of periodic media, structural lattices, and phononic crystal structures. Numerical predictions for the latter are validated with experimental measurements. Finally,

GMsFEM is exploited to study the interaction of guided elastic waves and defects in plate structures. Both two- and three-dimensional analyses correlate the computed scattering patterns to the relevant geometrical feature of damage. The broad range of considered applications show that the developed multiscale strategy is systematic, self-consistent and easy to implement. Such characteristics are extremely attractive to expand the method to nonlinear and multi-physics problems, and make GMsFEM a possible candidate for integration as part of commercial finite element softwares.

CHAPTER I

INTRODUCTION

1.1 Overview

The problem of elastic wave propagation in heterogeneous media is receiving increasing attention among different research communities for its promising applications in several areas of science and engineering. For example, ultrasonic guided waves have shown great potential as part of non-destructive testing (NDT) techniques. Extensive research is also devoted to the analysis and design of phononic crystals and acoustic metamaterials for wave propagation control. These engineered assemblies feature a periodic microstructure that exhibits properties not observed in nature or in their constituents. Interesting wave phenomena are typically associated with material and structural heterogeneities or periodic modulations of stiffness and inertial properties. The spatial scale of the property modulations determines the scale and frequency range of application of acoustic devices that take advantage of such properties. Also, the size of damage in critical structural components dictates the spatial and temporal scales that must be resolved for the development of accurate and reliable NDT strategies.

Numerical investigations rely on the simulation of wave propagation and the waves' interaction with material heterogeneities often occurring at smaller spatial scales. The accuracy of such simulations requires computational meshes that are refined enough to resolve the wavelength of propagating waves and to properly capture the small geometrical features of the heterogeneities. Typically, the length scale characterizing localized imperfections or periodic microstructures is small compared to the global size of the structural component, and often smaller than the shortest wavelength of

deformation. Hence, the size of the spatial discretization is dictated by the size of the microstructure, which may result in high memory and CPU requirements. The advent of an efficient simulation environment for the analysis of heterogeneous solids could significantly aid the development of more reliable NDT procedures, and the design of novel acoustic metamaterials. To this end, the formulation of a robust and systematic numerical tool is particularly appealing. Such a tool could be also extended to nonlinear or multi-physics simulations, and eventually implemented within commonly available finite element (FE) packages. The remaining sections of this chapter will discuss the peculiarities of the physical phenomena under investigation, with particular emphasis on the critical computational challenges that still need to be addressed.

1.2 Wave propagation in periodic solids

1.2.1 Definition and applications of periodic media

Periodic media are defined as heterogeneous domains characterized by a recursive pattern obtained through the translation in space of a fundamental unit cell or representative volume element (RVE). Figure 1.a illustrates the periodic structure of a graphene sheet, while Fig. 1.b shows periodic honeybee cells as examples of periodic patterns commonly found in nature. In contrast, Fig. 1.c,d illustrate a metallic honeycomb structure and a microstructured metallic foam as examples of man-made periodic systems of engineering interest. Extensive research is devoted to the analysis and design of periodic structures for wave management applications [109]. Such assemblies may in fact exhibit interesting wave propagation properties such as bandgaps [74, 97, 109], response directionality [112, 113, 117], left-handedness [108], and negative acoustic refraction [121], all of which can be employed for the design of acoustic devices operating over a broad range of frequencies and length scales. The application of such concepts to the design of filters, waveguides, logic ports, and ultrasonic transducer

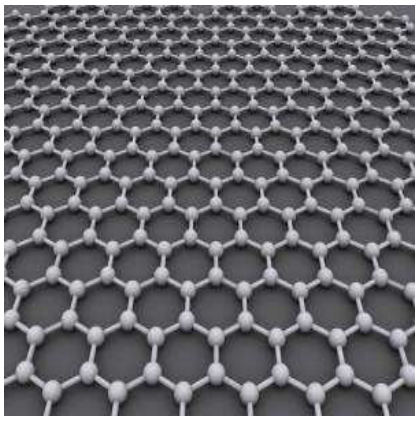

(a) Periodic structure of graphene

(b) Hexagonal honeycomb cells

(c) Metallic honeycomb

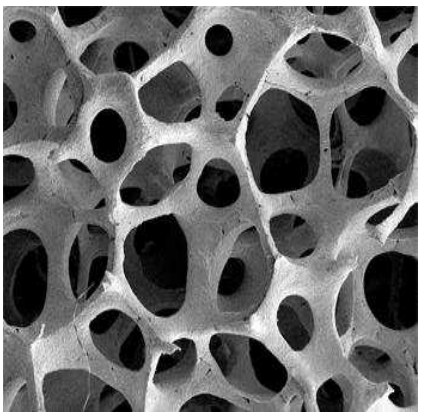

(d) Microstructure of stainless steel

Figure 1: Examples of periodic media and micro-structured materials.

arrays can, for example, be used to perform a variety of acoustics-based signal processing functions at frequencies where electronics suffer from severe power limitations. In conjunction to telecommunication and signal processing, potential implications of the "acoustic wave guiding" technology include among others active sensing of structural integrity [114], and dissipation of high frequency modes of vibration to enhance vehicle performance or stealth [32]. Other novel structural configurations may be exploited for devices which exhibit acoustic super-lensing, super-focusing and/or cloaking characteristics [108, 121]. Unusual wave properties of the kind mentioned above are associated with material and structural heterogeneities, which mostly correspond to periodic modulations of stiffness and inertial properties. As shown in Fig. 2.a,

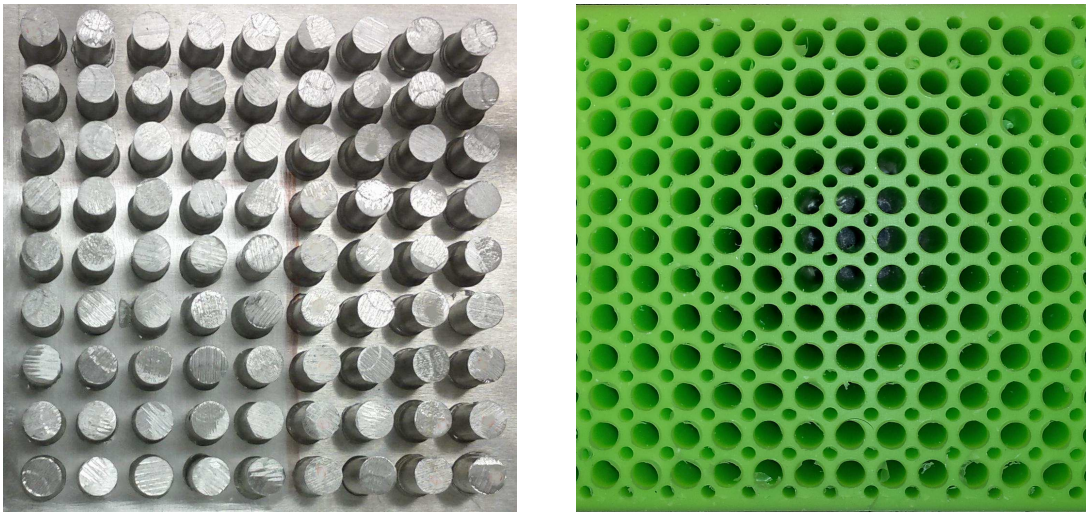

(a) (b)

Figure 2: Example of materials with periodic impedance modulations (a), and solid with periodic microstructures (b).

such modulations may result from the periodic dispersion of inclusions of different materials within a matrix [109, 113], or from the microstructural configuration of a given assembly [117, 125], schematically illustrated in Fig. 2.b. The spatial scale of the property modulations dictates the range of frequencies at which unusual wave guiding properties occur, and therefore determines the scale and frequency range of application of a device that takes advantage of such properties. As previously discussed, the direct numerical simulation of wave propagation in periodic components or microstructured materials constitutes an intrinsically multiscale problem. An overview of the major efforts aimed at reducing the time and memory requirements of wave simulations in periodic solids is reported in the following section.

1.2.2 Multiscale analysis of periodic systems

Many techniques developed to date for the simulation of waves propagating in microstructured solids have the objective of describing the overall behavior of an heterogeneous system in terms of equivalent properties. The analysis is then conducted with the same tools used for homogeneous media. The definition of equivalent properties

for multiscale heterogeneous solids is typically performed through classical homogenization techniques [18, 25, 75, 104]. For instance, composite materials constitute a classical example of heterogeneous media commonly analyzed in terms of effective properties based on rules of mixtures [56] or other averaging procedures such as the classical lamination theory for multilayered plates. Also, periodic structural lattices have been studied through homogenization strategies where the spatial periodicity is exploited to obtain dynamic equilibrium equations in the Fourier domain [15, 84, 85, 86, 103]. Homogenization methods are often based on the fundamental assumption that the system must be periodic, and are known to provide accurate results if the macroscopic fields are constant or slowly varying within a single representative volume element. Typically, such requirements hold far from the boundaries of the computational domain and when the size of the microstructure is significantly smaller than the wavelength of deformation.

In order to overcome the limitations of homogenization-based techniques, significant research effort is focused on the development of higher order expansion methods capable of describing the high frequency response and the dispersive behavior of periodic media. For example, Fish et al. [44, 46, 48, 49, 50, 51] developed a multi-grid method for wave problems in heterogeneous media characterized by microstructures whose size is comparable in magnitude to that of the structural details or the wavelength of a traveling signal. Working on the dynamic behavior of composite materials, Sun et al. [122] introduced the concept of effective stiffness for the dynamic analysis of laminated media and unidirectional fiber-reinforced composites. In this work high order expansions of the displacement field of each lamina are exploited to compute the dispersion properties of composite plates. Similarly, Murakami et al. [98, 99, 100] proposed a mixed theory based on high-order continuum models to simulate elastic wave dispersion in fiber-reinforced composites. Despite the outstanding achievements in the field of high-order homogenization, a definitive computational methodology for

the calculation of the dispersion properties of complex, non-periodic, microstructures is still not available. Significant advances were obtained more recently by McDevitt et al. [87, 88, 89] who proposed a multiscale method based on a two-field variational formulation for the calculation of the phase and group velocity spectra in laminated media and a fiber-reinforced composites. This approach is known to provide accurate results up to the point where the wavelength approaches the size of a representative volume element. Such spatial precision allows the correct description of the first wave modes and begins to deteriorate at higher frequencies. More recently, a reduced Bloch mode expansion method has been introduced by Hussein [63] for the calculation of band diagrams of periodic solids with complex microstructures. The method, based on a FE discretization of the unit cell, employs a limited number of Bloch eigenmodes to project the fine-scale eigenvalue problem onto a reduced subspace selected within the irreducible Brillouin zone at high symmetry points. Being in line with the well known concept of modal analysis, the approach maintains accuracy while reducing the computation time even if the calculation of the reduced basis requires explicit solution of the local eigenvalue problem.

1.3 Guided wave-based structural health monitoring

1.3.1 Concept of GW non-destructive testing

An important aspect in the life-cycle design of structural components is the accurate determination of the presence, size and location of damage. Among different approaches used for the monitoring of structural integrity, guided waves (GW) have shown great potentials for their capability to scan relatively wide portions of a structure and for being sensitive to a variety of damage types [4, 8, 110, 118]. As theorized in [126], Lamb waves inspection techniques should hierarchically perform: (1) qualitative indication of the occurrence of damage (detection), (2) quantitative assessment of the position of damage (localization), (3) quantitative estimation of the

severity of damage (quantification), and (4) estimation of residual service life and structural safety (prediction). Typical defects encountered in structural components include cracks and corrosion in metallic materials, and porosity, delaminations, matrix and/or fiber cracking in composites, as shown in Fig. 3. The development of

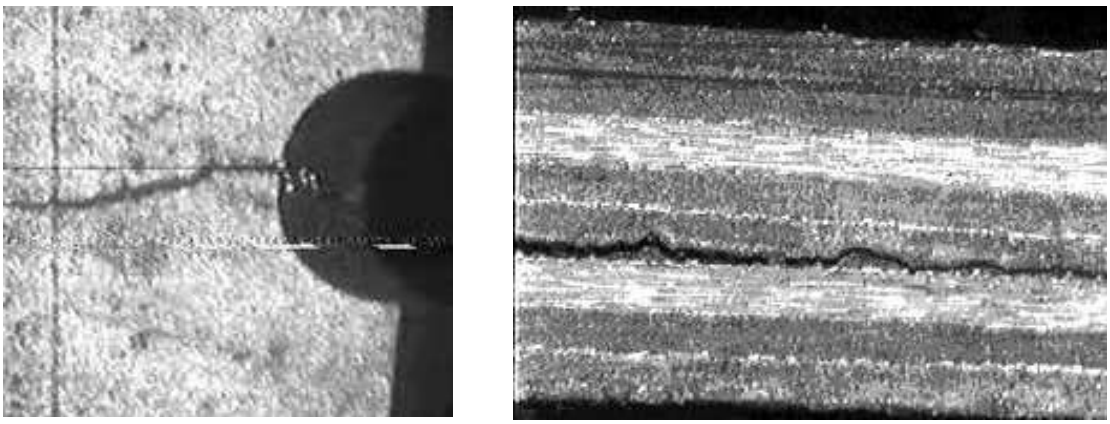

(a) (b)

Figure 3: Typical crack observed in a metallic material (a), and delamination in a composite plate (b).

effective GW-based inspection techniques that not only detect damage but also provide some quantitative measure of its severity, relies on numerical simulations which investigate the interaction between propagating waves and defects of different type, orientation and size. Specifically, numerical simulations of wave propagation play a key role for the development of novel damage detection algorithms and are useful to support the interpretation of experimental measurements. An overview of the most relevant research contributions in the field of numerical modeling of wave-damage interaction is presented in the following section.

1.3.2 Numerical modeling of wave-damage interactions

Due to their relatively simple mathematical formulation and the possibility to be applied to an extremely broad class of engineering problems, finite difference (FD) and finite element (FE) based methods have been used by several authors for the analysis of guided waves [27]. Most of the past research, conducted during the 90's,

is based on transient simulations in the time domain and is devoted to the study of the basic physics related to the generation and propagation of guided waves in plates [8, 9, 19, 123, 129]. These studies have mostly supported the development of experimental procedures for the inspection of plate-like structures. More recently, numerical simulations have been used for the characterization of different types of damage. Many implementations are developed for wave scattering problems from different damage configurations in metallic structures. Particularly relevant are the works by Fromme [52] who investigated numerically and experimentally the scattering of the first antisymmetric Lamb wave mode (A_0) at a circular hole in isotropic homogeneous plates. Also, Diligent et al. [39, 40, 81, 82] analyzed the interaction between the fundamental Lamb modes with various defects in an aluminum plate using two-dimensional (2D) FE models. When such domain discretization techniques are employed for wave propagation simulations, the size of the numerical grid is generally chosen to spatially resolve the propagation of the waves with the shortest wavelengths [7, 94]. However, when simulating the interaction of propagating waves with small defects, the element size is dictated by the need to accurately model the geometry of the damaged area. Consequently the model size grows as the defect length decreases.

To overcome the intrinsic limitation of FD/FE methods, various techniques have been developed and applied to study specific aspects of Lamb waves interaction with damage. Several methods, known as "global-local" methods, are based on the idea of coupling analytical solutions and FE models to compute the far-wavefield scattered by a localized damage located in the discretized region. Applications of global-local techniques to the problem of wave scattering from cracks and inclusions in plates can be found in the early works by Koshiba et al. [72], Karim and Kundu [69], and Al-Nassar et al. [6]. More recently, Moulin et al. [96] proposed a coupled finite element-normal modes expansion method for the analysis of Lamb waves generated by integrated

transducers in composite plates. The use of analytical solutions in conjunction with a discretization approach also constitute the basis of the Strip Element Method (SEM) developed by Liu and Achenbach [76] and applied by various authors to elastic waves scattering problems [77, 78]. Similar developments that employ the boundary integral equation method (BIEM) and the boundary element method (BEM) have also been proposed by Galan and Abascal in [53], and Rose et al. [36, 37, 133]. All these approaches allow to investigate very effectively the problem of wave scattering from imperfections since the total number of unknowns is significantly reduced by the use of analytical expressions. The main drawback is the lack of availability of exact expressions for realistic structural configurations as testified by the total absence of results available for three-dimensional (3D) structural components. An attempt to explicitly model the damage properties while maintaining computational efficiency is presented in [58], where a Bridging Scale Method (BSM) [67, 79, 124] is used to couple a coarse mesh with an overlapping fine scale mesh defined only over a limited portion of the domain. Bridging conditions between the two non-matching grids avoid the onset of spurious waves at the interface. However their implementation requires the computation, at each time step, of convolution integrals which significantly limits the performance of the method. Based on this experience, a formulation of the same method in the frequency domain was developed in [31]. Convolution terms are converted into algebraic expressions, but significant improvements were not observed due to the requirement to solve an asymmetric complex linear system of equations at each frequency step.

1.4 Multiscale analysis of heterogeneous media

1.4.1 Problem formulation

In the last decade, several multiscale strategies have been proposed to facilitate the study of heterogeneous materials involving multiple scales [68]. Such materials typically feature a macroscopic or global scale (L) which identifies the length scale of the material's application, and a microscopic or local scale (δ) defining the underlying microstructure. As shown in Fig. 4.a, if the ratio between the local and global length scales is small (i.e., when $\varepsilon = \delta/L \lll 1$), the problem is said to have "scale separation" and homogenized models can be successfully applied. In other circumstances for which $\varepsilon \lesssim 1$ it is not possible to identify a clear separation between the global and local scales, as shown in Fig. 4.b. Heterogeneities characterized by one to two orders of magnitude smaller than the global scale belong to the latter class of multiscale problems - the one considered in this thesis. The task of multiscale modeling is to design combined macroscopic-microscopic computational methods that are more efficient than solving the full microscopic model, and at the same time give the information needed to the desired accuracy.

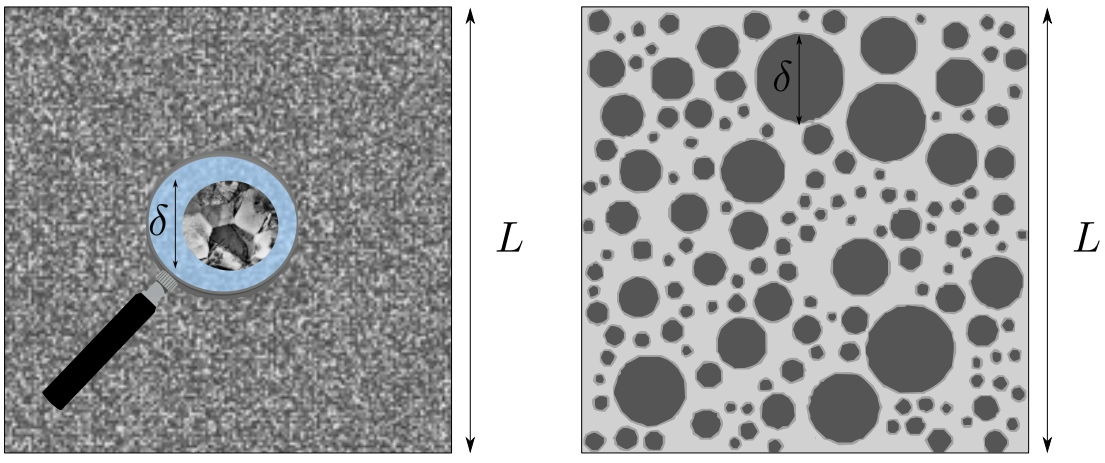

(a) (b)

Figure 4: Heterogeneous materials with (a) and without (b) scale separation.

1.4.2 Overview of multiscale methods

When the global and local scale are fully separated, numerical methods based on global-local analysis are employed. Global-local techniques [34, 47, 95, 102] are typically based on a hierarchical decomposition of the solution into a global or coarse scale, and a local or fine-scale component. A finite element description of the computational domain is commonly used to resolve the global scale of the problem, while the local properties are resolved by means of multiscale enrichment functions that complement the finite element basis. In most of the early attempts, reviewed in [95, 102], global functions describing closed form analytical solutions, such as crack tip asymptotic fields [57] or discontinuities in shear bands [22], were used to enrich the finite element approximation. Such global-enrichment methods are extremely efficient in enhancing the FE solution with very few fine scale functions but, on the negative side, they often tend to generate dense matrices.

More recently, local enrichment methods have been proposed to compute the fine scale functions at the element level. Local enrichment functions have been used to embed discontinuous strains [23, 45], curvatures [21] and displacements [13, 115]. Also, methods based on mathematical homogenization [14, 25, 59] can be interpreted as local enrichment methods whereby the global and local solutions correspond to the zero- and first order expansions of the unknown field. An attractive feature of this class of multiscale methods is the possibility of condensing the fine scale information by means of a static condensation procedure or through the definition of effective properties that are used as inputs of the coarse-scale model. For these reasons, this class of scale bridging is often denoted as "serial," or "parameter-passing." On the downside, such techniques tend to significantly approximate the fine-scale properties of the problem, and only an averaged response is effectively passed to the global model.

When the characteristic length of the microscopic features is not small compared

to the macroscale (Fig. 4.b), constant communication between two scales and special strategies for passing the necessary informations from one scale to another are required. To this end, strong coupling methods [64], and multi-level coupling methods [29, 55] implement a concurrent resolution of multiple scales throughout the entire simulation, and therefore are often denoted as "concurrent," "embedded" or "handshaking" methods. The extended finite element method (XFEM) [20, 24, 41] and the generalized finite element method (GFEM) [119, 120] are also examples of multiscale strategies based on the partition of unity method (PUM) first introduced by Melenk and Babuska in [90]. These techniques use discontinuous enrichment functions in order to introduce discontinuities into the displacement field with only a relatively small number of additional DOFs. Such techniques significantly simplify the meshing processes, but they do not completely incorporate the multiscale aspect induced particularly at the cracks tip. Furthermore in [73] it is shown that PUM - based methods provide very accurate results at low wave resolutions for the Helmholtz equation, but suffer from severe ill-conditioning that make the method highly ineffective. In the discontinuous enrichment method (DEM) [43], the standard FEM space is enriched within each element by additional non-conforming functions. The degrees of freedom that are associated with the enrichment are statically condensed on the element level so that no additional unknowns result through the enrichment. However, Lagrange multipliers are introduced in order to enforce continuity between elements. It is interesting to note that in the XFEM/GFEM/PUM, standard FEM unknowns and the enrichment DOFs are present in the final system of equations. Similarly, in the DEM both standard FEM unknowns and Lagrange multipliers characterize the DOFs retained in the final system. The number of such additional DOFs explicitly retained is a critical parameter that can potentially compromise the efficiency of such methods. Furthermore, in estimating the cost-effectiveness of such methods, it is important to take into account the effort for the static condensation and the construction of

the Lagrange multiplier space in the DEM, or the effort for computing the enriched moving-least squares functions in XFEM.

1.4.3 The multiscale finite element method

A different approach to bridge micro and macroscopic scales within a FE framework is based on the definition of multiscale shape functions. Such techniques, commonly known as multiscale finite element methods (MsFEM) [61, 62], incorporate the fine-scale features into the definition of the shape functions rather than enriching the polynomial FE basis.

Building on the pioneering work by Babuska et al. [16, 17], MsFEM was originally developed within the applied math community for the analysis of elliptic problems with rapidly oscillating coefficients. The basic idea of the method is to modify the basis functions in the finite element space by solving, for each element, the original microscale problem with homogeneous right hand side and suitable boundary conditions. The small-scale information is then brought to the macroscopic level through the coupling of the global stiffness matrix. A similar idea was also suggested by [80] for solving Helmholtz equations by using oscillatory functions as basis functions. Moreover, the use of basis functions represented by free-space solutions of the homogeneous equations is reminiscent of Trefftz approximations [65, 66, 71].

This method has been applied to study complex flows in highly heterogeneous porous media [2, 3, 35, 42], and more recently, extended to static elastic [131], and elasto-plastic [130, 132] problems in mechanics. The major limitation of MsFEM methods resides in the fact that the use of common elements, such as quadrilaterals and triangles, provide limited ability to model arbitrarily complex shapes. From the known literature, it is also not clear if the idea behind such methods can be applied to general three-dimensional elements or if it can be implemented for time-dependent dynamic analyses.

1.5 Motivations

The present research effort is devoted to the development of a multiscale analysis tool inspired by the MsFEM concept, that can be systematically applied for the calculation of the dynamic response of solids with periodic or localized heterogeneities of arbitrary shape in two and three spatial dimensions. From the previous discussion, it is evident that wave propagation simulation in solids and structures with multiscale features remains a challenging task even for modern computational resources. Such limitations characterize the intrinsic nature of grid based methods, such as FE and FD methods, and are not completely overcome by recent developments in multiscale analysis. Furthermore, many multiscale methods are developed for highly specialized problems and therefore tend to remain confined within the academic community. Instead, several industrial applications could benefit from the development of fast and reliable numerical techniques for the simulation of wave phenomena in heterogeneous structures. For instance, in the context of wave-based non-destructive methods, numerical simulations facilitate the interpretation of experimental measurements and support the development of algorithms for damage detection. Furthermore, simple and robust multiscale simulations can unveil fundamental aspects regarding the interactions of elastic waves and defects in advanced structural components. The present research is also motivated by the growing interest within the research community toward the design of acoustic metamaterials for wave management.

1.6 Objectives

In response to such needs, the objective of this research is to develop a geometric multiscale finite element method (GMsFEM) for the efficient analysis of wave propagation in materials with internal damage, and microstructured media with periodic heterogeneities. The proposed GMsFEM extends the current multiscale modeling

capabilities by combining the idea of multi-node elements to the concept of numerical shape functions proper of MsFEM methods. In the present approach, multiscale shape functions for arbitrarily shaped elements are derived in the process of minimizing the global strain energy of the problem. This allows describing both the elastic and inertial properties of arbitrary multiscale elements in terms of limited nodal information. In addition, this work derives three-dimensional (3D) multiscale elements based on the proposed GMsFEM formulation and describes the compatibility between multiscale elements and the remaining elements of the numerical grid.

The free wave propagation properties of periodic solids and structural lattices are first analyzed. While many multiscale analysis tools provide accurate results exclusively in the long wavelength regime, GMsFEM provides a systematic approach to tailor the required degree of accuracy according to the needs of the specific application. For instance, very efficient multiscale elements can be used for applications in the low and medium frequency range when the wavelengths of deformation are large compared to the unit cell of the medium. Additionally, the use of multiscale elements with increasing number of global information allows modeling localized deformations within the RVE that leads to fully converged solutions at higher frequencies. This becomes a major advantage since some peculiar phenomena of periodic structures, such as bandgaps and wave steering, typically characterize the dispersion properties of higher wave branches. The proposed GMsFEM is finally exploited for the analysis of a phononic crystal plate, and predictions are compared with the experimental estimation of its dispersion properties.

The GMsFEM is also exploited for the analysis of wave propagation in damaged plate-like structures. The objective is to extract information regarding the scattering behavior associated with several defect configurations. Particularly relevant is the calculation of scattering directivity diagrams associated with partial-depth defects in

metallic plates. Due to the intrinsic three-dimensional nature of the problem, simulations are conducted using a comprehensive multiscale FE code developed in-house for the implementation of both 2D and 3D multiscale elements. Parametric analyses are conducted for varying damage size, orientation, and depth relative to the plate thickness. Of particular interest is the possibility of defining libraries of multiscale elements with embedded defects to be used in conjunction with FE packages to analyze different damage configurations without re-meshing the entire domain.

1.7 Organization of the work

This thesis is organized in five chapters including this introduction. Chapter II introduces the numerical formulation of GMsFEM by describing the concept of multiscale elements, multiscale shape functions, and their implementation. Particular emphasis is given to the problem of inter-element compatibility, especially related to the formulation of three-dimensional multiscale elements. Numerical examples are presented to illustrate the approach. In Chapter III, the proposed GMsFEM is applied for the analysis of periodic heterogeneous media such as materials with periodic inclusions and structural lattices. Numerical examples illustrate the possibility of reducing the computational costs for the calculation of the dispersion relations of periodic solids. Also, the analyses highlight the major shortcomings of the method. The dispersion properties of a phononic crystal are computed and experimentally validated through laser vibrometry measurements. Chapter IV applies the proposed multiscale strategy to the interaction of elastic waves and small defects in otherwise homogeneous structures. Numerical results obtained with GMsFEM are first compared with analogous FE solutions to validate the modeling approach. Several parametric studies are then conducted to characterize the scattering patterns due to defects in both two- and three- dimensional structures. Finally, Chapter V summarizes the current research findings and provides recommendations for future developments.

CHAPTER II

THE GEOMETRIC MULTISCALE FINITE ELEMENT METHOD

2.1 Overview

This chapter presents the geometric multiscale finite element method (GMsFEM) developed for estimating the dynamic response of materials and structures with localized or periodic heterogeneities. The method is based on the formulation of multi-node elements of arbitrary shape that model geometrical imperfections without requiring localized mesh refinements. Such elements are equipped with a set of basis functions that are computed numerically by means of an auxiliary finite element discretization of the element itself. An extensive section is dedicated to the issue of compatibility between adjacent elements, and a rigorous formalism is presented in order to formally address this issue. In the final part of this chapter, numerical examples are presented to illustrate the approach.

2.2 Formulation

2.2.1 Multiscale energy functional

Consider the discretization of an elastic body into the assembly of non-overlapping finite elements. The computational domain is discretized using both regular finite elements (quadrilaterals, tetra, bricks, etc.), and elements characterized by an arbitrary number of nodes, here denoted as multiscale elements (MSE). Such elements are exploited to model localized geometrical details with an irregular shape as shown in Fig. 5. The field variables associated with the nodes of each MSE are interpolated within the element's domain by means of an auxiliary fine-scale FE mesh, shown in

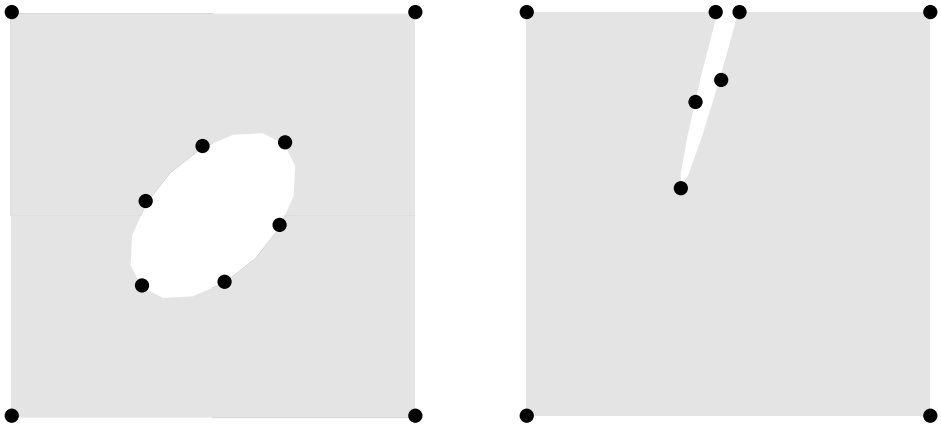

(a) (b)

Figure 5: Example of multiscale elements with an internal inclusion (a), and with a generic irregular shape (b).

Fig. 6.a, that discretizes the region within the element itself. The degrees of freedom (DOFs) associated with such local mesh are denoted as *local DOFs* or alternatively *fine-scale DOFs* ($\boldsymbol{q}$) because they describe the behavior of the system at sub-elemental length scales. On the other hand, the degrees of freedom associated with the global nodes of each MSE and the DOFs of other finite elements are referred to as *global DOFs* or similarly *coarse-scale DOFs* ($\boldsymbol{d}$). They are used to represent the macroscopic behavior of the system. A schematic representation of these two sets of nodes (and associated DOFs) is shown in Fig. 6.a.

The strain energy $\mathcal{U}$ of the system under consideration is expressed in terms of contributions derived from local elements (within each MSE) and elements that discretize the uniform portion of the domain:

$$\mathcal{U} = \frac{1}{2} \begin{bmatrix} \boldsymbol{d} & \boldsymbol{q} \end{bmatrix} \begin{bmatrix} \boldsymbol{K}_{dd} & \boldsymbol{K}_{dq} \\ \boldsymbol{K}_{qd} & \boldsymbol{K}_{qq} \end{bmatrix} \begin{bmatrix} \boldsymbol{d} \\ \boldsymbol{q} \end{bmatrix} \tag{1}$$

where $\boldsymbol{K}_{dd}$ and $\boldsymbol{K}_{qq}$ indicate partitions of the global stiffness matrix associated with the global and local DOFs respectively. The coupling matrix $\boldsymbol{K}_{dq}$ relates the nodes of the local mesh that are adjacent to the nodes of the global discretization. Equation (1)

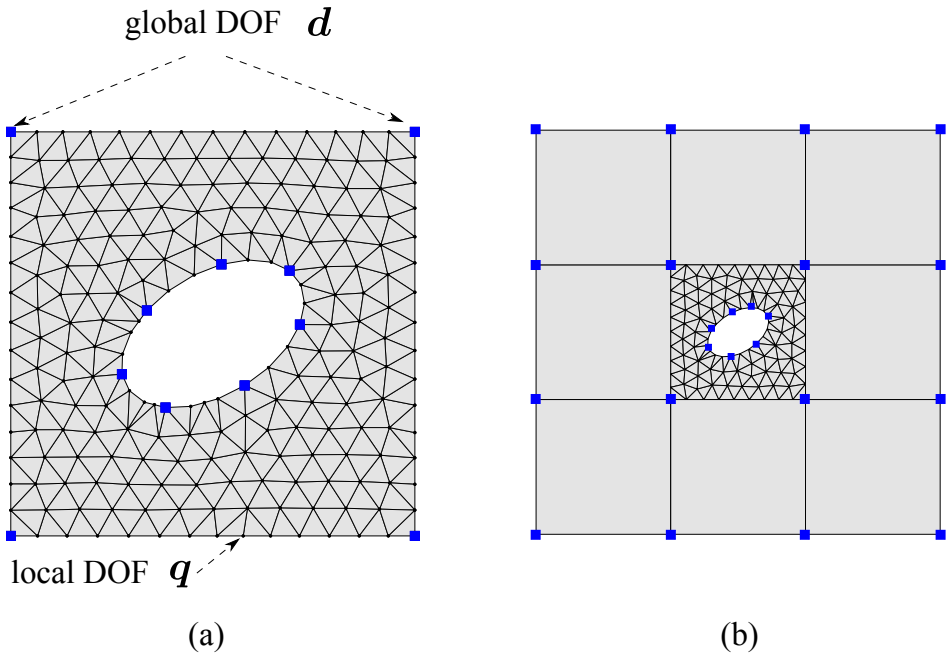

Figure 6: Fine-scale discretization of a multiscale element (a) with global (blue square markers), and local (small • markers) nodes, and coupling with standard finite elements (b).

can be rewritten in the following compact form as:

$$\mathcal{U} = \frac{1}{2}\boldsymbol{u}^T \boldsymbol{K}\, \boldsymbol{u} \tag{2}$$

where $\boldsymbol{u} = [\boldsymbol{d} \quad \boldsymbol{q}]^T$, and $\boldsymbol{K}$ is the global stiffness matrix of the system that is assembled using standard FE procedures. This formalism is similar to the one commonly adopted in model reduction techniques, such as Guyan reduction [60], where a larger group of slave DOFs is expressed in terms of a smaller group of master DOFs. The major difference with the methodology proposed herein lies in the fact that the resulting fine-scale mesh is in general not conforming to the elements of the global discretization, as illustrated in Fig. 6.b. A discretization is a conformal mesh of the computational domain if all elements of the mesh have a non empty interior, and if the intersection between any two elements is either an empty set, a point, an edge or a face of both elements [54]. Physically, conformity assures that no gaps or material overlaps occur when the mesh is subjected to external loads.

2.2.2 Constraint equations for element compatibility

In order to recover the required continuity of displacements across adjacent elements, the fine-scale DOFs are required to satisfy a set of linearity constraints along the boundaries of the MSE that are shared with adjacent linear finite elements. Such condition is enforced by means of multipoint constraint equations of the form:

$$\boldsymbol{B}_d\,\boldsymbol{d} + \boldsymbol{B}_q\,\boldsymbol{q} = \boldsymbol{0} \tag{3}$$

where $\boldsymbol{B}_d$ and $\boldsymbol{B}_q$ are matrices of known coefficients used to express a relative value between the fine-scale and global DOFs. A vector of Lagrange multipliers $\boldsymbol{\lambda}$ is exploited to enforce the required constraint equations that are used to define the following augmented strain energy function:

$$\mathcal{U}^+ = \mathcal{U} + \boldsymbol{\lambda}^T\,(\boldsymbol{B}_d\,\boldsymbol{d} + \boldsymbol{B}_q\,\boldsymbol{q}) \tag{4}$$

The equations of motion are obtained through the definition of a total potential:

$$\Pi^+ = \mathcal{U}^+ - \mathcal{W} \tag{5}$$

where $\mathcal{W} = \boldsymbol{d}^T\boldsymbol{f}$ represents the work of external forces $\boldsymbol{f}$ applied to the global nodes of the model.

The stationary points of Π^+ with respect to the coarse-scale DOFs $\boldsymbol{d}$, the fine-scale DOFs $\boldsymbol{q}$, and the Lagrange multipliers $\boldsymbol{\lambda}$ are determined as:

$$\begin{aligned}
\frac{\partial\Pi^+}{\partial\boldsymbol{d}} &= \boldsymbol{K}_{dd}\,\boldsymbol{d} + \boldsymbol{K}_{dq}\,\boldsymbol{q} + \boldsymbol{B}_d^T\,\boldsymbol{\lambda} - \boldsymbol{f} = \boldsymbol{0}\\
\frac{\partial\Pi^+}{\partial\boldsymbol{q}} &= \boldsymbol{K}_{dq}^T\,\boldsymbol{d} + \boldsymbol{K}_{qq}\,\boldsymbol{q} + \boldsymbol{B}_q^T\,\boldsymbol{\lambda} = \boldsymbol{0}\\
\frac{\partial\Pi^+}{\partial\boldsymbol{\lambda}} &= \boldsymbol{B}_d\,\boldsymbol{d} + \boldsymbol{B}_q\,\boldsymbol{q} = \boldsymbol{0}
\end{aligned} \tag{6}$$

or in compact matrix form as:

$$\begin{bmatrix} \boldsymbol{K}_{dd} & \boldsymbol{K}_{dq} & \boldsymbol{B}_d^T \\ \boldsymbol{K}_{dq}^T & \boldsymbol{K}_{qq} & \boldsymbol{B}_q^T \\ \boldsymbol{B}_d & \boldsymbol{B}_q & \boldsymbol{0} \end{bmatrix} \begin{bmatrix} \boldsymbol{d} \\ \boldsymbol{q} \\ \boldsymbol{\lambda} \end{bmatrix} = \begin{bmatrix} \boldsymbol{f} \\ \boldsymbol{0} \\ \boldsymbol{0} \end{bmatrix} \tag{7}$$

Equation (7) represents the equilibrium equations of a system discretized with a non-conforming mesh where compatibility of displacements is enforced by the constraint equations expressed in Eq. (3).

The direct solution of the resulting system, although possible, may result in a challenging computational task due to the explicit presence of the fine-scale DOFs and the vector of Lagrange multipliers. Furthermore, in the context of dynamic simulations, the presence of Lagrange multipliers generates a singular mass matrix that gives rise to a system of differential algebraic equations whose solution is particularly demanding especially for simulations that involve a large number of unknowns. An alternative approach is presented in the following sections which illustrate how the fine-scale information can be brought to the global model through the definition of multiscale shape functions.

2.2.3 Multiscale shape functions

The equilibrium equations given by Eq. (7) constitute the starting point to define the interpolation operator for multiscale elements. This allows solving for the global DOFs $\boldsymbol{d}$ only without resolving the fine-scale. From the second line of Eqs. (7) it is possible to express $\boldsymbol{q}$ as:

$$\boldsymbol{q} = -\boldsymbol{K}_{qq}^{-1} \left(\boldsymbol{K}_{dq}^{T} \boldsymbol{d} + \boldsymbol{B}_{q}^{T} \boldsymbol{\lambda} \right) \tag{8}$$

Substituting Eq. (8) into the third of Eqs. (7) gives:

$$\boldsymbol{B}_{d} \boldsymbol{d} - \boldsymbol{B}_{q} \boldsymbol{K}_{qq}^{-1} \left(\boldsymbol{K}_{dq}^{T} \boldsymbol{d} + \boldsymbol{B}_{q}^{T} \boldsymbol{\lambda} \right) = \boldsymbol{0} \tag{9}$$

Thus the Lagrange multipliers are expressed in terms of the coarse-scale DOFs:

$$\boldsymbol{\lambda} = \left(\boldsymbol{B}_{q} \boldsymbol{K}_{qq}^{-1} \boldsymbol{B}_{q}^{T} \right)^{-1} \left(\boldsymbol{B}_{d} - \boldsymbol{B}_{q} \boldsymbol{K}_{qq}^{-1} \boldsymbol{K}_{dq}^{T} \right) \boldsymbol{d} \tag{10}$$

Substituting Eq. (10) back into Eq. (8) gives an explicit expression for $\boldsymbol{q}$ as a function of $\boldsymbol{d}$:

$$\boldsymbol{q} = -\boldsymbol{K}_{qq}^{-1} \left[\boldsymbol{K}_{dq}^{T} + \boldsymbol{B}_{q}^{T} \left(\boldsymbol{B}_{q} \boldsymbol{K}_{qq}^{-1} \boldsymbol{B}_{q}^{T} \right)^{-1} \left(\boldsymbol{B}_{d} - \boldsymbol{B}_{q} \boldsymbol{K}_{qq}^{-1} \boldsymbol{K}_{dq}^{T} \right) \right] \boldsymbol{d} \tag{11}$$

Equation (11) allows expressing the global state vector $\boldsymbol{u} = [\boldsymbol{d} \quad \boldsymbol{q}]^T$ in terms of $\boldsymbol{d}$ only:

$$\boldsymbol{u} = \begin{bmatrix} \boldsymbol{d} \\ \boldsymbol{q} \end{bmatrix} = \begin{bmatrix} \boldsymbol{I} \\ \boldsymbol{\Gamma} \end{bmatrix} \boldsymbol{d} = \boldsymbol{\mathcal{N}} \boldsymbol{d} \tag{12}$$

where

$$\boldsymbol{\Gamma} = -\boldsymbol{K}_{qq}^{-1} \left[\boldsymbol{K}_{dq}^T + \boldsymbol{B}_q^T \left(\boldsymbol{B}_q \boldsymbol{K}_{qq}^{-1} \boldsymbol{B}_q^T \right)^{-1} \left(\boldsymbol{B}_d - \boldsymbol{B}_q \boldsymbol{K}_{qq}^{-1} \boldsymbol{K}_{dq}^T \right) \right] \tag{13}$$

In Eq. (12), $\boldsymbol{\mathcal{N}}$ is an interpolation operator that maps the information available at the global nodes of the MSE onto the fine-scale. The inherent structure of matrix $\boldsymbol{\Gamma}$ reveals that the present approach resembles a static condensation of the fine-scale DOFs under the prescribed set of constraints. The first term in the expression of $\boldsymbol{\Gamma}$, i.e. $-\boldsymbol{K}_{qq}^{-1} \boldsymbol{K}_{dq}^T$, in fact can be recognized as the transformation matrix between master ($\boldsymbol{d}$) and slave ($\boldsymbol{q}$) DOFs in static condensation [60]. The remaining terms involving $\boldsymbol{B}_d$ and $\boldsymbol{B}_q$ define the constraint equations imposed to recover the desired inter-element compatibility. Such terms are introduced in order to formulate conformable elements when the fine-scale mesh is not conforming to the adjacent discretization. Due to the approximate nature of the multiscale shape functions, however, the Lagrange multiplier approach adopted herein provides only a necessary condition to enforce inter-element compatibility. A more extensive treatment on conformity of multiscale elements will be presented in the following section.

Similarly to what observed for static condensation, each column of the transformation matrix $\boldsymbol{\mathcal{N}}$ represents the static displacement of the fine-scale mesh obtained by imposing a unit displacement to one global DOF of the MSE when all other external nodes are constrained and when the local DOFs satisfy the desired constraint equations. Because of the local support of the FE basis functions, only the global nodes that belong to a specific MSE give a non-zero contribution to each column of $\boldsymbol{\mathcal{N}}$. Examples of GMsFEM multiscale basis functions for the multi-node element shown in Fig. 5.b are illustrated in Fig. 7. Such displacements provide the means to

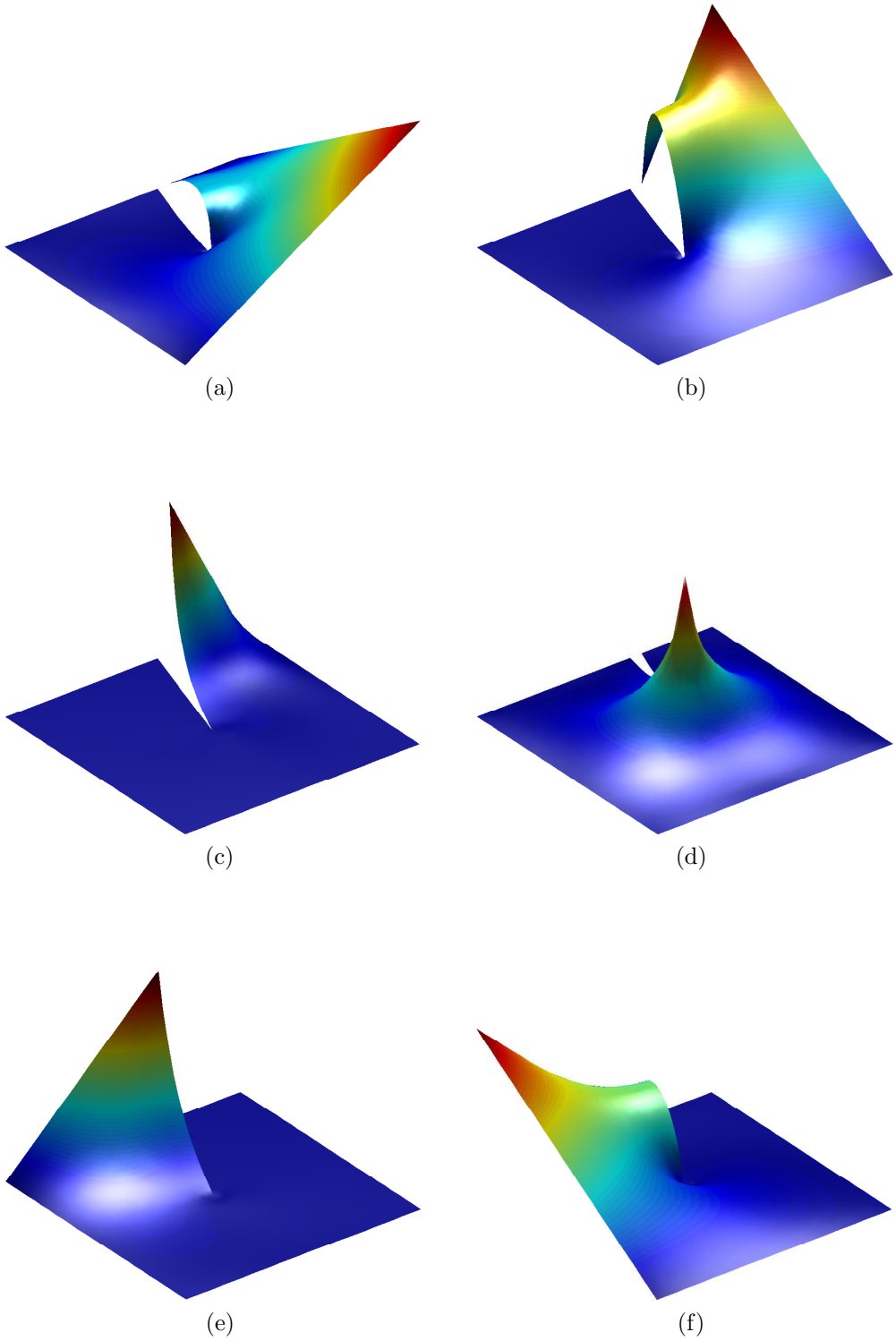

Figure 7: Selected multiscale shape functions of a MSE with generic shape. For the sake of clarity, MSF are represented as out-of-plane surfaces.

interpolate information available at the global scale onto the entire domain of multiscale elements and are therefore denoted as the multiscale shape functions (MSF), or basis functions of the MSE. This observation highlights the similarity between the proposed approach and the multiscale finite element method (MsFEM) originally proposed by Hou et al. [61, 62], and recently applied by Zhang et al. [131, 132] to static elasticity problems under the name of extended-MsFEM (EMsFEM). As shown in Fig. 7 the present method generalizes the intuition by Hou et al. to elements with arbitrary shapes for which MsFEM and EMsFEM, in their original formulations, do not seem to apply. The proposed derivation of the GMsFEM equations also demonstrates how both MsFEM and EMsFEM can be interpreted within the framework of a constrained static condensation method.

2.2.4 Multiscale mass and stiffness matrices

The calculation of $\boldsymbol{\mathcal{N}}$ allows expressing the local matrices of multiscale elements in terms of the corresponding fine-scale mass and stiffness matrices. Consider the general j^{th} MSE for which $\boldsymbol{\mathcal{N}}_j$ represents the portion of $\boldsymbol{\mathcal{N}}$ that involves only the relevant coarse-scale DOFs $\boldsymbol{d}_j$ that contribute to the associated multiscale basis functions. The strain and kinetic energies of the MSE can be expressed as a function of the global unknowns as:

$$\mathcal{U}_j = \frac{1}{2}\boldsymbol{d}_j^T \boldsymbol{K}_j \boldsymbol{d}_j \quad \text{and} \quad \mathcal{T}_j = \frac{1}{2}\dot{\boldsymbol{d}}_j^T \boldsymbol{M}_j \dot{\boldsymbol{d}}_j \tag{14}$$

or in terms of the entire fine-scale state vector $\boldsymbol{u}_j$ of the underlying micro-scale mesh as:

$$\mathcal{U}_j = \frac{1}{2}\boldsymbol{u}_j^T \boldsymbol{K}^f \boldsymbol{u}_j \quad \text{and} \quad \mathcal{T}_j = \frac{1}{2}\dot{\boldsymbol{u}}_j^T \boldsymbol{M}^f \dot{\boldsymbol{u}}_j \tag{15}$$

where $\boldsymbol{K}^f$ and $\boldsymbol{M}^f$ are respectively the stiffness and mass matrices associated with the local mesh within the MSE and are computed using standard FE procedures. Substituting Eq. (12) into Eq. (15) gives:

$$\mathcal{U}_j = \frac{1}{2}\boldsymbol{d}_j^T \boldsymbol{\mathcal{N}}^T \boldsymbol{K}^f \boldsymbol{\mathcal{N}} \boldsymbol{d}_j \quad \text{and} \quad \mathcal{T}_j = \frac{1}{2}\dot{\boldsymbol{d}}_j^T \boldsymbol{\mathcal{N}}^T \boldsymbol{M}^f \boldsymbol{\mathcal{N}} \dot{\boldsymbol{d}}_j \tag{16}$$

Comparing Eq. (14) and Eq. (16) shows that:

$$\boldsymbol{K}_j = \boldsymbol{\mathcal{N}}^T \boldsymbol{K}^f \boldsymbol{\mathcal{N}} \quad \text{and} \quad \boldsymbol{M}_j = \boldsymbol{\mathcal{N}}^T \boldsymbol{M}^f \boldsymbol{\mathcal{N}} \tag{17}$$

where $\boldsymbol{K}_j$ and $\boldsymbol{M}_j$ are the equivalent stiffness and mass matrices of the j^{th} MSE. Similarly to what observed for static condensation, the proposed approach provides an exact condensation of the elastic properties of the fine scale, but only an approximate representation of the mass matrix $\boldsymbol{M}_j$. As suggested by Eq. (17), the calculation of $\boldsymbol{K}_j$ and $\boldsymbol{M}_j$ does not require any numerical integration procedure but simply the product between the corresponding local matrices and the matrix of multiscale shape functions of the element.

For transient, time-domain simulations, this procedure is carried out only once for each MSE before starting the time integration loop, and the resulting local matrices $\boldsymbol{K}_j$ and $\boldsymbol{M}_j$ are stored into memory. If an explicit integration scheme is adopted, as commonly done for transient wave problems, the local stiffness matrix can be utilized for the calculation of the internal forces of the j^{th} MSE as $\boldsymbol{f}_j^{(int)} = -\boldsymbol{K}_j \, \boldsymbol{d}_j$, while the mass matrix $\boldsymbol{M}_j$ can be easily diagonalized by means of standard mass lumping techniques [38]. In the case of implicit time integration, or for eigenvalue analysis, the local contributions deriving from each MSE can be assembled as part of the final sparse system of equations that is solved only in terms of the coarse-scale unknowns $\boldsymbol{d}$. The local information $\boldsymbol{q}$ is recovered in the post-processing stage by projecting the computed coarse-scale solution onto the fine-scale mesh (where it is defined) as indicated by Eq. (12).

2.3 Compatibility conditions

The proposed set of basis functions must guarantee the continuity of the solution (displacements) across common boundaries of neighboring elements. For instance the FE solution must match along the edges of two-dimensional elements or on the common faces of solid elements. As described in the previous section, this condition is

enforced on the nodes of the fine-scale mesh that lie along the boundaries of the MSE. However, due to the approximate nature of the fine-scale model, this condition does not necessarily ensure that adjacent elements display the same solution point-wise on the common interface. In this section, the general framework utilized to derive the required compatibility conditions is first introduced and then applied to specific finite elements.

2.3.1 General framework

The problem of inter-element compatibility is addressed here by considering a general interface scenario between 3D elements. For instance, Fig. 8 shows a 8-node hexahedral element (HEXA) which neighbors a general multiscale element with quadrilateral faces intersected by a hole through the center. The interface between these two elements is defined by nodes (1, 2, 3, 4) of the HEXA element that coincide with the corresponding nodes (I, II, III, IV) of the adjacent MSE. A scalar field function $\phi(\boldsymbol{x})$,

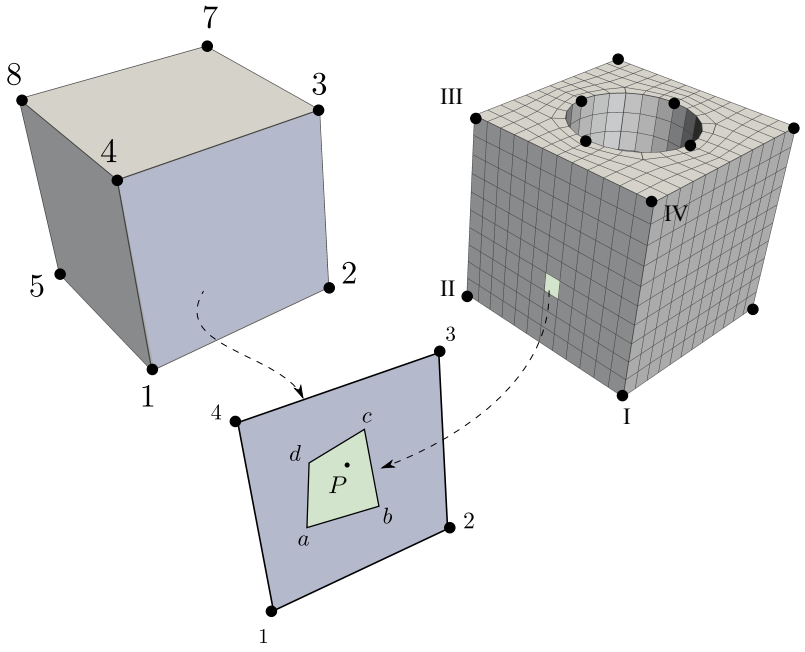

Figure 8: Interface between a 8-node hexahedral elements and an arbitrary three-dimensional multiscale element.

representing a generic numerical solution, is defined over the considered face in terms

of the nodal values ϕ_i $(i = 1, 2, 3, 4)$, and can be interpolated at any arbitrary point through the shape functions of the two adjacent elements. For instance, the value of $\phi(\boldsymbol{x})$ at an arbitrary point P lying on the considered boundary surface (see Fig. 8) can be expressed as:

$$\phi(\boldsymbol{x}_p) = \phi_p = \sum_{i=1}^{4} h_i(r_p, s_p)\, \phi_i \tag{18}$$

or in matrix form as:

$$\phi_p = \boldsymbol{h}(r_p, s_p)^T\, \boldsymbol{\phi} \tag{19}$$

where $\boldsymbol{h} = [h_1,\ h_2,\ h_3,\ h_4]^T$, $\boldsymbol{\phi} = [\phi_1,\ \phi_2,\ \phi_3,\ \phi_4]^T$, and (r_p, s_p) denote the natural coordinates that identify the location of P in the reference element of the transformation $\mathcal{M}_1$ shown in Fig. 9.

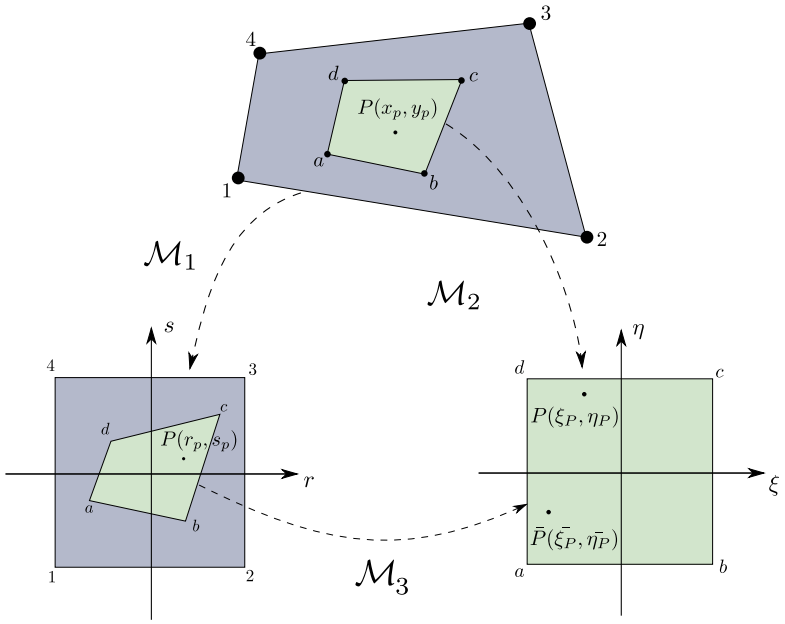

Figure 9: Isoparametric transformations used to derive compatibility conditions between multiscale elements.

In Eq. (18), $h_i(r_p, s_p)$ represents the i^{th} interpolation function of the coarse-scale element restricted on the face (1,2,3,4), that for the HEXA element shown in Fig. 8

are given by:

$$h_1(r,s) = \frac{1}{4}(1-r)(1-s) \qquad h_2(r,s) = \frac{1}{4}(1+r)(1-s)$$
$$h_3(r,s) = \frac{1}{4}(1+r)(1+s) \qquad h_4(r,s) = \frac{1}{4}(1-r)(1+s) \tag{20}$$

Note that in Eq. (19) such shape functions are evaluated at point (r_p, s_p) corresponding to the coordinates of point P expressed in the reference element space defined by the isoparametric transformation $\mathcal{M}_1$ shown in Fig. 9.

Similarly, the value of the considered test function can be interpolated at the same point P using the nodal information derived from the adjacent multiscale element. In this case, the solution ϕ_p is expressed using the microscopic information ϕ_α ($\alpha = a, b, c, d$) available at the nodes of the fine-scale element shown in Fig. 8 as:

$$\phi_p = \overline{\boldsymbol{h}}(\xi_p, \eta_p)^T \, \boldsymbol{\phi}_\alpha \tag{21}$$

where $\boldsymbol{\phi}_\alpha = [\phi_a \ \phi_b \ \phi_c \ \phi_d]^T$, and $\bar{\boldsymbol{h}}(\xi, \eta)$ denotes the basis functions that define the map $\mathcal{M}_2$ illustrated in Fig. 9. Note that in Eq. (21) ξ_p, and η_p are the natural coordinates that identify point P in the reference element of the map $\mathcal{M}_2$ (see Fig. 9). At this point, it is important to recall that the values of ϕ at nodes (a, b, c, d) are related to the coarse-scale information ϕ_i through the constraints equations imposed by Lagrange multipliers $\boldsymbol{\lambda}$ on the DOFs of the fine-scale model. Such relationships are expressed as:

$$\phi_a = \boldsymbol{h}(r_a, s_a)^T \, \boldsymbol{\phi} \qquad \phi_b = \boldsymbol{h}(r_b, s_b)^T \, \boldsymbol{\phi}$$
$$\phi_c = \boldsymbol{h}(r_c, s_c)^T \, \boldsymbol{\phi} \qquad \phi_d = \boldsymbol{h}(r_d, s_d)^T \, \boldsymbol{\phi} \tag{22}$$

or in compact matrix form as:

$$\boldsymbol{\phi}_\alpha = \boldsymbol{\mathcal{H}} \, \boldsymbol{\phi} \tag{23}$$

where

$$\boldsymbol{\mathcal{H}} = [\boldsymbol{h}(r_a, s_a) \ \boldsymbol{h}(r_b, s_b) \ \boldsymbol{h}(r_c, s_c) \ \boldsymbol{h}(r_d, s_d)]^T \tag{24}$$

is a matrix of known coefficients.

The two-element configuration shown in Fig. 8 generates a fully compatible solution across the entire boundary (i.e. face 1,2,3,4) if the value of the test function ϕ_p interpolated at point P using the global information equals the solution interpolated at the same point using the micro scale information. Substituting Eq. (23) in Eq. (21) and comparing the result with Eq. (19) gives:

$$\boldsymbol{h}(r_p, s_p) = \boldsymbol{\mathcal{H}}^T \overline{\boldsymbol{h}}(\xi_p, \eta_p) \tag{25}$$

The proposed approach to enforce inter-element continuity of displacements is therefore valid as long as Eq. (25) is satisfied. In order to better understand the nature of Eq. (25), a third affine map $\mathcal{M}_3$ is introduced, as shown in Fig. 9. This transformation is defined such that points (a,b,c,d) in the (r, s) space are mapped into the reference element in the (ξ, η) space. Point $P(r_p, s_p)$ is transformed accordingly into $\bar{P}(\overline{\xi}_p, \overline{\eta}_p)$ that is in general different from point $P(\xi_p, \eta_p)$ resulting from the transformation $\mathcal{M}_2$. It can be easily proved that Eq. (25) is identically satisfied if $\bar{P}$ coincides with point P, that is when:

$$\xi_p = \overline{\xi}_p \quad \text{and} \quad \eta_p = \overline{\eta}_p \tag{26}$$

If Eq. (26), holds then:

$$\phi_p = \overline{\boldsymbol{h}}(\xi_p, \eta_p)^T \boldsymbol{\phi}_\alpha \tag{27}$$

and Eq. (25) follows from simple algebraic identities (see Appendix A).

In the following sections, specific finite elements are considered in order to explicitly determine the conditions on the fine-scale mesh that are required in order to exactly satisfy Eq. (25).

2.3.2 Two-dimensional linear elements

In case of two-dimensional (2D) multiscale finite elements, displacement compatibility must be enforced along the *edges* shared by adjacent elements, as shown in Fig. 10.

Along segments (1,2) and (a,b) both standard and multiscale elements feature piece-

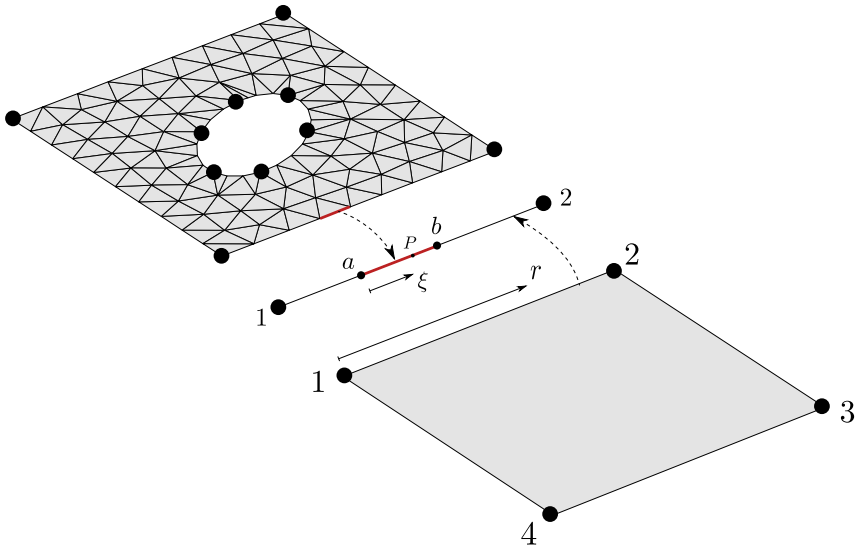

Figure 10: Global and local mesh restricted along the edge of a 2D element.

wise linear interpolations functions:

$$h_1(r) = \frac{1}{2}(1-r) \quad \text{and} \quad h_2(r) = \frac{1}{2}(1+r) \tag{28}$$

The value of a generic field variable at point P is therefore interpolated from the nodal values ϕ_1 and ϕ_2 as

$$\phi_p = \frac{1}{2}(1-r_p)\,\phi_1 + \frac{1}{2}(1+r_p)\,\phi_2 \tag{29}$$

or as a function of the nodal values ϕ_a and ϕ_b as

$$\phi_p = \frac{1}{2}(1-\xi_p)\,\phi_a + \frac{1}{2}(1+\xi_p)\,\phi_b \tag{30}$$

The two considered elements display compatible solutions at their common interface if the two expressions for ϕ_p given in Eq. (29) and Eq. (30) coincide. This condition can be formalized through the definition of the following error function:

$$\mathcal{E} = \frac{1}{2}(1-r_p)\,\phi_1 + \frac{1}{2}(1+r_p)\,\phi_2 - \frac{1}{2}(1-\xi_p)\,\phi_a - \frac{1}{2}(1+\xi_p)\,\phi_b = 0 \tag{31}$$

obtained by subtracting Eq. (30) from Eq. (29). The kinematic conditions imposed on the fine-scale DOFs require that ϕ_a and ϕ_b satisfy the following constraints:

$$\begin{aligned}\phi_a &= \frac{1}{2}(1 - r_a)\,\phi_1 + \frac{1}{2}(1 + r_a)\,\phi_2 \\ \phi_b &= \frac{1}{2}(1 - r_b)\,\phi_1 + \frac{1}{2}(1 + r_b)\,\phi_2\end{aligned} \tag{32}$$

while the compatibility conditions expressed in the form of Eq. (27) require that:

$$r_p = \frac{1}{2}(1 - \xi_p)\,r_a + \frac{1}{2}(1 + \xi_p)\,r_b \tag{33}$$

Substituting Eq. (32) and Eq. (33) into Eq. (31) leads to:

$$\begin{aligned}2\,\mathcal{E} = &\left[1 - \frac{1}{2}(1-\xi_p)r_a - \frac{1}{2}(1+\xi_p)r_b - \frac{1}{2}(1-\xi_p)(1-r_a) - \frac{1}{2}(1+\xi_p)(1-r_b)\right]\,\phi_1 + \\ &\left[1 + \frac{1}{2}(1-\xi_p)r_a + \frac{1}{2}(1+\xi_p)r_b - \frac{1}{2}(1-\xi_p)(1+r_a) - \frac{1}{2}(1+\xi_p)(1+r_b)\right]\,\phi_2 \;=\; 0\end{aligned} \tag{34}$$

It can be easily shown that the bracketed terms in Eq. (34) are identically zero for any combination of r_a, r_b, and ξ_p, indicating that compatibility between the global and local solutions of the considered elements is always guaranteed as long as the linearity constraints expressed by Eq. (32) are correctly enforced.

2.3.3 Three-dimensional elements

In the case of three-dimensional MSE, displacement compatibility must be enforced on the *faces* shared by adjacent elements. This analysis focuses only on the interaction between arbitrary MSEs and 8-node HEXA elements typically used for 3D wave simulations. In three dimensions, different types of finite elements can be adopted for the fine-scale mesh of a given MSE. Therefore, different conditions must be separately considered. For instance, Fig. 11 illustrates how the same multiscale element presented in Fig. 8 can be discretized with a fine-scale mesh comprised of tetrahedral elements (TETRA) instead of HEXA as considered in the previous section.

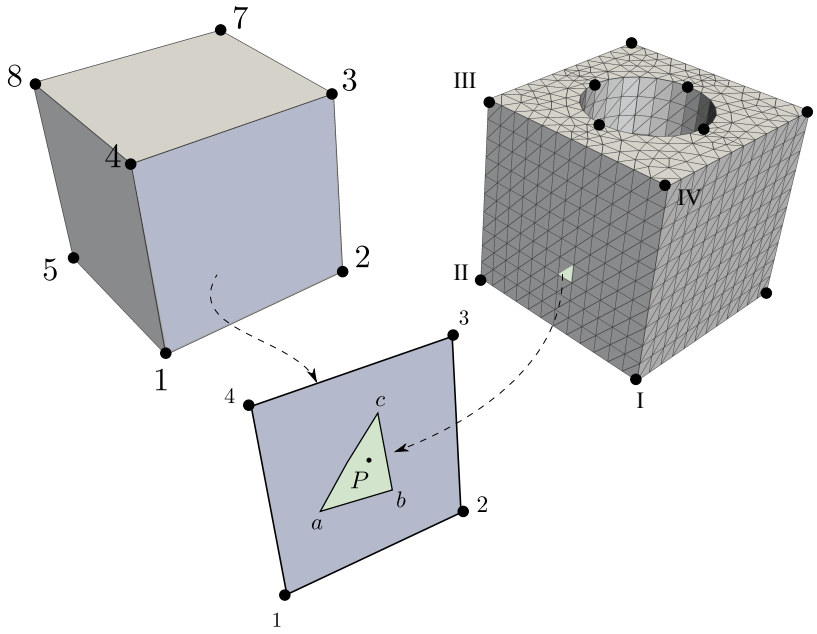

Figure 11: Interface between a 8-node hexahedral elements and an arbitrary three-dimensional multiscale element.

Although the formal treatment proposed to study compatibility still applies, the different topological nature of the elements at the common interface requires a dedicated investigation.

Following the procedure proposed in the previous sections, the conditions required to guarantee fully compatible solutions are derived by considering a scalar test function $\phi(\boldsymbol{x})$ interpolated at an arbitrary location over the inter-element boundary. The value of $\phi(\boldsymbol{x})$ at a generic point P (see Fig. 8, and Fig. 11) lying on the face (1,2,3,4) of an HEXA element is interpolated from the four nodal values ϕ_i $(i = 1, 2, 3, 4)$ as:

$$\begin{aligned}\phi_p =& \frac{1}{4}(1 - r_p)(1 - s_p)\,\phi_1 + \frac{1}{4}(1 + r_p)(1 - s_p)\,\phi_2 + \\ &+ \frac{1}{4}(1 + r_p)(1 + s_p)\,\phi_3 + \frac{1}{4}(1 - r_p)(1 + s_p)\,\phi_4\end{aligned} \tag{35}$$

The same value can be expressed as a function of the micro scale nodal values of the adjacent MSE. If the fine-scale mesh is composed by TETRA elements (see Fig. 11), then ϕ_p is written in terms of the shape functions of the triangular element identified

by nodes (a,b,c) as:

$$\phi_p^{\triangle} = (1 - \xi_p - \eta_p)\,\phi_a + \xi_p\,\phi_b + \eta_p\,\phi_c \tag{36}$$

When the local mesh features quadrilateral-faced elements (see Fig. 8), the considered test function at point P is:

$$\begin{aligned}\phi_p^{\square} =& \frac{1}{4}(1-\xi_p)(1-\eta_p)\,\phi_1 + \frac{1}{4}(1+\xi_p)(1-\eta_p)\,\phi_2 + \\ &+\frac{1}{4}(1+\xi_p)(1+\eta_p)\,\phi_3 + \frac{1}{4}(1-\xi_p)(1+\eta_p)\,\phi_4\end{aligned} \tag{37}$$

The following error functions are defined to measure the difference between the micro and macro scale solutions:

$$\mathcal{E}^{\triangle} \equiv \phi_p - \phi_p^{\triangle} \tag{38}$$

and

$$\mathcal{E}^{\square} \equiv \phi_p - \phi_p^{\square} \tag{39}$$

Following the footsteps highlighted in the previous section, Eq. (36) and (37) are substituted into Eq. (38) and (39) respectively. Finally Eq. (35) is used to rewrite $\mathcal{E}^{\triangle}$ and $\mathcal{E}^{\square}$ in terms of the relative orientations of the two meshes as:

$$\mathcal{E}^{\triangle} = \frac{\phi_1 - \phi_2 + \phi_3 - \phi_4}{4}\left(B_1\,\eta_p^2 + B_2\,\eta_p + B_3\right) \tag{40}$$

and

$$\mathcal{E}^{\square} = \frac{\phi_1 - \phi_2 + \phi_3 - \phi_4}{64}\left(A_1\,\eta_p^2 + 2\,A_2\,\eta_p + A_3\right) \tag{41}$$

where the coefficients A_i and B_i (i=1,2,3) are functions of the natural coordinates (r_α, s_α) and the arbitrary location (ξ_p, η_p) of point P in the (ξ, η) space (see Fig. 9). For the sake of clarity, explicit expressions for A_1, A_2, A_3, and B_1, B_2, B_3 are in Appendix B. For perfectly compatible solutions, $\mathcal{E}^{\triangle}$ and $\mathcal{E}^{\square}$ must vanish for any arbitrary combination of the coarse-scale nodal values ϕ_i (i=1,2,3,4). This clearly occurs only if:

$$A_1 = A_2 = A_3 = 0 \quad \text{and} \quad B_1 = B_2 = B_3 = 0 \tag{42}$$

Since the terms ξ_p and η_p in the expression of the coefficients A_i and B_i are arbitrary parameters that identify a generic location over the inter-element boundary, the conditions in Eq. (42) are equivalent to imposing a constraint on r_α and s_α. Such conditions identify the relative orientation of the fine-scale element with respect to the external interface. Algebraic manipulations show that $\mathcal{E}^{\square}$ is identically zero if the following conditions are simultaneously satisfied:

$$s_b = s_a, \quad r_b = r_c, \quad s_c = s_d, \quad \text{and} \quad r_d = r_a \tag{43}$$

Note that Eq. (43) is equivalent to requiring that the edges of each element of the fine-scale mesh are aligned to the natural coordinates of the quadrilateral face (1,2,3,4) of the neighboring element as schematically shown in Fig. 12.a. When Eq. (43) is not satisfied, the elements of the local discretization are arbitrarily oriented with respect to the quadrilateral interface (see Fig. 12.b). In such cases two adjacent elements will feature different displacements over the common boundary thus generating voids or regions of material overlapping. Analysis of Eq. (40) reveals that it is not possible to

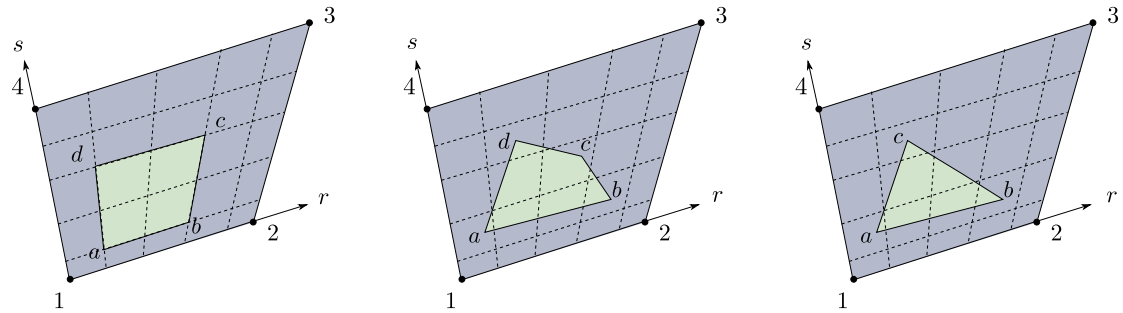

Figure 12: Summary of possible compatible (a), and incompatible (b,c) interface configurations between hexahedral elements and MSEs featuring HEXA or TETRA local meshes.

determine a condition similar to Eq. (42) that identically nullifies $\mathcal{E}^{\triangle}$. This implies that it is not possible to have perfectly matching solutions between HEXA elements and MSEs that employ a tetrahedral local mesh (Fig. 12.c).

The formalism presented herein identifies the geometrical conditions required for

compatible solutions across adjacent elements. As previously shown, discrepancies in this regard are associated with the fact that neighboring elements with dissimilar local meshes feature different interpolation schemes over the common boundary. The interpolation error associated with incompatible meshes is however related to the size of the fine-scale mesh relative to the area of the boundary region, and therefore will converge to zero as the size of the fine-scale discretization reduces. In other words, due to the converging properties of the piecewise linear interpolating functions, the interpolation errors $\mathcal{E}^{\triangle}$ and $\mathcal{E}^{\square}$ can be reduced, for arbitrary values of r_α and s_α, by reducing the size of the fine-scale mesh. Instead of following an analytical approach, this behavior is illustrated by numerical examples presented in the following section.

From the previous discussion on compatibility between 3D multiscale elements, it is also possible to observe how the proposed method does not allow imposing continuity conditions over arbitrarily-shaped boundaries. The approach in fact requires expressing the solution at an arbitrary point within the inter-element boundary as a linear combination of the solution at the coarse-scale nodes defining the boundary itself. For instance, consider the case shown in Fig. 13.a in which two multiscale ele-

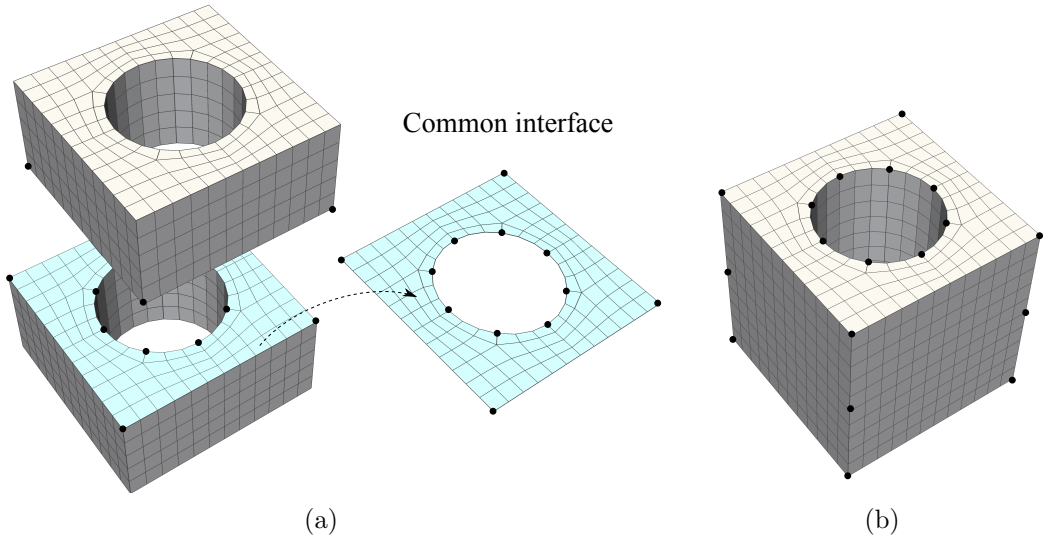

Figure 13: Example of multiscale elements with an irregular interface (a), and possible solution to combine the two MSEs (b).

ments with a central hole are stacked on top of each other. In this case the common interface consists of a quadrilateral region with a circular void at the center. This scenario could for example represent a case in which a through-thickness defect in a 3D plate model is discretized using multiple multiscale elements. The problem can be easily circumvented through the definition of one multiscale element that matches the actual through-thickness discretization of the system, as shown in Fig. 13.b. Clearly such considerations do not apply to two-dimensional multiscale elements for which inter-element boundaries can always be described as a series of straight lines if bilinear elements are used.

2.4 Numerical examples

Numerical examples illustrate the developed GMsFEM method with emphasis on the different aspects related to inter-element compatibility previously described.

2.4.1 Three-dimensional patch test

The first example presented in this section consists of the three-dimensional patch test originally proposed by MacNeal and Harder [83]. The idea is to verify a multiscale element's ability to represent a constant stress/strain field, and thus to ensure completeness and the ability to converge in the limit as the element size decreases. In addition to these classical considerations, several kinds of fine-scale elements are used to illustrate their influence on compatibility. As shown in Fig. 14.a the unit cube is discretized with a set of seven irregular brick elements, each being equipped with a proper fine-scale mesh and a set of multiscale shape functions. A prescribed linear displacement is imposed to the eight exterior nodes:

$$\begin{aligned} u &= 0.5\,(2x + y + z)\ 10^{-4}\ m \\ v &= 0.5\,(x + 2y + z)\ 10^{-4}\ m \\ w &= 0.5\,(x + y + 2z)\ 10^{-4}\ m \end{aligned} \tag{44}$$

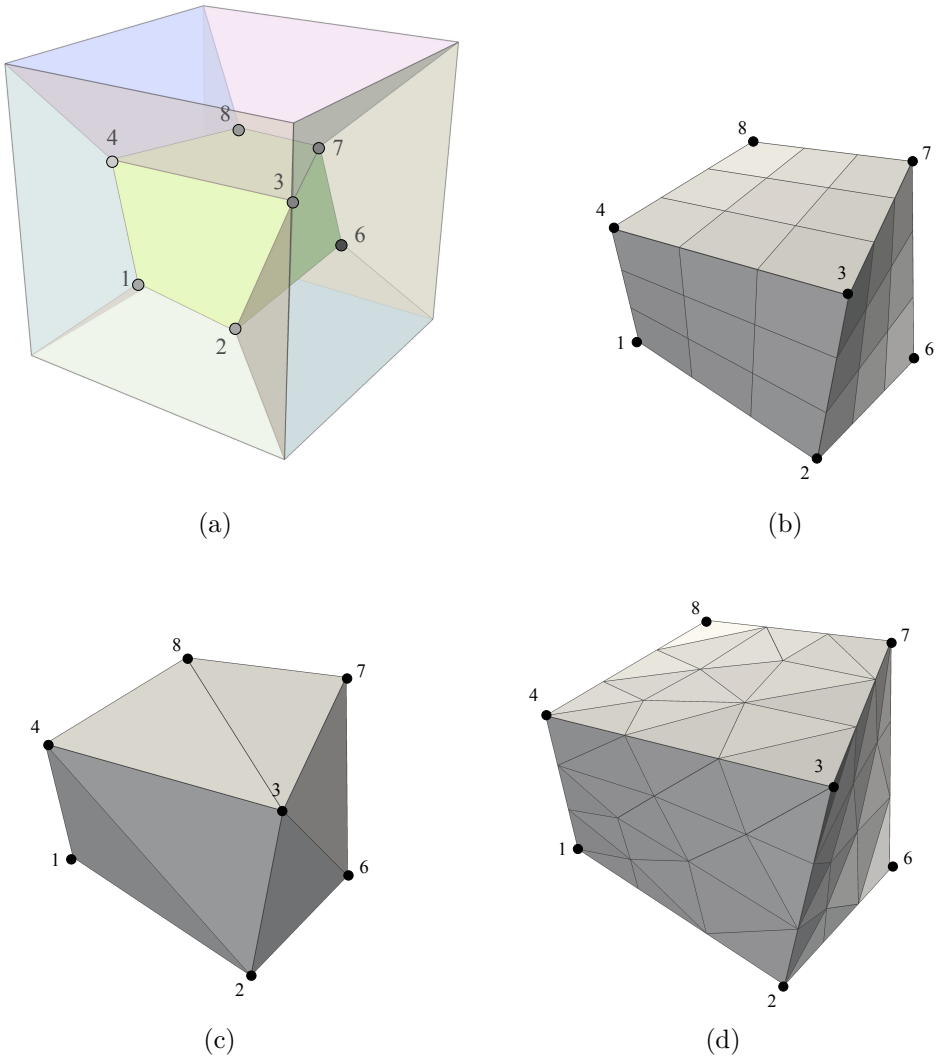

Figure 14: Seven irregular multiscale elements comprising the geometry of the 3D patch test (a), and examples of fine-scale meshes utilized within each MSE (b,c,d).

The remaining eight interior nodes must deform in such a way that all the elements have an identical constant state of stress in order to pass the test. The problem is intended to be quasi-static, and the displacements are applied gradually up to a specific steady-state value according to the following loading curve:

$$f(t) = \begin{cases} 0.5\,(1 - \cos(\pi\, t)) & 0 < t < 1 \\ 1 & t > 1 \end{cases} \tag{45}$$

The material is linearly elastic, with Young's modulus $E = 600$ kPa, and $\nu = 0.2$. Substituting the displacement boundary conditions given by Eq. (44) into the strain-displacement relations leads to the following analytical solution:

$$\varepsilon_x = \varepsilon_y = \varepsilon_z = \gamma_{xy} = \gamma_{xz} = \gamma_{yz} = 10^{-4} \tag{46}$$

From Hooke's law, the corresponding stresses are given by:

$$\sigma_x = \sigma_y = \sigma_z = 100\ Pa \quad \text{and} \quad \tau_{xy} = \tau_{xz} = \tau_{yz} = 25\ Pa \tag{47}$$

This problem is first solved using for each MSE a fine-scale mesh comprised of 27 hexahedral elements with edges oriented along the natural coordinates of the outer faces as shown for a representative element in Fig. 14.b. Results illustrated in Fig. 15 show the time variation of the stresses σ_x and τ_{xy} whose maximum analytical values are given in Eq. (47). As discussed in the previous section, the adopted local meshes satisfy the conditions that analytically guarantee inter-element compatibility, and the maximum discrepancy observed with the analytical solution is of the order of the machine epsilon. The same analysis is conducted when tetrahedral elements are used in the fine-scale mesh of each MSE. Examples of such local discretizations are shown in Fig. 14.c,d for the central element of the domain. According to what was derived in the previous section, multiscale shape functions computed with such mesh do not generate compatible displacements over the faces shared by adjacent elements, with detrimental consequences on the accuracy of the resulting numerical solution. This phenomenon is illustrated for instance in Fig. 16.a,b showing that significant discrepancies occur when the coarsest TETRA mesh is used in the fine-scale. Also, Fig. 16.c-f show how such numerical errors gradually tend to zero as the size of the local meshes is refined. This is related to the converging properties of the finite element solution used to compute the local shape functions. This idea is corroborated by results illustrated in Fig. 17 showing how the rate of convergence of such interpolation error decreases almost linearly with the number of nodes in the

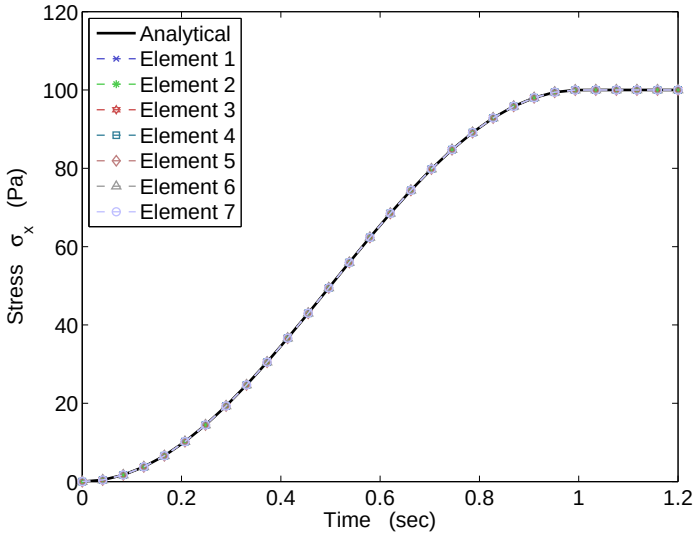

(a)

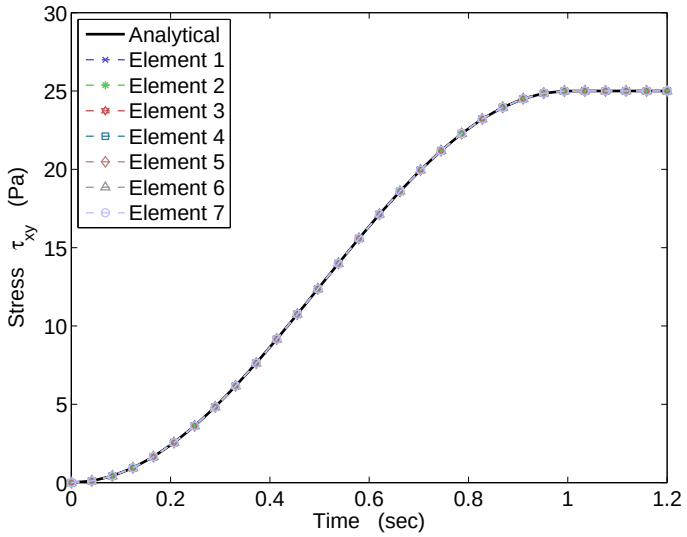

(b)

Figure 15: Time histories of the stress components σ_x (a), and τ_{xy} (b) of each element when the fine-scale mesh features 27 HEXA elements.

fine-scale mesh. The sub-optimal convergence rate observed in Fig. 17 is attributed to the non conforming shape functions characterizing the adopted MSEs that generate incompatible displacements across the elements' boundaries.

Clearly, one advantage of using TETRA elements at the local scale is related to their superior modeling flexibility especially when dealing with complex geometries such as voids or material inclusions. However, as shown by this analysis, the use of

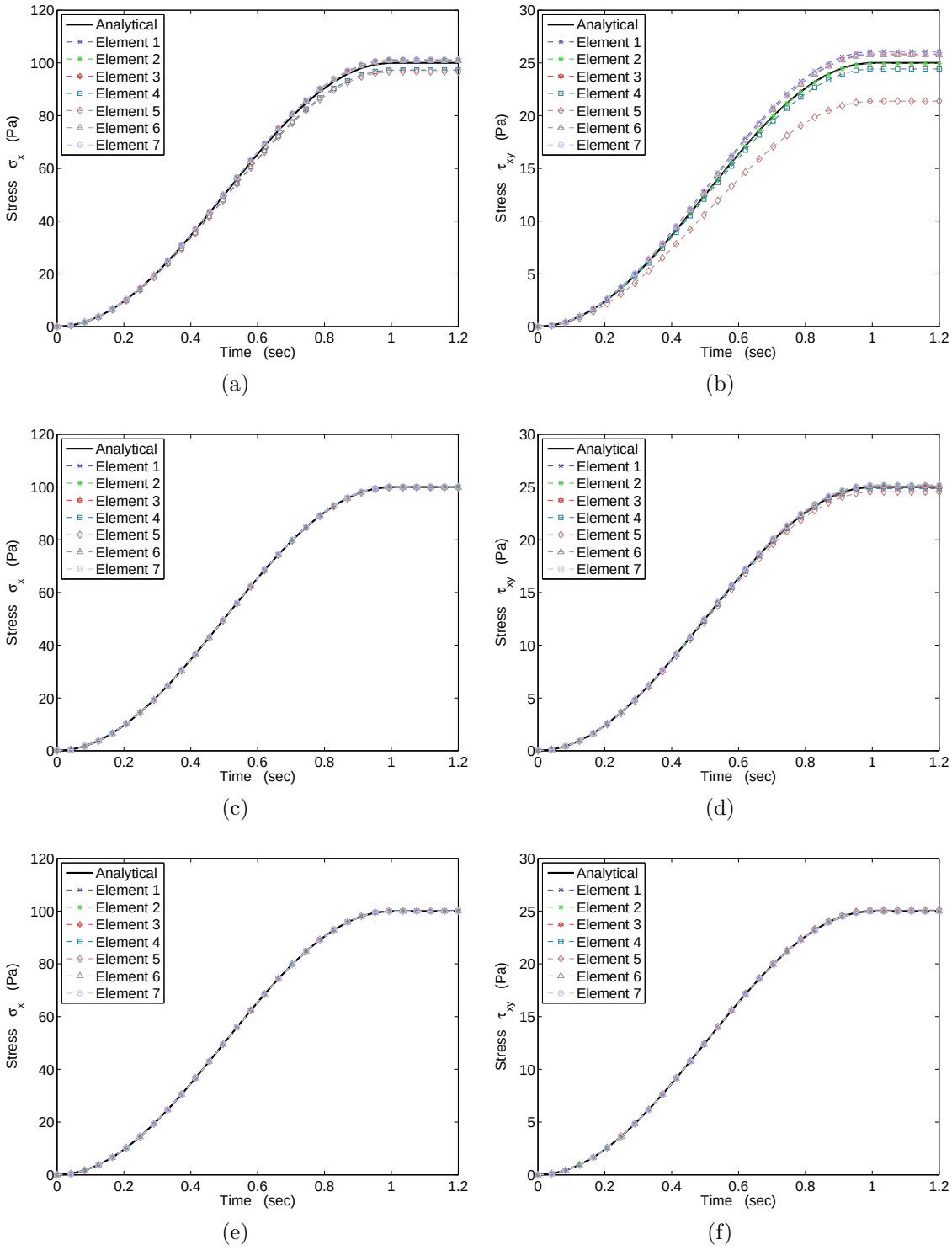

Figure 16: Time histories of the stress components σ_x (first column), and τ_{xy} (second column) of each element with fine-scale meshes composed of 12 TETRA elements (a,b), 60 TETRA elements (c,d), and 232 TETRA elements (e,f).

TETRA elements for the calculation of multiscale shape functions typically requires a higher number of fine-scale elements that therefore increases the computational overhead related to this task.

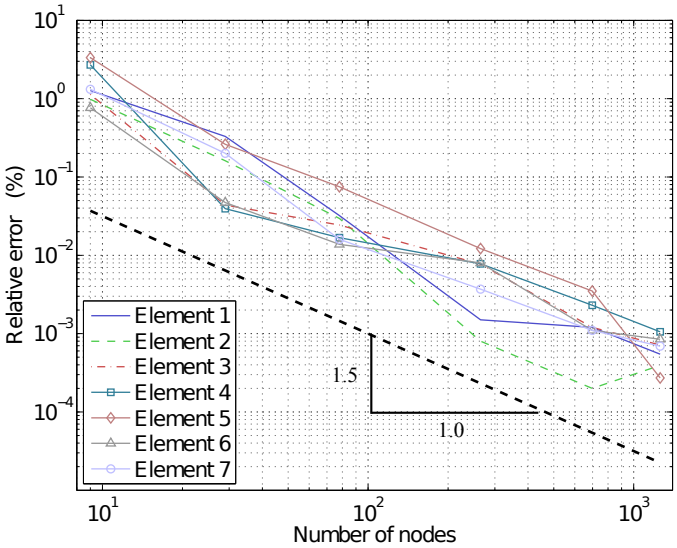

(a)

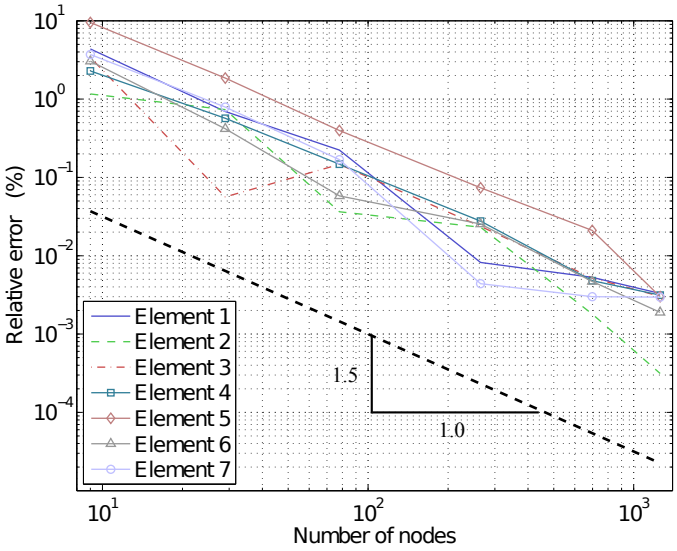

(b)

Figure 17: Convergence histories of the error of σ_x (a), and τ_{xy} (b) as a function of the number of fine-scale nodes characterizing the local TETRA mesh.

2.4.2 Energetic analysis of compatibility

A three-dimensional plate bending problem illustrates the effects of the choice of different types of fine-scale elements on the macroscopic energy of the system. The considered aluminum plate (E=71 GPa, ν=0.3, and ρ = 2700 kg/m^3) features side lengths L_x=1.0 m, L_y=1.0 m, L_z=0.1 m, is clamped along one side, and is loaded by a distributed out-of-plane (vertical) force as shown in Fig. 18. The structure is

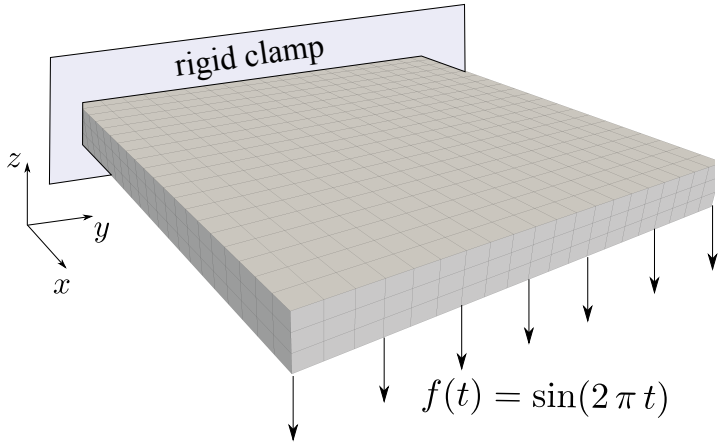

Figure 18: Discretization and boundary conditions of the considered aluminum plate.

first discretized with a uniform mesh of 20×20×3 hexahedral elements, and the time histories of the strain and kinetic energies are evaluated from the transient response computed by means of an implicit time integration scheme of the Newmark family. The same quantities are computed when the plate is modeled using 20×20×1 multiscale elements, each replacing three through-thickness HEXA elements used in the standard mesh. For the fine-scale of each MSE both TETRA elements and 6-node wedge elements (WEDGE) are considered. As previously mentioned, TETRA elements are particularly appealing for their modeling flexibility and the wide availability of software tools for mesh generation. In this study WEDGE elements are also considered as they combine the "in-plane" modeling capabilities of TETRA elements with the possibility of exactly satisfying the compatibility conditions over the boundaries of MSEs with quadrilateral faces. Results of such analysis are shown

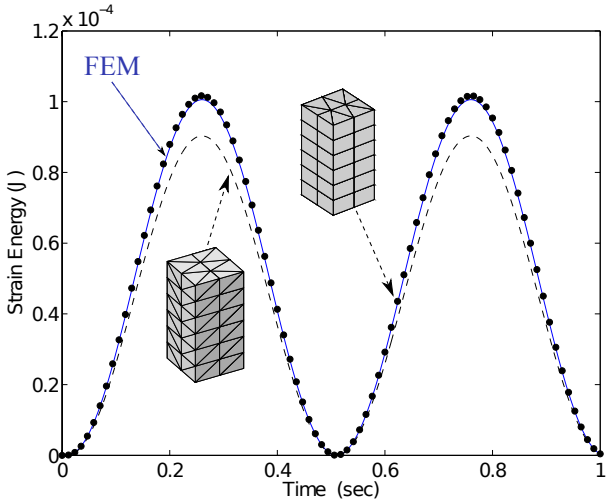

(a)

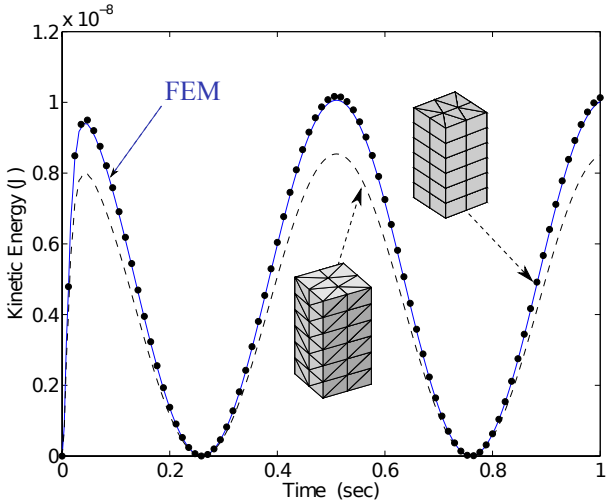

(b)

Figure 19: Time history of the strain energy (a) and kinetic energy (b) of the system computed with different types of elements: 8-node HEXA elements (solid blue line), MSEs with TETRA fine-scale elements (dashed black line), and MSEs with WEDGE fine-scale elements (• markers).

in Fig. 19 which compares the time histories of the strain (Fig. 19.a) and kinetic (Fig. 19.b) energies computed with the aforementioned elements. Such comparison reveals the close agreement between solutions obtained with HEXA elements and using MSEs with a local mesh comprised of WEDGE elements. Such elements are characterized by quadrilateral side faces, and therefore allow for the calculation of multiscale shape functions that exactly satisfy compatibility. Also, Fig. 19 illustrates

that an energy deficit characterizes the response of the system discretized with MSEs featuring TETRA fine-scale elements. In this case, MSEs are not compatible across boundaries, so that the resulting mesh features non-physical deformation modes that tend to "over-soften" the element. As mentioned in the previous sections, such dis-

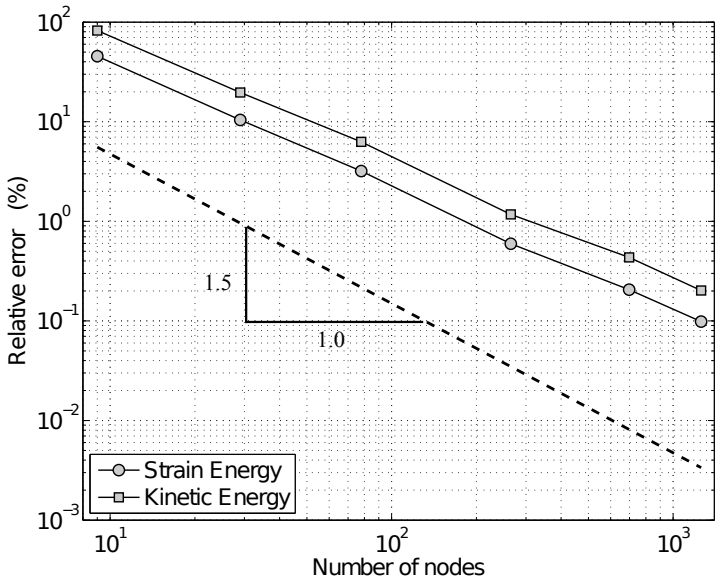

Figure 20: Convergence histories of the strain and kinetic energies as a function of the number of fine-scale nodes characterizing the local TETRA mesh.

crepancies tend to zero as the fine mesh is refined. This trend is shown in Fig. 20 which illustrates the convergence histories of the following error functions

$$\mathcal{E}^{\mathcal{U}} = \left(\mathcal{U}_{FEM} - \mathcal{U}^{\triangle}_{GMsFEM}\right) / \, \mathcal{U}_{FEM} \cdot 100 \tag{48}$$

$$\mathcal{E}^{\mathcal{K}} = \left(\mathcal{K}_{FEM} - \mathcal{K}^{\triangle}_{GMsFEM}\right) / \, \mathcal{K}_{FEM} \cdot 100 \tag{49}$$

corresponding to the maximum difference between the strain and kinetic energies ($\mathcal{U}^{\triangle}_{GMsFEM}$, and $\mathcal{K}^{\triangle}_{GMsFEM}$) of the system computed with TETRA multiscale elements and with the reference HEXA finite elements ($\mathcal{U}_{FEM}$, and $\mathcal{K}_{FEM}$).

2.4.3 Beam with spherical inclusions

This example illustrates the application of GMsFEM to the dynamic analysis of a three-dimensional beam-like structure with a distribution of spherical voids. Both the

transient and free dynamic response of the system are evaluated when the structure is discretized with multiscale elements, and results are compared with the solution obtained through the direct solution of the entire fine-scale.

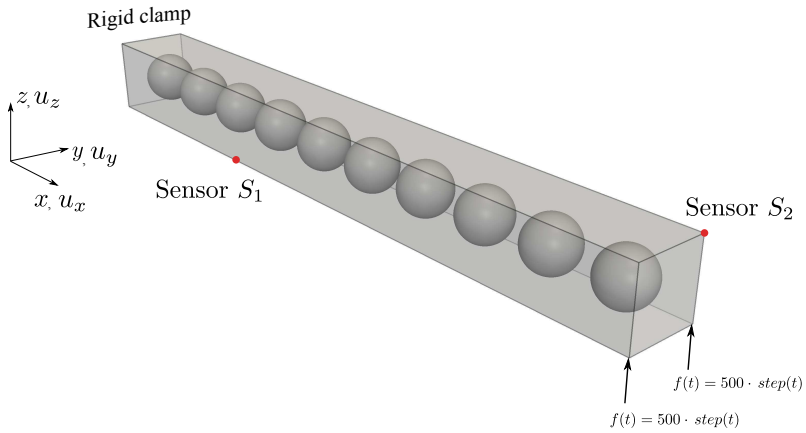

Figure 21: Schematic of the considered 3D beam problem.

The beam, shown in Fig. 21, is L=1.0 m long, and features a square cross section with side length l=0.1 m. The structure is made of an isotropic material (E=71 GPa, ν=0.3, and ρ=2700 kg/m^3) and is characterized by ten spherical voids of radius R=0.035 m equally distributed along its length. The system is modeled using ten

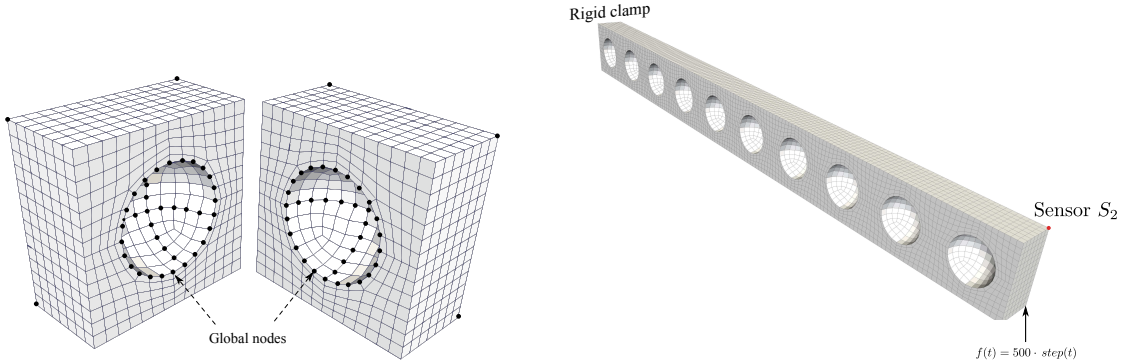

(a) (b)

Figure 22: Split view of a 74-node multiscale element with an internal spherical void (a), and sliced view of the entire fine-scale mesh of the beam (b).

multiscale elements (one for each spherical void) each featuring eight coarse-scale nodes at the exterior corners of the element, plus 66 additional global nodes along

the three equators of the internal sphere, as shown in Fig. 22.a. A sliced view of the fine-scale mesh over the entire structure is shown in Fig. 22.b. Each multiscale

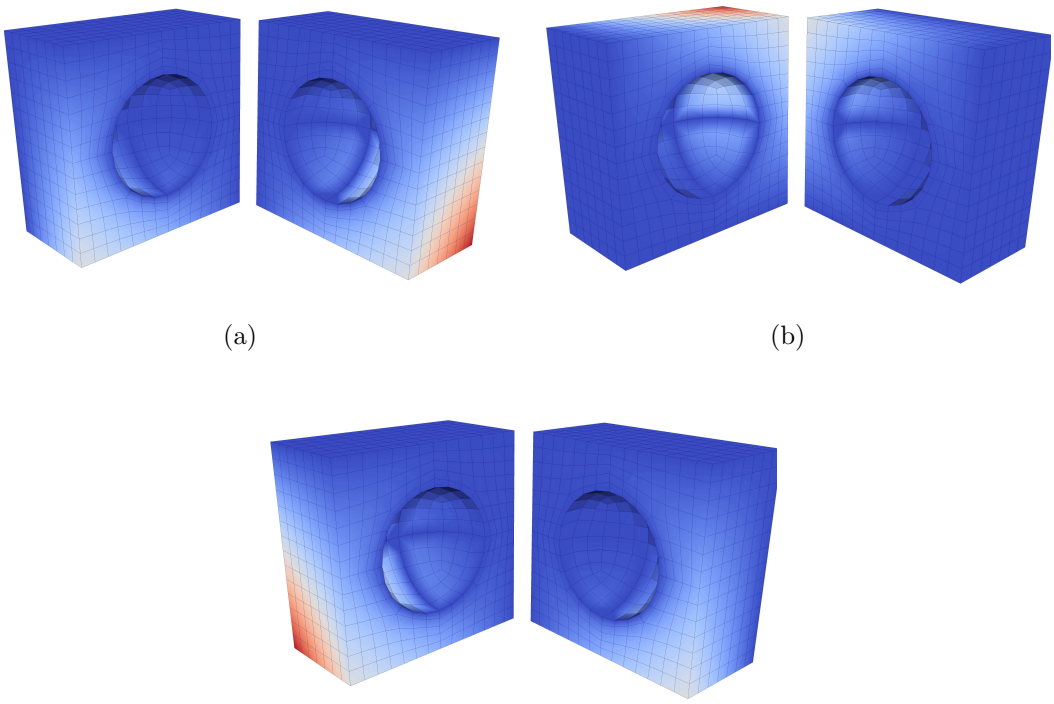

(a) (b)

(c)

Figure 23: Subset of multiscale shape functions of the considered element.

element is equipped with a set of multiscale shape functions (see Fig. 23) computed with the procedure previously described imposing compatibility conditions over the six external faces of the element.

The free dynamic response of the system is evaluated when a clamped boundary condition is imposed at one end of the beam, as shown in Fig. 21. A summary of the first ten natural frequencies is presented in Table 1 which compares the GMsFEM predictions with FEM results obtained through the direct solution of all the fine-scale degrees of freedom. The associated normal modes are also shown in Fig. 25. Note that repeated frequencies associated with eigenmodes vibrating in the two planes of symmetry for the problem are considered only once. The excellent agreement

Table 1: Natural frequencies of the beam computed with GMsFEM (704 nodes) and comparison with the fine-scale solution (32655 nodes).

Mode label	**Natural frequencies (Hz)**		**Error (%)**
	GMsFEM	FEM (fine-scale)	
BENDING I	86.4	85.3	1.28
BENDING II	512.7	505.7	1.38
TORSION I	741.5	733.3	1.11
AXIAL I	1227.7	1221.8	0.48
BENDING III	1334.5	1313.6	1.59
TORSION II	2235.9	2201.7	1.55

between the GMsFEM and FEM solutions indicates the ability of the multiscale model to capture the dynamics of the system within the considered frequency range. This conclusion is corroborated by the results shown in Fig. 24 which illustrate the transient response of the beam excited by a step-function load applied at the tip (see Fig. 21). In order to show both the transient and steady state response of the system, a 0.4% stiffness proportional damping is used.

It is also interesting to note how the GMsFEM frequencies reported in Table 1 systematically overestimate the values predicted by the refined model. This phenomenon is associated with the compatibility conditions between adjacent MSEs that constrain the solution over the elements' faces, and tend to overestimate the element stiffness. This produces small inaccuracies when the wavelength of deformation is large compared to the element's size (as in this case), but can potentially induce large errors otherwise. This phenomenon is illustrated in the third column of Table 2 which shows that the relative error between GMsFEM and FEM results rapidly increases when higher modes are considered.

A possible solution to this issue is intrinsically embedded in the GMsFEM method itself that allows one to include, for example, additional coarse-scale DOFs in the definition of a MSE. For instance, a refined multiscale element, featuring 1244 nodes,

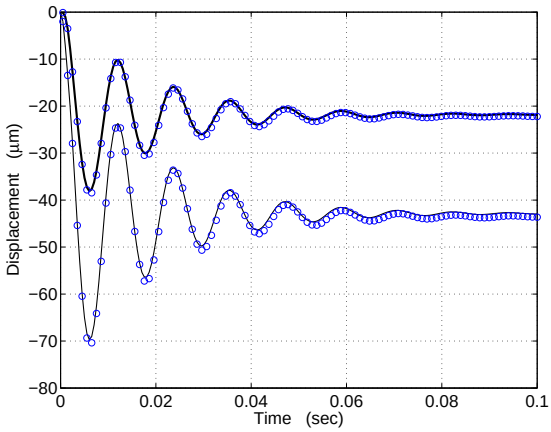

(a) Displacement u_x

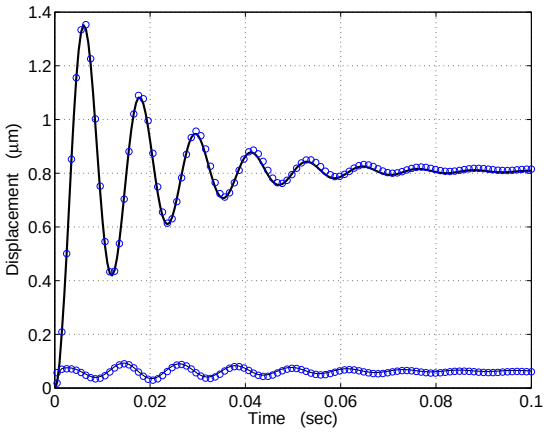

(b) Displacement u_y

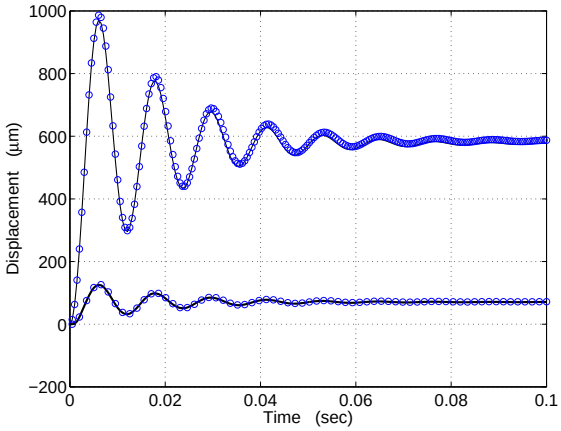

(c) Displacement u_z

Figure 24: Transient response of the beam computed with GMsFEM at sensor S_1 (thick line), sensor S_2 (thin line), and fine-scale FEM results (O-markers).

is defined by including additional coarse-scale DOFs selected over the boundary faces of the MSE shown in Fig. 22.a. The first 40 natural frequencies obtained with this refined element are presented in the fourth column of Table 2. Also in this case, the eigensolutions associated with repeated modes are presented only once. Results show that the refined element accurately predicts the eigenvalues of the system in a wider frequency range compared to the previously adopted multiscale element. As expected, results also show that increasing the number of coarse-scale nodes also reduces the error associated to the lower-frequency modes.

Such approach is clearly more computationally expensive since it increases the

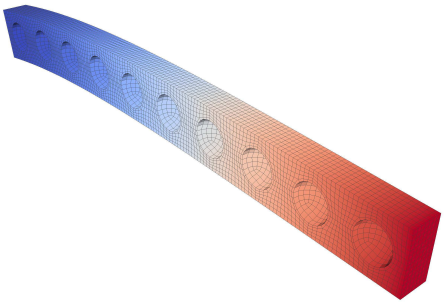

(a) First bending mode (86.4 Hz)

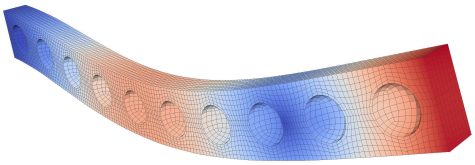

(b) Second bending mode (512.7 Hz)

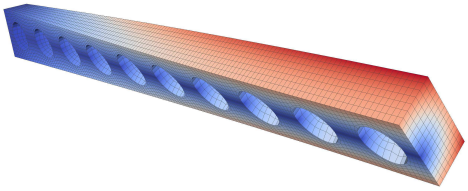

(c) First torsional mode (741.5 Hz)

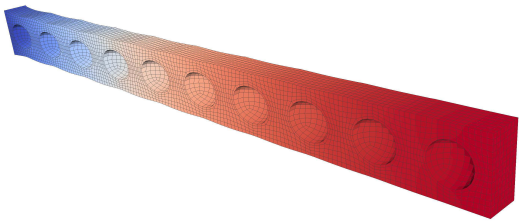

(d) First axial mode (1227.7 Hz)

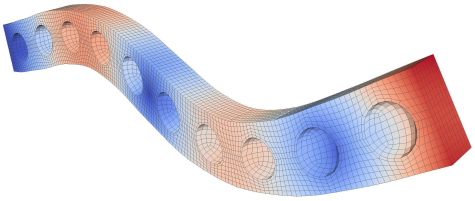

(e) Third bending mode (1334.5 Hz)

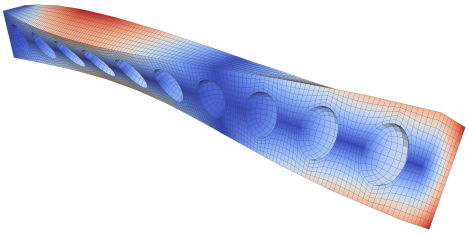

(f) Second torsional mode (2235.9 Hz)

Figure 25: Mode shapes of the beam computed using 10 multiscale elements. For visualization purposes the coarse-scale solution in projected onto the fine-scale mesh.

number of nodes for which multiscale shape functions are computed, and also increases the number of DOFs explicitly retained in the coarse-scale model. It is however interesting to note that the size of the final system, comprised of 1244 global nodes, is significantly smaller compared to the 32655 nodes characterizing the entire fine-scale model. Also, the calculation of the multiscale shape functions is an operation that is done only once in the pre-processing stage of the simulation, and is not repeated if multiple analysis are conducted for different loading or boundary conditions.

2.5 Conclusions

This chapter presents the theoretical formulation of the geometric multiscale finite element method (GMsFEM). Multiscale elements are derived from the minimization of the energy of the system, and linear constraints are implemented in order to guarantee compatibility of displacements across adjacent elements. A formalism is proposed to investigate the issue of inter-element compatibility that is particularly relevant when implementing three-dimensional multiscale elements. Numerical examples illustrate the ability of GMsFEM to pass the patch test, and to provide compatible solutions across the boundaries of dissimilar elements. In this regard, the effects of different types of fine-scale elements are investigated in order to support the theoretical predictions. Numerical results computed for three-dimensional heterogeneous structures illustrate how GMsFEM allows to model fine-scale geometrical features by means of a limited number of global information. As expected, the GMsFEM performs well when the wavelength of deformation is larger than the relevant small-scale features of the problem and offers a systematic approach to capture the response of the system at higher frequencies.

Table 2: Natural frequencies computed with coarse (704 nodes), and fine (1244 nodes) MSEs, and comparison with the fine-scale FEM solution (32655 nodes). The bracketed values indicate the % error between GMsFEM and FEM results.

Mode number	**Natural frequencies (Hz)**		
	FEM	GMsFEM - coarse	GMsFEM - fine
1	85.33	86.38 (1.23)	85.73 (0.47)
3	505.7	512.6 (1.37)	508.2 (0.50)
5	733.3	741.5 (1.11)	729.1 (0.56)
7	1221	1227 (0.48)	1224 (0.25)
8	1313	1334 (1.58)	1320 (0.55)
10	2201	2235 (1.55)	2188 (0.59)
11	2352	2398 (1.95)	2367 (0.65)
13	3540	3628 (2.51)	3568 (0.79)
15	3615	3692 (2.12)	3651 (0.98)
16	3655	3764 (2.98)	3670 (0.40)
17	4814	4972 (3.28)	4862 (1.00)
19	5060	5348 (5.70)	5118 (1.16)
20	6056	6182 (2.07)	6100 (0.72)
21	6131	6390 (4.23)	6208 (1.26)
23	6503	7008 (7.77)	6593 (1.38)
24	7451	7844 (5.27)	7569 (1.58)
26	7943	8706 (9.60)	8076 (1.66)
27	8396	8756 (4.29)	8494 (1.17)
28	8720	9257 (6.15)	8892 (1.96)
30	9381	10435 (11.2)	9569 (2.00)
31	9801	10436 (6.47)	10033 (2.36)
33	10628	11264 (5.98)	10707 (0.75)
34	10815	12461 (15.2)	10964 (1.38)
35	12241	13829 (12.9)	12460 (1.79)
36	12675	14215 (12.1)	12856 (1.43)
37	12883	14906 (15.7)	13135 (1.95)
39	13298	15273 (14.8)	13558 (1.96)

CHAPTER III

MULTISCALE ANALYSIS OF PERIODIC SOLIDS

3.1 Overview

In this chapter, the GMsFEM is applied to the analysis of periodic material configurations. The wave propagation properties of periodic materials and structures are described through the application of Bloch formalism. This leads to the dispersion relations of the system that fully characterize its wave properties in terms of frequency/wavenumber relations, equivalent constitutive behavior at long wavelengths, and wave velocities of propagation. Results computed with GMsFEM are compared with reference FEM solutions to characterize the computed multiscale solutions, and to identify advantages and shortcomings of the method.

The following section summarizes the Bloch theorem and its application to the analysis of free wave motion in periodic structures. The chapter continues with applications of GMsFEM to two- and three-dimensional periodic solids, such as lattices and a phononic crystal plate. The dispersion properties of the latter are validated through experimental measurements conducted on an assembly of finite size.

3.2 Free wave propagation in periodic solids

3.2.1 Unit cell analysis: Bloch theorem

The propagation of elastic waves in periodic systems is conveniently described through the Bloch formalism [26], briefly summarized in what follows. As shown in Fig. 26, a periodic medium is uniquely defined by a set of lattice vectors $(\boldsymbol{e}_1, \boldsymbol{e}_2)$ that generate the periodic pattern. Given $(\boldsymbol{e}_1, \boldsymbol{e}_2)$, the position vector $\boldsymbol{r}_p$ of a generic point P within

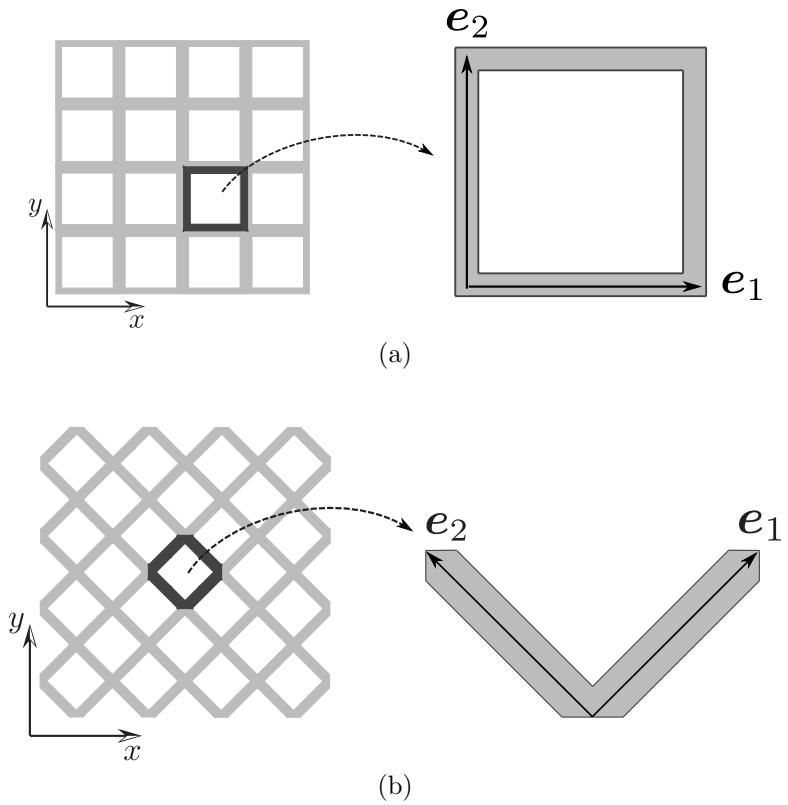

Figure 26: Periodic systems with Cartesian (a) and skew (b) lattice vectors.

cell (n_1, n_2) can be expressed as:

$$\boldsymbol{r}_p = \boldsymbol{r}_{p0} + n_1\boldsymbol{e}_1 + n_2\boldsymbol{e}_2 \tag{50}$$

where $\boldsymbol{r}_{p0}$ is the position of point P in the reference cell, and n_1, n_2 are integers. According to the Bloch theorem, the displacement of point $\boldsymbol{r}_p$ can be expressed in terms of the displacement $\boldsymbol{r}_{p0}$ in the reference unit cell:

$$\boldsymbol{u}(\boldsymbol{r}_p) = \boldsymbol{u}(\boldsymbol{r}_{p0})\, e^{i\boldsymbol{k}\cdot(\boldsymbol{r}_p - \boldsymbol{r}_{p0})} \tag{51}$$

where

$$\boldsymbol{u}(\boldsymbol{r}_{p0}) = \boldsymbol{u}_0\, e^{i(\omega t - \boldsymbol{k}\cdot\boldsymbol{r}_{p0})} \tag{52}$$

In Eq. (52), $i = \sqrt{-1}$ denotes the imaginary unit, ω is the frequency of wave propagation (rad/s), and $\boldsymbol{k}$ is the wave vector. Substituting Eq. (50) into Eq. (51) gives:

$$\boldsymbol{u}(\boldsymbol{r}_p) = \boldsymbol{u}(\boldsymbol{r}_{p0})\, e^{i(n_1\mu_1 + n_2\mu_2)} \tag{53}$$

where $\mu_i = \boldsymbol{k} \cdot \boldsymbol{e}_i$ with $i = 1, 2$. Eq. (53) states that in a periodic system the change in amplitude that a wave experiences as it propagates from one cell to another does not depend on the specific location of the cell within the system, and thus the analysis can be restricted to the reference unit cell or representative volume element (RVE).

3.2.2 Finite element analysis of free wave motion

The dynamic behavior of the unit cell is studied with the proposed multiscale finite element method. The discretized equations of motion of the reference cell are derived through standard FE procedures [38] in conjunction with the multiscale discretization technique described in Chapter II. If the structure undergoes harmonic motion at frequency ω, the equations of motion for the cell are given by:

$$\left[\boldsymbol{K} - \omega^2 \boldsymbol{M}\right] \boldsymbol{d} = \boldsymbol{f} \tag{54}$$

where $\boldsymbol{M}$ and $\boldsymbol{K}$ denote the global mass and stiffness matrices of the unit cell, $\boldsymbol{d}$ is the vector of generalized displacements, and $\boldsymbol{f}$ denotes generalized forces of interaction of the cell with its neighbors. The propagation of elastic waves from one cell to another is studied by imposing compatibility and equilibrium conditions between the boundary nodes of the cell, and assuming that only the interaction forces with neighboring cells appear in $\boldsymbol{f}$. Periodic boundary conditions are commonly written in matrix form as:

$$\boldsymbol{d} = \boldsymbol{\mathcal{A}}(\mu_1, \mu_2)\, \boldsymbol{d}_r \quad \text{and} \quad \boldsymbol{f} = \boldsymbol{\mathcal{B}}(\mu_1, \mu_2)\, \boldsymbol{f}_r \tag{55}$$

where matrices $\boldsymbol{\mathcal{A}}$ and $\boldsymbol{\mathcal{B}}$ are transformation operators between $\boldsymbol{d}$ and $\boldsymbol{f}$, and the corresponding vectors of reduced order $\boldsymbol{d}_r$ and $\boldsymbol{f}_r$. Explicit expressions for $\boldsymbol{\mathcal{A}}$ and $\boldsymbol{\mathcal{B}}$ can be written in relation to specific arrangements of the fundamental unit cell [58, 107]. Substituting Eq. (55) into Eq. (54), pre-multiplying the resulting equation for $\boldsymbol{\mathcal{A}}^H$, with $(\,)^H$ denoting the Hermitian operator, and assuming that no external forces are applied, gives:

$$\left[\boldsymbol{K}_r(\mu_1, \mu_2) - \omega^2 \boldsymbol{M}_r(\mu_1, \mu_2)\right] \boldsymbol{d}_r = \boldsymbol{0} \tag{56}$$

where $\boldsymbol{K}_r = \boldsymbol{\mathcal{A}}^H \boldsymbol{K} \boldsymbol{\mathcal{A}}$, and $\boldsymbol{M}_r = \boldsymbol{\mathcal{A}}^H \boldsymbol{M} \boldsymbol{\mathcal{A}}$. The eigenvalue problem given by Eq. (56) requires imposing the two components of the wave vector and solving for the corresponding frequency of wave propagation $\omega = \omega(\mu_1, \mu_2)$. The complete solution for varying μ_1 and μ_2 defines the dispersion surfaces of the medium. In the present analysis, wave propagation without attenuation is considered. Hence, μ_1 and μ_2 are purely imaginary numbers that vary within the first Brillouin zone of the system [30]. Each surface describes the dispersion relation for each wave mode. The total number of dispersion surfaces equals the size of the eigenvalue problem in Eq. (56), which in turn depends on the number of reduced degrees of freedom $\boldsymbol{d}_r$. The computational cost for the evaluation of the dispersion diagrams can be significantly reduced by exploiting the proposed multiscale method, which allows elements to be formulated that retain only the relevant boundary or internal DOFs for characterizing the dynamics of the system in a selected frequency range. It is common practice to let the wave vector span the contour of the irreducible part of the Brillouin zone [30] to obtain dispersion diagrams. Examples of possible representations of the dispersion diagrams are presented for selected examples in the following sections.

3.3 Solid with periodic hard inclusions

3.3.1 Configuration

As illustrated in Fig. 27.a, the configuration considered herein consists of a square domain made of an isotropic material (E=71 GPa, ρ=2700 kg/m^3, and ν=0.3) with a periodic arrangement of circular fibers. The inclusions are ten times stiffer and heavier than the surrounding matrix. The corresponding unit cell, shown in Fig. 27.b, features side length L=1.0 m long and a central circular fiber with diameter $d = 0.3\,L$. On the spirit of h-refinements, the RVE is discretized using three GMsFEM meshes as shown in Fig. 28.a,b,c.

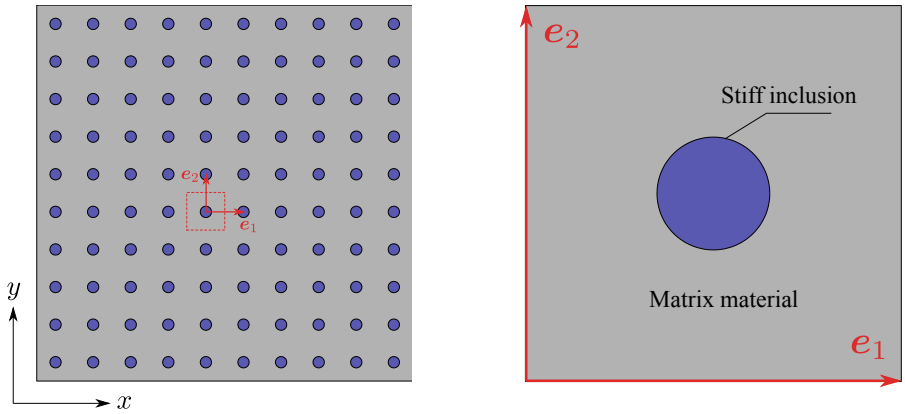

(a) (b)

Figure 27: Periodic arrangement of stiff fibers in a uniform matrix (a) and representative unit cell (b).

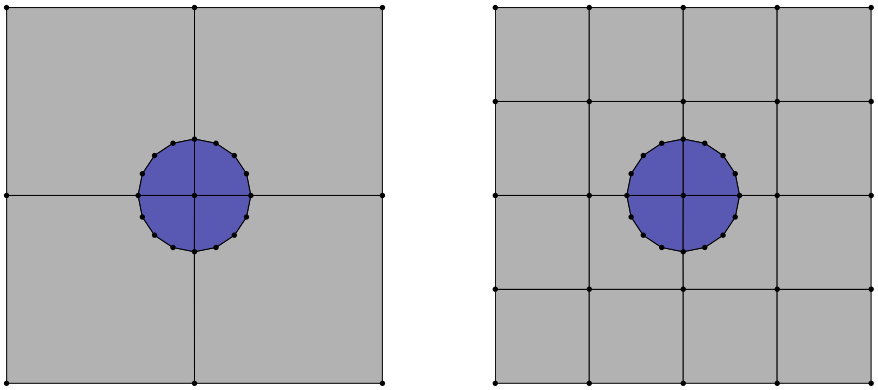

(a) MSE-A: 25 nodes (b) MSE-B: 41 nodes

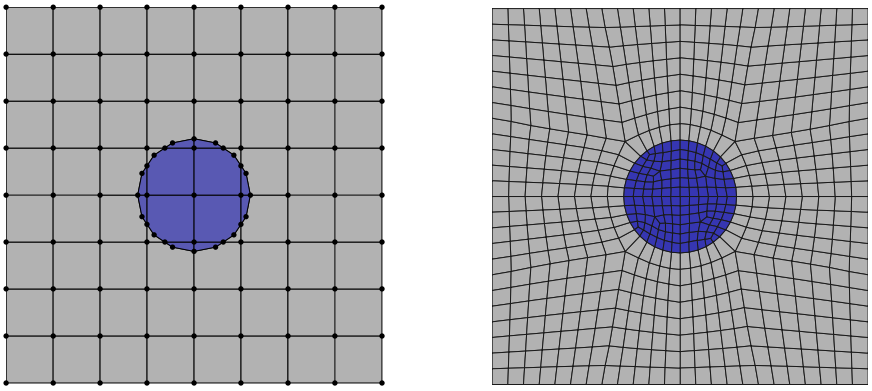

(c) MSE-C: 105 nodes (d) FEM mesh: 805 nodes

Figure 28: Multiscale and standard FEM discretizations used to model the RVE.

A FE discretization of the domain, shown in Fig. 28.d, is used to compare the computed results. The number of elements in the FE mesh is chosen to correctly describe the inclusion's boundary using a smooth discretization. Furthermore, increasing the number of elements does not significantly change the dispersion relations of the first five wave modes in the frequency range below 3.5 kHz.

3.3.2 Numerical results: band diagrams and wave modes

Results of the dispersion analysis are shown in Fig. 29 that illustrates the change of the first five wave modes over the contour of the irreducible Brillouin zone. Specifically,

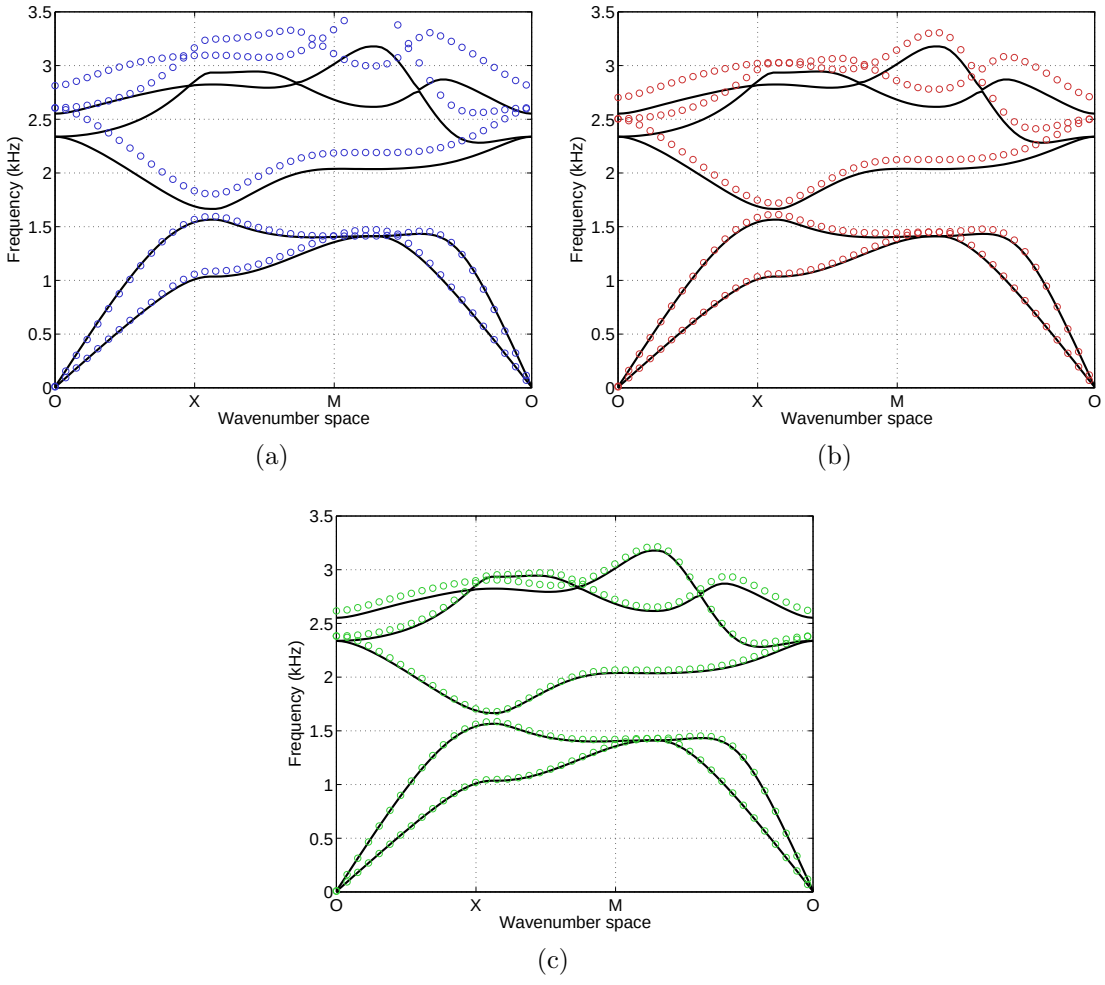

Figure 29: Band diagrams of the system computed with GMsFEM (o-markers) using MSE-A (a), MSE-B (b), and MSE-C (c). FEM solution (thick solid line).

Fig. 29.a shows excellent agreement between the dispersion curves of the first two modes obtained with the coarsest GMsFEM mesh (Fig. 28.a) and the corresponding FEM solution. The first two modes are in fact typically characterized by a global deformation pattern of the cell that is captured even by the coarsest GMsFEM discretization. The same results also highlight discrepancies on the high frequency modes, typically characterized by local deformations within the RVE itself. In this case the linear compatibility conditions between multiscale elements tend to overstiffen the model therefore impeding the proper estimation of the Bloch's eigenvectors and associated frequencies. Figures 29.b,c illustrate how convergence at higher frequencies is achieved by means of successive mesh refinements that allow capturing the localized deformation patterns typical of higher frequency modes. This interpretation is further supported by results shown in Fig. 29 that illustrate the first five eigenmodes computed when $\mu_1 = \mu_2 = \pi$. Results computed using different discretizations show that the first two eigenmodes computed with the coarsest MSE (see Fig. 28.a) are in good agreement with the corresponding FE solutions, while discrepancies are observed for modes characterized by complex deformation patterns within the cell. A better agreement at higher frequencies is observed when MSEs are utilized in conjunction with additional quadrilateral elements, shown in Fig. 28.b,c, so that also localized deformations within the cell can be correctly captured.

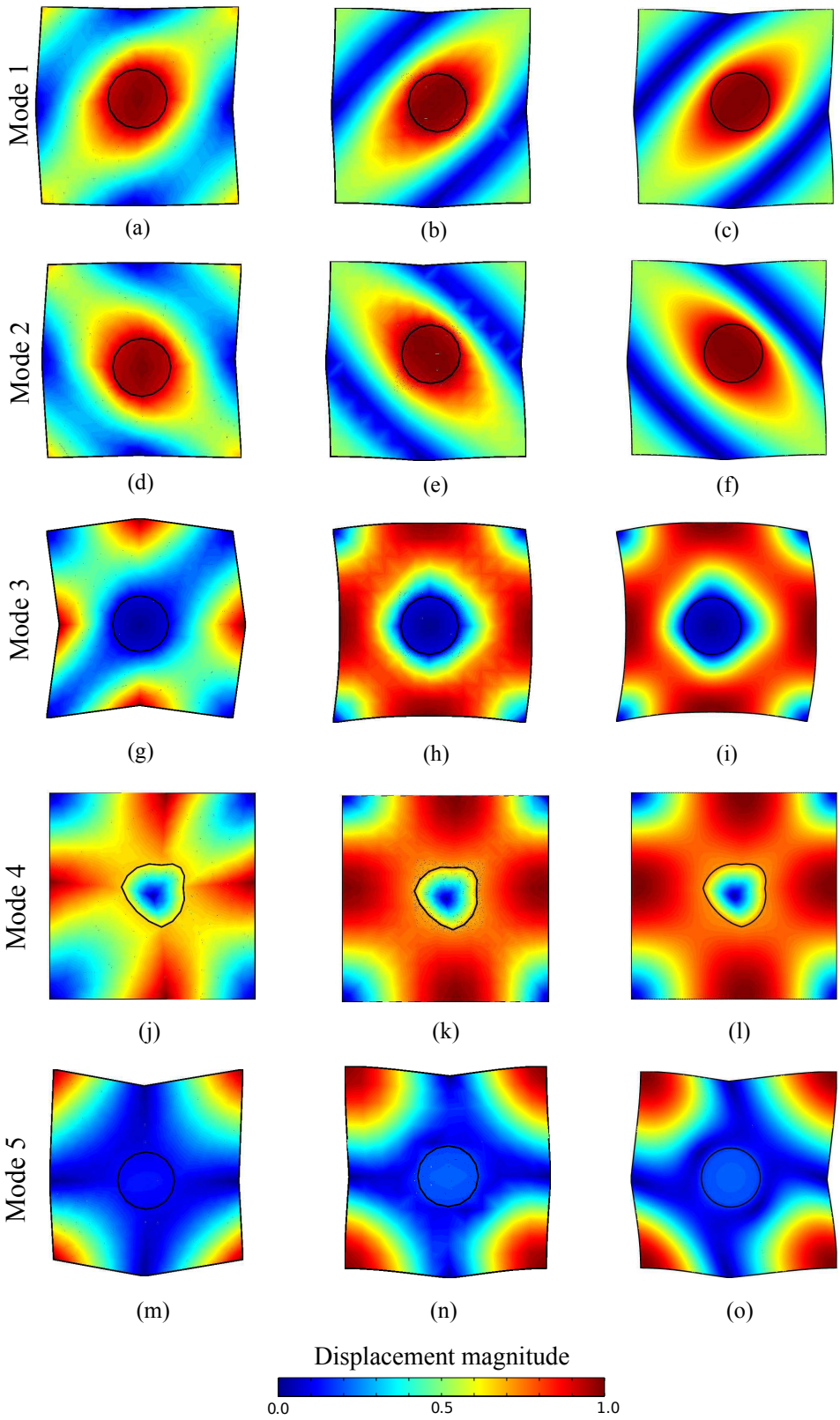

Figure 30: Bloch eigenvectors of the first five modes computed with GMsFEM-A (a,d,g,j,m), GMsFEM-C (b,e,h,k,n), and FEM results (c,f,i,l,o).

3.4 Structural lattices

In this example, the GMsFEM is applied to compute the wave propagation properties of 2D periodic lattices. In the low frequency range, when the wavelength of deformation is larger than the unit cell of the lattice, such systems behave as equivalent media with anisotropic properties that can be exploited for the design of structures with directional wave properties. In this frequency range, the lattice is characterized by global deformation modes that are influenced by the specific cell's topology. As discussed in the previous example, this is a favorable scenario for the application of GMsFEM to reduce the computational costs of simulations aimed at characterizing the directional wave properties of the lattice.

3.4.1 Configuration

A schematic of the considered lattice topology is shown in Fig. 31.a along with the unit cell illustrated in Fig. 31.b. The unit cell features side length L=0.5 mm, and aluminum ligaments oriented at θ=45 deg with respect to the cartesian frame ($\boldsymbol{i}_1$, $\boldsymbol{i}_2$). As shown in Fig. 32.a, the unit cell is discretized by means of a limited number of

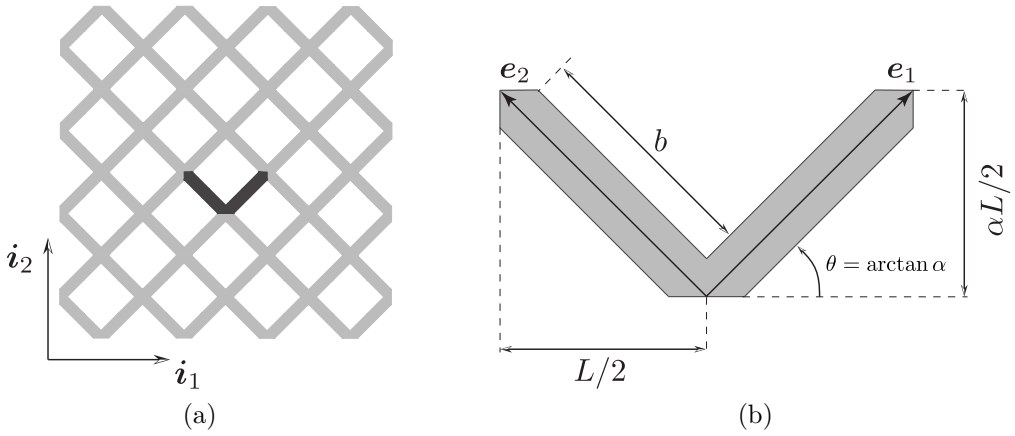

Figure 31: Considered lattice structure (a) and representative unit cell (b).

multiscale elements that significantly reduce the coarse scale DOFs retained in the simulation. Also, the present approach allows for a better positioning of the global nodes along the boundary of the cell and therefore facilitates the implementation of

periodic boundary conditions. On the other hand, a higher number of elements is typically required when a triangular mesh is used to discretize the same topology, as shown in Fig. 32.b.

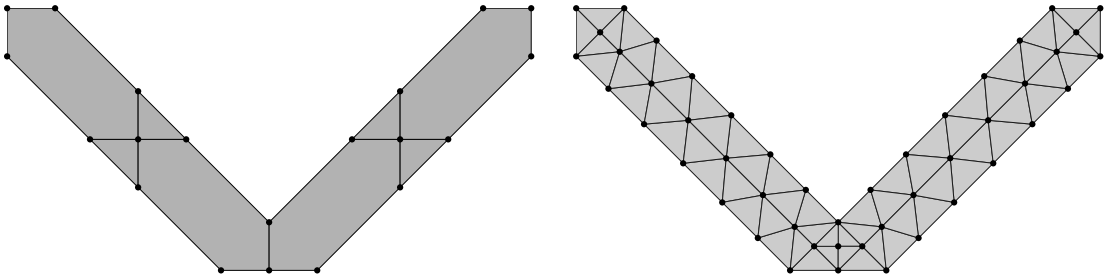

(a) GMsFEM mesh (20 nodes) (b) FEM mesh (47 nodes)

Figure 32: Discretization of the unit cell: GMsFEM (a), and FEM (b).

3.4.2 Band diagrams and wave velocities

Wave propagation in the considered lattice is analyzed through the calculation of the wave speeds of the first two low frequency modes [58, 107]. In the long wavelength region the lattice is characterized by a linear dispersion relation, as shown in Fig. 33, that denotes the non-dispersive nature of the medium. In this example,

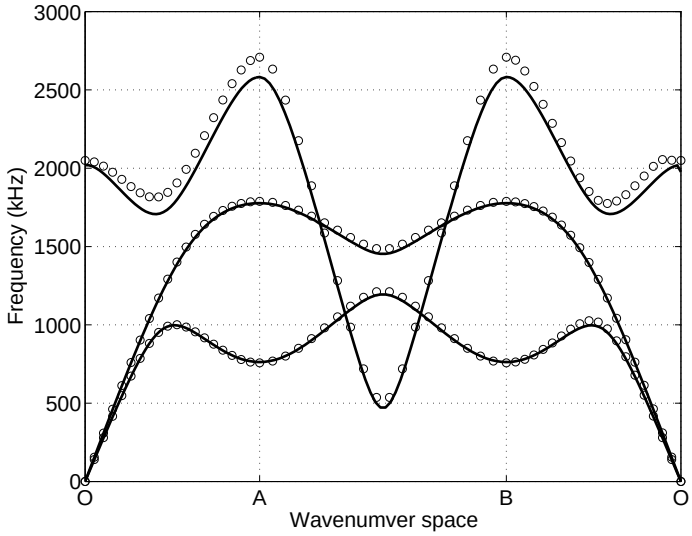

Figure 33: Band diagrams of the three low-frequency modes of the considered lattice. FEM solution (thick solid line), GMsFEM results (o-markers).

such region extends approximately between 0 and 500 kHz where Fig. 33 shows an excellent agreement between GMsFEM and FEM results. Results also illustrate that, contrary to classical homogenization methods, GMsFEM correctly captures the dispersion relations of the system beyond the long wavelength region, in the frequency range between 500 kHz and 1800 kHz. As expected, discrepancies between the predicted results and the FEM solution appear in the higher portion of the considered frequency spectrum.

To characterize the directional behavior of structural lattices, it is common practice to investigate the dependence of wave velocities upon directions of propagation. The evaluation of wave speeds provides important indications on the anisotropic nature of the lattice within a specified frequency range. It shows the existence of preferential directions of propagation and energy flow, and defines the dispersive nature of the medium. For instance, the phase velocity at a given frequency ω is given by:

$$\boldsymbol{c}_{ph} = \frac{\omega}{\kappa}\,\boldsymbol{v} \tag{57}$$

where $\kappa = |\boldsymbol{\kappa}|$ is the wavenumber, and $\boldsymbol{v} = \boldsymbol{\kappa}/\kappa$ is a unit vector in the direction of the wave vector.

It is particularly interesting to investigate the directivity of the phase speeds in the long wavelength region that for the lattice considered herein extends from 0 to 500 kHz. In such a frequency range the structure behaves as a homogeneous medium with effective properties that can be correlated to the lattice skewness and void volume fraction. Furthermore, because of the non-dispersive nature of the system, the wave velocities and effective properties are independent of frequency. The phase speeds of the first two wave modes computed in the long wavelength regime are shown in Fig. 34. Results indicate that the first mode tends to propagate faster along the 0-90 deg direction, while the second mode is characterized by higher speeds at ± 45 deg. The dependency of wave speeds from the direction of propagation reveals the effective anisotropic response of the lattice in the considered frequency range. Contrary to

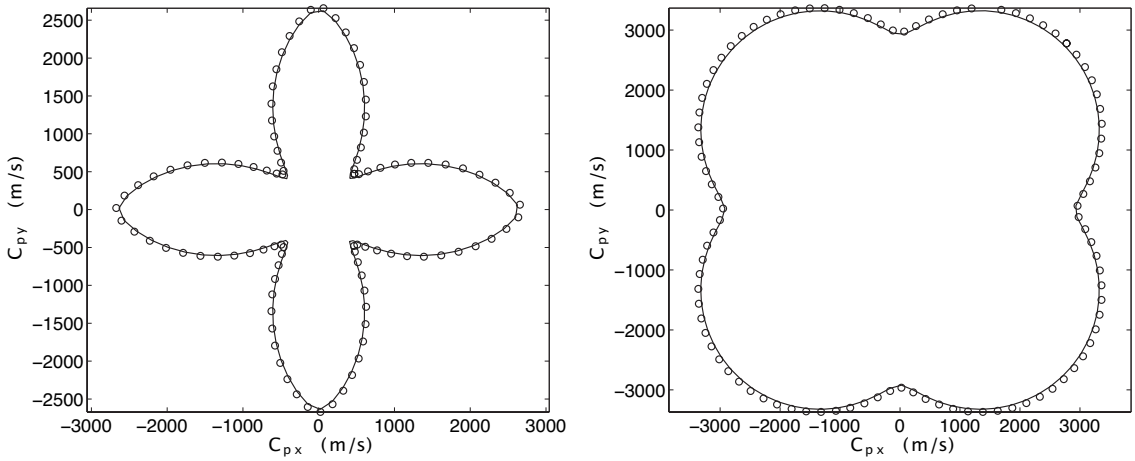

(a) Mode 1 (b) Mode 2

Figure 34: Phase speed of the first wave mode (a) and of the second wave mode (b) computed with FEM (thin solid line) and GMsFEM (o-markers).

composite materials, such anisotropic behavior is correlated to the lattice's topology, even if the ligaments are made of an isotropic material.

Results presented in Fig. 34 also illustrate the excellent agreement between the GMsFEM and FEM solutions. As shown in Fig. 32, the proposed method allows discretizing the unit cell with a significantly smaller number of nodes thus the computational cost is reduced accordingly. Note that the complete description of the dispersion properties requires the sequential solution of Eq. (56) for different values of μ_1 and μ_2. In this case, GMsFEM is particularly appealing because the additional computational cost associated with calculation of the multiscale shape functions is computed only once to assemble the global matrices, while a reduced number of DOFs is explicitly retained in the subsequent analysis.

3.4.3 Transient response of finite lattices

Results predicted by the unit cell analysis are verified by computing the time response of 2D grids of finite size. The structures are composed of 15 cells in the x and y directions. The lattice is excited by a narrowband 10-cycle tone burst signal centered at a frequency of 100 kHz as shown in Fig. 35.b. The frequency spectrum of

the load is entirely confined in the low-frequency region where the structure behaves as effective anisotropic medium. Four forces are simultaneously applied at the nodal points of the central cell in order to uniformly excite the system in all directions, as illustrated in Fig. 35.a. The response is evaluated by integrating the equations of mo-

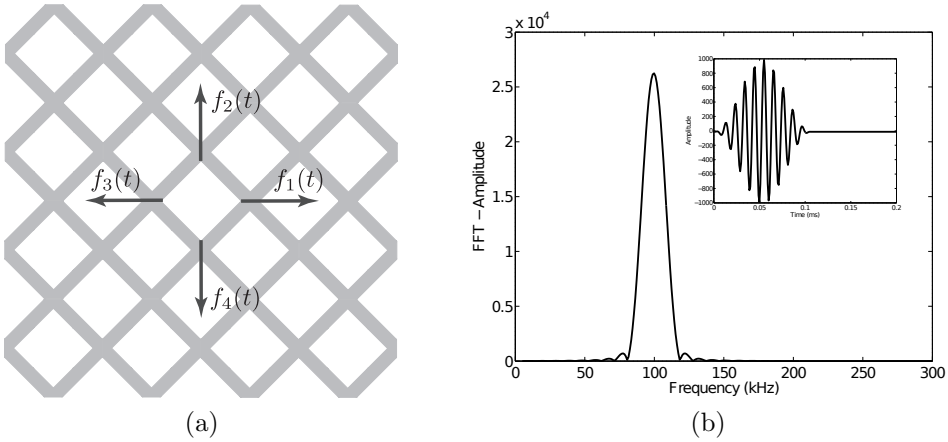

(a) (b)

Figure 35: Spatial arrangement (a), and time variation (b) of the nodal forces applied to the lattice.

tion of the assembly with a time marching scheme of the Newmark family [101] using displacement-free boundary conditions at the edges of the computational domain.

Results presented in Fig. 36 illustrate snapshots of the displacement field captured before observing reflections from the boundaries. This allows investigating the response of the lattice ignoring the effects of specific boundary conditions. As predicted by the unit cell analysis, the system is characterized by a significant directional behavior whereby elastic energy tends to be focused along the ligaments of the lattice. Results are presented side-by-side to emphasize the agreement between the GMsFEM and FEM solutions.

The GMsFEM allows for integration of the dynamic equations of the problem in about 5.5 sec, while 36 sec are required to integrate the FE system. Such CPU times are evaluated considering 200 time-steps, and using the same implementation of the time marching scheme. Clearly, GMsFEM is more advantageous since a smaller number of DOFs is explicitly retained in the time marching loop. The gap between

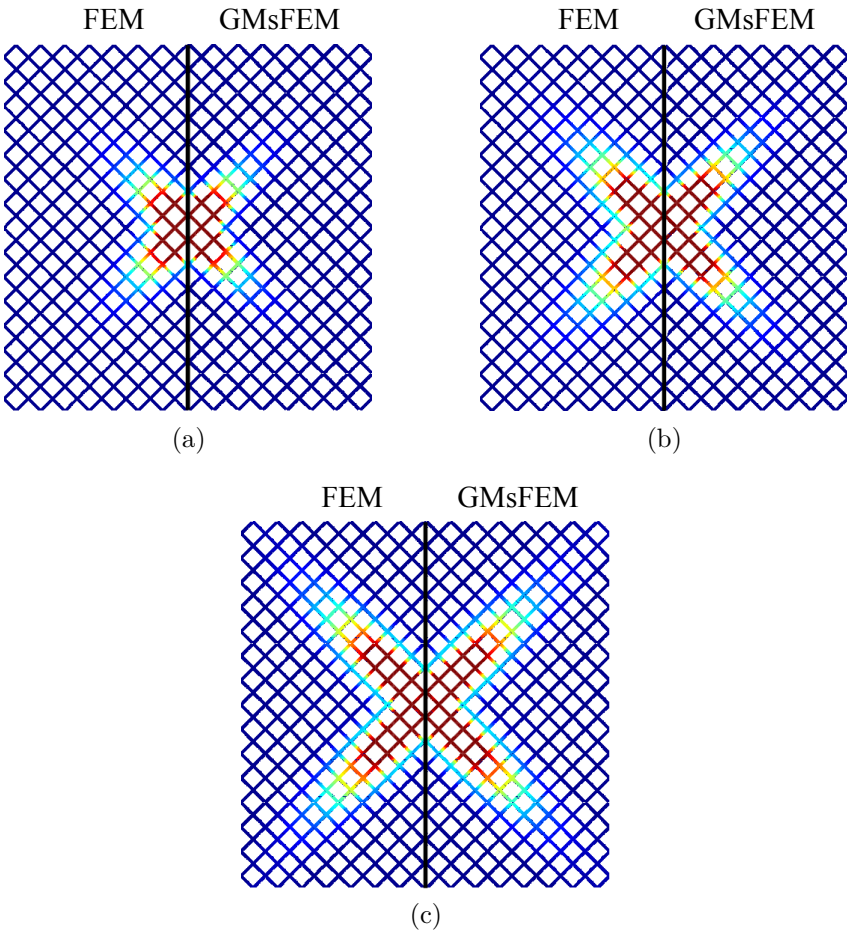

Figure 36: Magnitude of the displacement field for evolving time-steps.

the two approaches reduces if the CPU time required to compute the multiscale shape functions, (about 11 sec), is considered. However, it is important to underline that this operation is executed only once at the beginning of the analysis in order to assemble the global system matrices, and it is not repeated if simulations are conducted for different boundary or loading conditions.

3.5 Phononic stubbed plate

Acoustic bandgaps characterize the propagation of Lamb waves in plates having periodic variations of acoustic properties, commonly known as phononic crystal (PC) plates. The existence of bandgaps, or frequency ranges in which acoustic-wave propagation is forbidden, is particularly appealing for the development, among others,

of acoustic logic ports, mechanical filters, and efficient acoustic waveguides [70, 93, 106, 127, 128]. The mechanical impedance mismatch between the periodic elements is a key factor for obtaining frequency bandgaps, which typically originate from wave scattering occurring at wavelengths of the same order of the unit cell size (Bragg scattering) [28]. The band structure of PC plates is commonly computed using approximate techniques such as the finite element method. This example shows the possibility of reducing the computational cost of simulations through the definition of multiscale elements capable of describing the salient physical features of the problem without fully resolving all the spatial scales. The configuration considered herein consists of a 2D periodic domain (Fig. 37) that is modeled using 3D elements thus representing a more challenging modeling scenario. Different multiscale elements are proposed in order to illustrate how the proposed multiscale method can be exploited to fit the needs of specific analyses.

3.5.1 Configuration

The considered structure, schematically shown in Fig. 37.a, consists of a thin aluminum plate (thickness $h_p = 1$ mm) characterized by a periodic distribution of cylindrical stubs bonded to one surface of the plate. As shown in Fig. 37.b the cylindrical

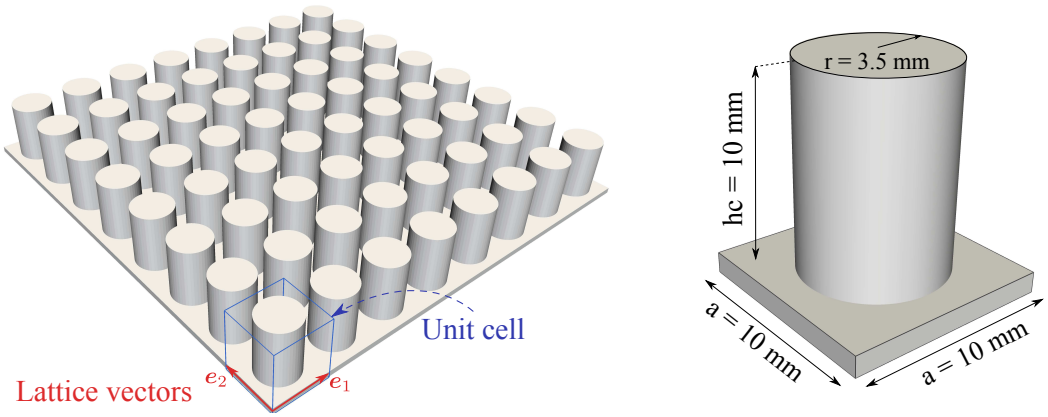

(a) Phononic crystal plate

(b) Representative unit cell

Figure 37: Phononic crystal plate with a periodic stubbed surface (a), and corresponding unit cell (b).

stubs feature a diameter $d = 7$ mm, height $h_c = 10$ mm, and are arranged in a square lattice with a lattice constant $a = 10$ mm. An interesting feature of this configuration, already investigated by Wu et al. [127], is the presence of a complete bandgap that extends from 114 to 143 kHz, and two additional partial bandgaps centered at 21 kHz and 110 kHz respectively.

In this study, the unit cell is modeled by means of two multiscale elements, shown in Fig. 38, each being characterized by a different number of global nodes. For instance, Fig. 38.a illustrates a 288-node MSE, denoted as multiscale element A, characterized by global nodes located over the four sides of the plate and along the peripheral edges of the cylinder. Also, Fig. 38.b shows a multiscale element (B) featuring 2595-global nodes representing an improved version, on the spirit of a p-refinement, of the previous MSE. Both MSEs are characterized by the same fine scale mesh comprised by 7704 elements. The dispersion properties of the unit cell computed with such discretization are in good agreement with results presented in [127]. For this reason, the resulting fine-scale solution is used as a reference to compare the GMsFEM predictions.

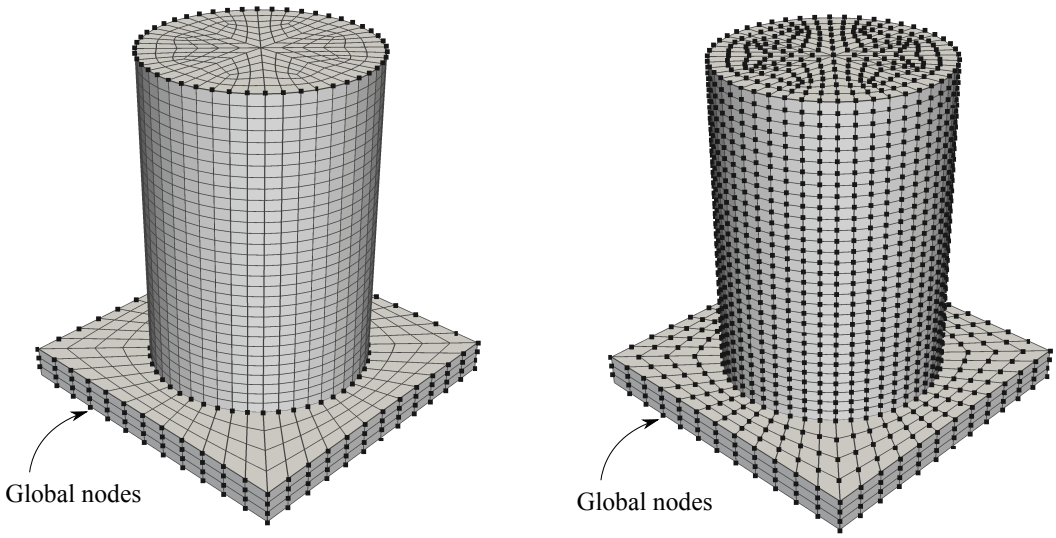

(a) Multiscale element A (b) Multiscale element B

Figure 38: Multiscale elements with 288 (a) and 2595 (b) coarse scale nodes.

3.5.2 Band diagrams

Multiscale elements A and B are used to compute the band diagrams of the considered unit cell in order to characterize the wave propagation properties of the phononic crystal plate. The computed results are compared with the FE solution obtained by explicitly resolving all the fine scale DOFs. For instance, results obtained with the multiscale element A are shown in Fig. 39.a illustrating how the adopted MSE fully captures the dispersion properties of the first three lower-frequency branches. Such wave modes are given by the combination of the fundamental symmetric (S_0), anti-symmetric (A_0), and shear horizontal (SH_0) Lamb modes that propagate in the plate and completely characterize the dynamic response of the PC plate below 25 kHz. In this frequency range, the behavior of the system is characterized by global deformation modes that are captured by the limited set of coarse scale nodes characterizing the adopted MSE. This considerations are further illustrated in Fig. 40 showing the excellent agreement between the first three Bloch eigenmodes computed at point X ($\mu_1 = \pi,\ \mu_2 = 0$) of the reduced wavenumber space using GMsFEM with MSE A and the fine scale FEM mesh. Also, Fig. 39.a shows how the multiscale element A is not able to describe the dispersion relations of the system at higher frequencies, and therefore is not a good candidate to model the bandgap behavior of the PC plate.

In order to overcome this limitation a second multiscale element (B) is proposed. Such MSE features a higher number of coarse scale nodes that provide a better description of the local deformation field characterizing high frequency modes. This is illustrated in Fig. 39.b, where the agreement extends to a broader frequency range. In particular, it is noteworthy to observe how multiscale element B provides an accurate description of the main bandgap of the system, even if minor discrepancies are observed above 200 kHz. This example demonstrates further how the GMsFEM is characterized by performance that balances the computational costs associated with

the numerical calculation of the multiscale shape functions to the specific requirements of the simulation.

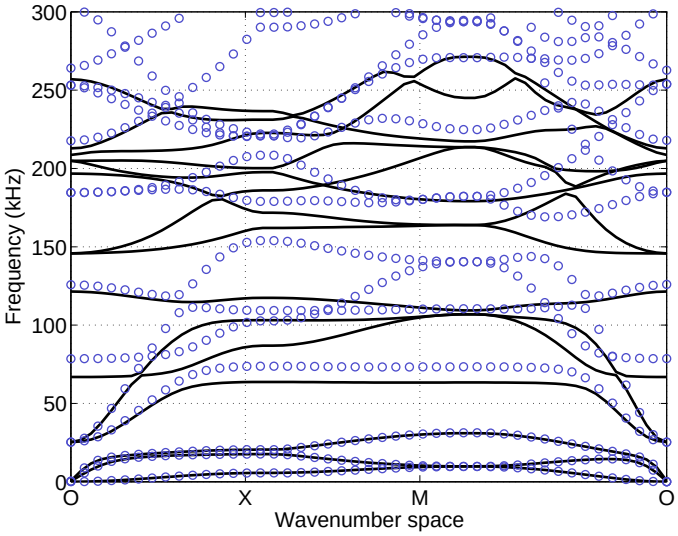

(a)

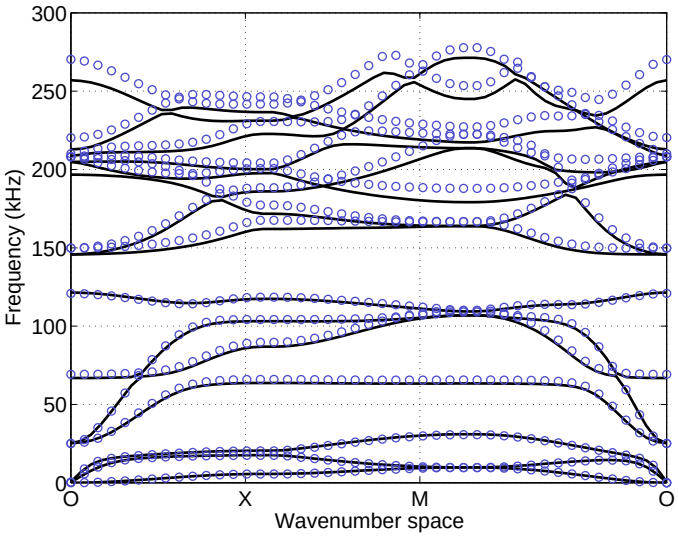

(b)

Figure 39: Band diagrams computed with MSE-A (a) and MSE-B (b) (O-markers) with comparison with the fine scale FEM solution (thick solid line).

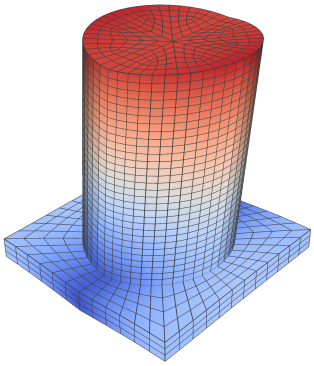

(a) Mode 1 (FEM)

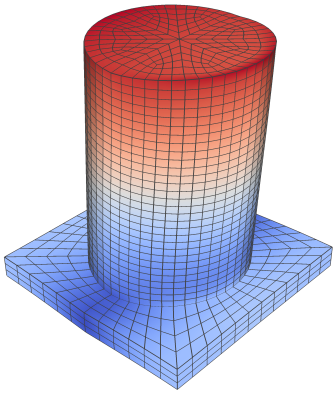

(b) Mode 1 (GMsFEM)

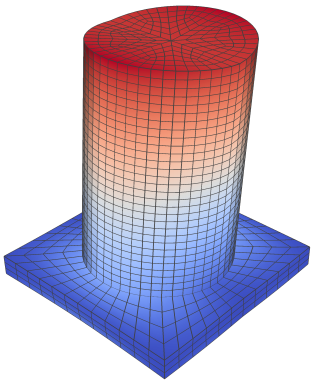

(c) Mode 2 (FEM)

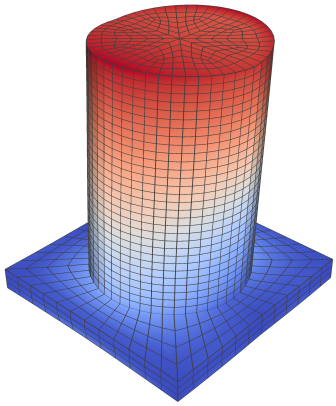

(d) Mode 2 (GMsFEM)

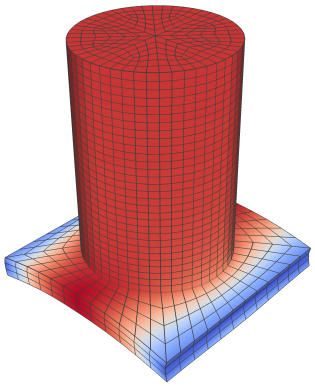

(e) Mode 3 (FEM)

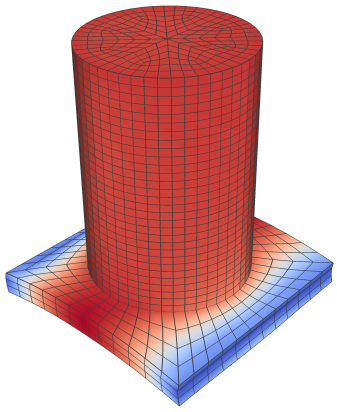

(f) Mode 3 (GMsFEM)

Figure 40: First three Bloch modes of the PC plate computed with the fine scale FEM mesh (a,c,e) and with MSE-A (b,d,f).

3.5.3 Experimental analysis of dispersion

In this section, the band structure computed numerically with the proposed multiscale elements are compared to experimental results characterizing the dispersion properties of a phononic crystal plate of finite size. The structure, shown in Fig. 41, is generated by the repetition of the RVE described in the previous section to form a periodic array of 6×20 units. Standard epoxy glue is used to bond the cylindrical stubs over the surface of the plate.

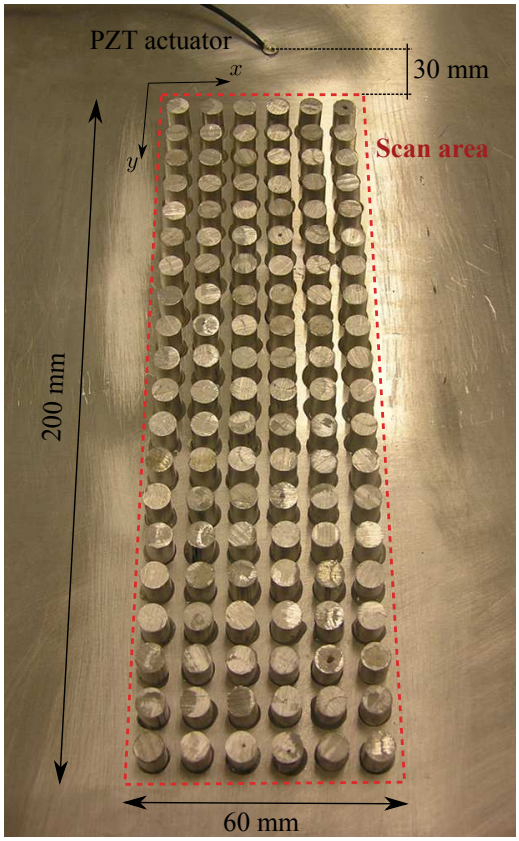

Figure 41: Experimental specimen of the phononic crystal plate.

The wave propagation properties of the structure are characterized by means of two-dimensional wavefield measurements, recorded with a scanning laser vibrometer (Polytec PSV-400). Measurements are conducted over a grid of 60×200 scan points with a spatial resolution of 1 mm in the horizontal and vertical directions. At each grid point, the laser measures the time history of the component of velocity $w(x, y, t)$

normal to the plate surface. Each time history includes 512 samples and is recorded at a sampling frequency of 1.28 MHz. Elastic waves are excited by a piezoelectric transducer located 30 mm away from the stubbed area as shown in Fig. 41. The transducer is driven by an input signal consisting of a four-cycle tone burst generated by a waveform generator (Agilent 33220A - 20MHz), and amplified by a piezo driver amplifier (Trek PZD 350). In order to uniformly actuate the system in de-

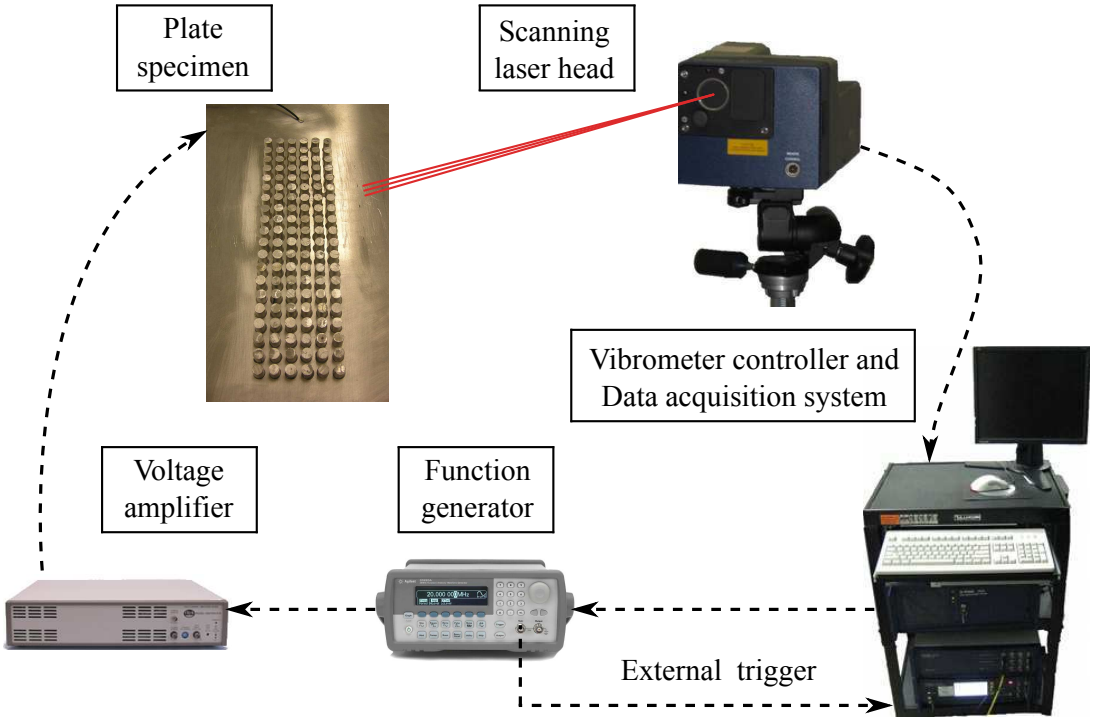

Figure 42: Schematic representation of the experimental apparatus.

sired frequency ranges, the plate is excited by three successive tone burst signals each centered at a frequency of 5 kHz, 15 kHz, and 40 kHz respectively. Three different measurements, one for each input signal, are sequentially conducted and the recorded displacements are summed into one single dataset. Such technique allows obtaining the response of the stubbed plate to an equivalent external input given by the sum of the three independently-applied loads.

The measured displacement is first transformed in the frequency domain ω through

the following Fourier Transform (FT):

$$\widehat{w}(x, y, \omega) = \mathcal{F}[w(x, y, t)]. \tag{58}$$

The resulting signal is then spatially averaged according to the following averaging procedure:

$$\widehat{w}(y, \omega) = \frac{1}{N_x} \sum_{i=1}^{N_x} \widehat{w}(x_i, y, \omega) \tag{59}$$

where $N_x = 60$ denotes the number of scan points along the width of the scanned area, identified by the x-direction in Fig. 41. A final FT along the y-direction (see Fig. 41) leads to the frequency-wavenumber representation of the averaged response ($\widehat{W}(k, \omega) = \mathcal{F}[\widehat{w}(y, \omega)]$).

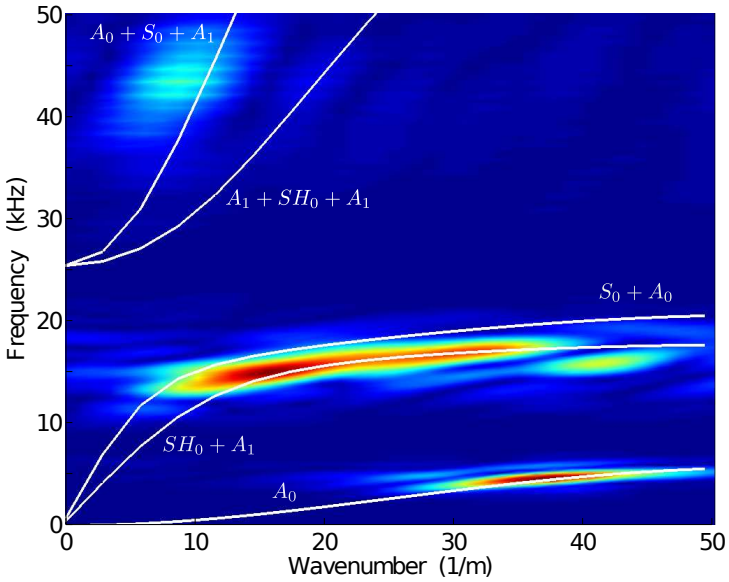

Figure 43: Experimental estimation of the dispersion curves of the considered phononic crystal. In white (solid lines) the wave branches computed with GMsFEM.

The amplitude of $\widehat{W}(k, \omega)$ is shown in Fig. 43. Specifically, Fig. 43 shows the comparison between the experimental (color scale) and numerical (solid lines) dispersion relations of the first five modes in a frequency range below 50 kHz. Results indicate how the numerical predictions tend to match the experimental dispersion branches identified by the peaks of $\widehat{W}$. A closer agreement is observed for the first and third modes that, being characterized by out-of-plane polarized displacements, are better

detected by the experimental apparatus. Also, the signature of the fifth branch is observed at 45 kHz while the fourth mode is hardly visible because of the absence of strongly out-of-plane polarized components.

A second measurement is performed in order to characterize the main bandgap of the PC plate. The same specimen is excited by a broadband chirp signal with frequency content between 70 kHz and 150 kHz. The dispersion relations of the plate are computed using the procedure previously described. Experimental results, illustrated in Fig. 44, reveal the presence of a full bandgap between 101 kHz and 132 kHz - about 15% lower than the corresponding theoretical values predicted by [127]. This discrepancy is attributed to the presence of the epoxy glue used to bond the stubs to the plate's surface, and to imperfections characterizing the height of each cylinder deriving from the manual cutting procedure used to produce the stubs from a longer bar. For instance, the average height of the stubs adopted in the experiment results about 1 mm shorter than the nominal value of 10 mm.

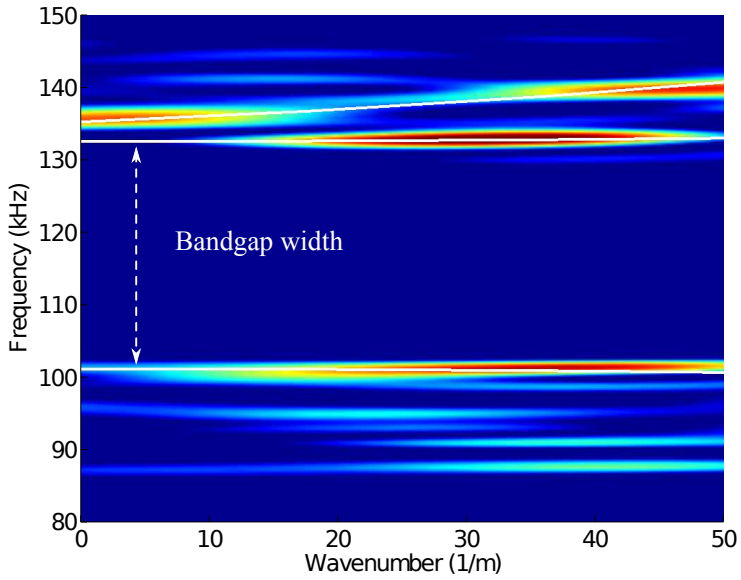

Figure 44: Experimental characterization of the bandgap of the PC plate. In white (solid lines) the wave branches computed with GMsFEM.

For a better agreement between numerical and experimental results, a possible strategy is to improve the experimental specimen. For instance, the stubs could be

cut more precisely by a water-jet automatic machine, and bonded to the plate's surface by friction welding as suggested in [127]. Since the prediction of the actual dispersion properties of this configuration is not the major purpose of the present study, the numerical model of the unit cell is adapted to the experimental configuration. In particular, a 0.3 mm thick layer of glue is added at the base of the multiscale element B (see Fig. 38.b), and the height of the stub is reduced to 9 mm. The glue is modeled by reducing the Young's modulus of the corresponding elements to 6 GPa as suggested in [5]. Whereas such changes do not appreciably affect the low frequency dispersion relations shown in Fig. 43, an excellent agreement of results is observed for the three main wave modes that define the bandgap as illustrated in Fig 44.

3.6 Conclusions

In this chapter GMsFEM is applied to the analysis of wave propagation in heterogeneous periodic media. In particular, two- and three-dimensional multiscale elements are adopted to study the free wave propagation properties of materials with periodic inclusions, structural lattices, and phononic crystal structures. These systems are characterized by unique dynamic properties, such as bandgaps, typically occurring at frequency ranges in which wavelengths are of the same order of the unit cell size, and wave directionality resulting from effective anisotropic behaviors in the low frequency/long wavelength regime. These important features can be correctly captured by the proposed multiscale elements. Extremely coarse multiscale elements accurately capture the global deformation modes characterizing the response of the system in the low frequency range. As the wavelength of deformations increases, additional global information are needed in order to represent localized deformations within the RVE. This can be achieved by coupling multiscale elements with a refined FE mesh, as shown in the first example, or by increasing the number of coarse scale nodes characterizing one single MSE, as demonstrated in the PC plate analysis.

Both strategies require a higher number of DOFs, thus increasing the computational cost of the analysis, and the time associated with the calculation of multiscale shape functions. The chapter concludes with the experimental validation of the dispersion diagrams computed with the proposed multiscale method. Numerical results are in good agreement with the measured data, especially in the low frequency range where wave modes are characterized by strongly out-of-plane polarized displacements that are better detected by the experimental apparatus. In order to predict the frequency range defining the major bandgap of the PC plate, the numerical model of the unit cell has been updated to reflect the details related to the realization of the experimental apparatus.

CHAPTER IV

APPLICATION TO DAMAGED STRUCTURES

4.1 Overview

Numerical simulations of wave-damage interaction play a key role for the development of modern guided wave-based inspection techniques. A concise yet meaningful understanding of these phenomena is often obtained by means of scattering diagrams illustrating the directivity of the wavefield scattered by defects. Such simulations are computationally intensive, not only due to the scale difference between the global and local features, but also because scattering information requires several parametric studies for damage of different size and orientation. Consequently, significant effort related to model preparation and re-meshing is required. The following sections illustrate how GMsFEM can be exploited to alleviate the modeling and computational costs of simulations involving small defects in an otherwise homogeneous system.

4.2 Plate with a circular hole

4.2.1 Configuration

The problem of wave propagation in a uniform plate with a central hole is studied first. Consider a square aluminum (E=71 GPa, ρ=2700 kg/m^3, and ν=0.3) plate with side length L=100 mm, characterized by a circular defect at the center. The multiscale nature of this problem is related to the difference between the characteristic length scales of the structure and the size of the hole (see Fig. 45). For instance, three diameters, $D_1 = 0.2$ mm, $D_2 = 1.0$ mm, and $D_3 = 2.0$ mm, are considered in order to represent a significant range of critical modeling scenarios. The computational domain is discretized with a grid of 40×40 linear quadrilaterals in order to properly capture the global wave motion at the given excitation frequency. The circular inclusions

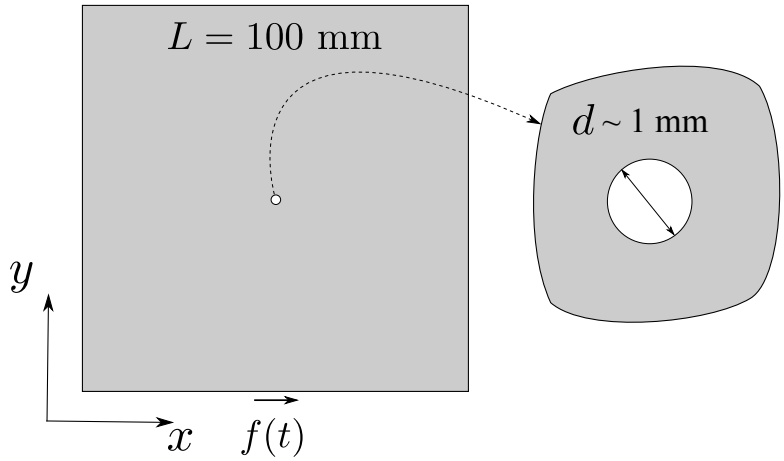

Figure 45: Schematic of the two-dimensional plate with central hole.

are modeled by means of one multiscale element as shown in Fig. 46. Each MSE is characterized by four "exterior" nodes that coincide with the nodes of adjacent linear quadrilaterals, and a variable number of "internal" nodes along the rim of the defect. The number of such internal nodes is arbitrary, and is chosen in order to resolve the

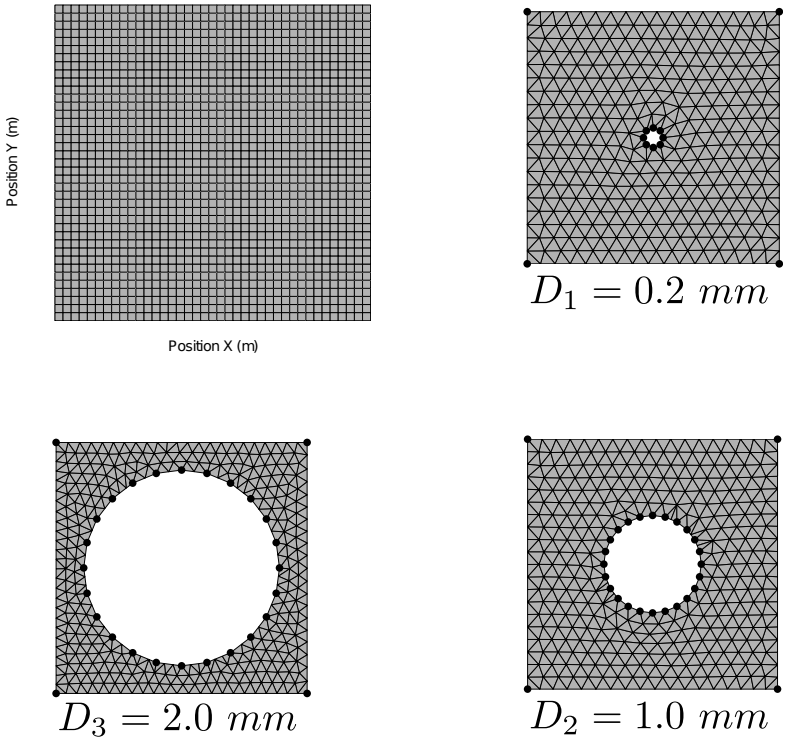

Figure 46: Discretization of the computational domain, and multiscale elements used to model three circular defects.

domain boundary. In addition, Fig. 46 shows the fine scale triangular mesh that is used inside each MSE to numerically compute the corresponding shape functions as described in Chapter II.

A reference FE discretization of the system, shown in Fig. 47, is comprised of an exterior region (Fig. 47.a) with regular (undistorted) elements, and a localized refinement region (Fig. 47.b,c,d) where the element size is gradually reduced to capture the fine-scale details. The presence of such refined elements clearly constitutes

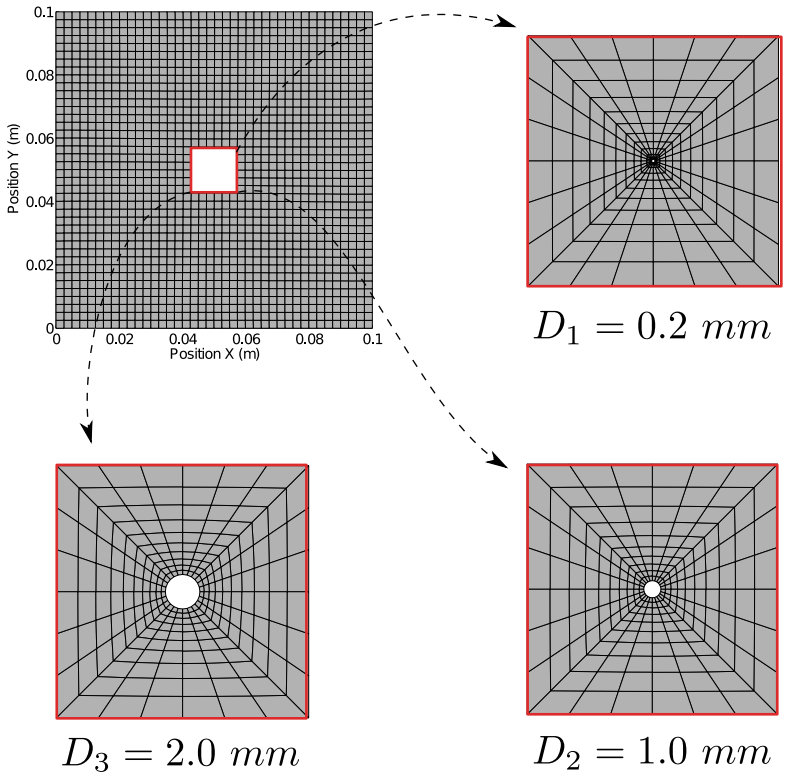

Figure 47: Finite element mesh of the computational domain with three refinement regions used to accommodate the presence of defects with different radius.

the primary disadvantage of FE techniques, since they increase the total number of DOFs explicitly retained in the simulation, and also impose a limit on the time step of integration. The generation of a good-quality mesh that provides a smooth transition between the uniform domain and the defect is also a time consuming operation that is completely bypassed in the proposed GMsFEM approach. In the following section, results of wave propagation computed with GMsFEM are compared with FE

simulations based on the discretizations described herein.

4.2.2 Numerical results

Numerical results are obtained when the system is excited by a concentrated nodal load in the lower portion of the domain (see Fig. 45.a) with a time variation corresponding to a 1-cycle tone burst centered at a frequency of 100 kHz. A first comparison between FEM and GMsFEM solutions is shown in Fig. 49 which illustrates the magnitude of displacements recorded at selected angular positions (see Fig. 48) along the rim of the three defects shown in Fig. 46. For the sake of clarity, only

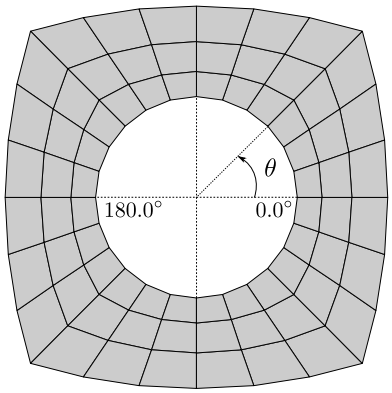

Figure 48: Angular positions along the rim of the hole.

four angles are considered but similar results are observed along the entire angular range. Such results indicate an excellent agreement between the two solutions for the entire simulation time, and show how the proposed GMsFEM correctly captures the wavefield near the three considered scatterers. A similar agreement is observed in Fig. 50 showing the total mechanical energy

$$\mathcal{E}(t) = \mathcal{T} + \mathcal{U} = \frac{1}{2}\dot{\boldsymbol{d}}^T \boldsymbol{M}\, \dot{\boldsymbol{d}} + \frac{1}{2}\boldsymbol{d}^T \boldsymbol{K}\, \boldsymbol{d} \tag{60}$$

evaluated within the refinement region of the FE model (see Fig. 47). Results are illustrated for the two extreme cases for which $D_1 = 0.2$ mm and $D_3 = 2.0$ mm, and show how GMsFEM captures the local softening of the structure as the defect

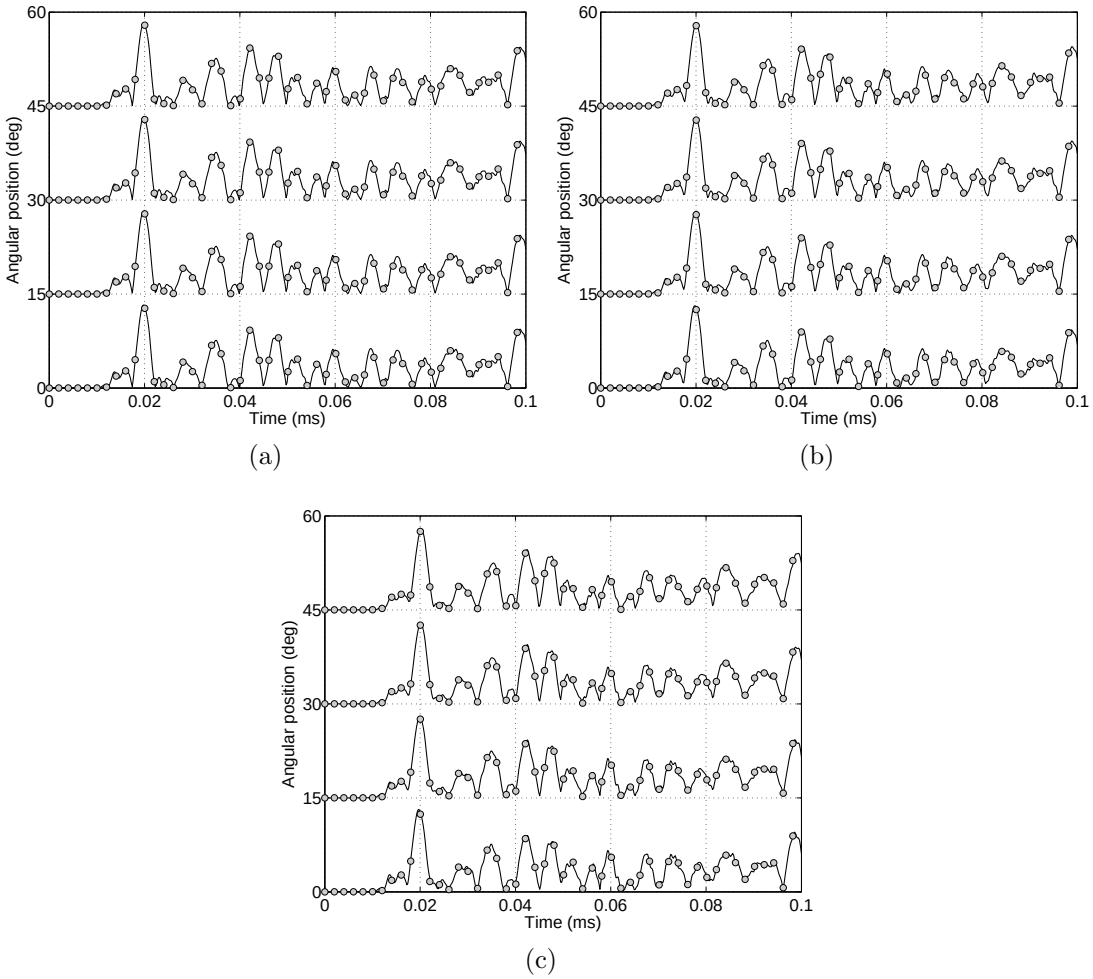

Figure 49: Magnitude of nodal displacements at selected angular positions along the perimeter of the hole: Diameter $D_1 = 0.2$ mm (a), $D_2 = 1.0$ mm (b), and $D_3 = 2.0$ mm (c). FEM results (solid line) and GMsFEM results (∘-markers).

size increases. Since $\mathcal{E}(t)$ is computed considering multiple elements, the agreement between FEM and GMsFEM results also confirms that the compatibility between MSEs and their adjacent elements is properly enforced.

Figure 51 shows similar results computed for the defect with $D_2 = 1.0$ mm. In this case the mechanical energy is computed only with GMsFEM by changing the size of the fine scale mesh used to compute the corresponding multiscale shape functions. For instance, a refined, intermediate, and coarse discretization within the MSE are considered featuring 1266, 320, and 82 fine-scale triangular elements, respectively.

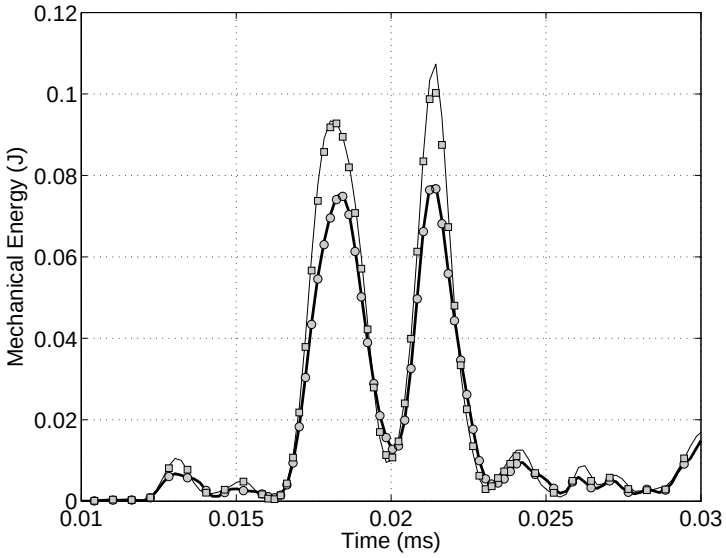

Figure 50: Mechanical energy computed within the refined region of the FE model for $D_1 = 0.2$ mm (thin solid line) and $D_3 = 2.0$ mm (thick solid line). Markers denote the same quantity computed with GMsFEM.

As shown in Fig. 51, little difference can be observed between results obtained with different local meshes, indicating the modest sensitivity of the solution with respect to the number of local elements.

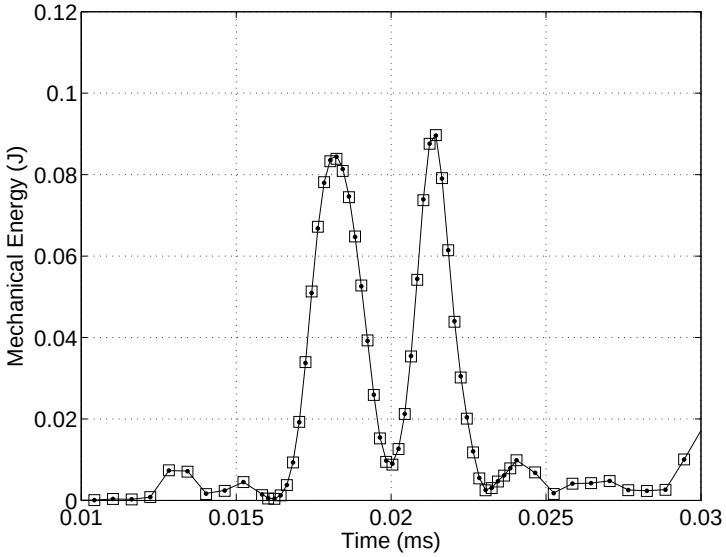

Figure 51: Mechanical energy computed for $D_2 = 1.0$ mm with GMsFEM using different fine scale grids: fine (solid line), intermediate (•-marker), and coarse (□-marker).

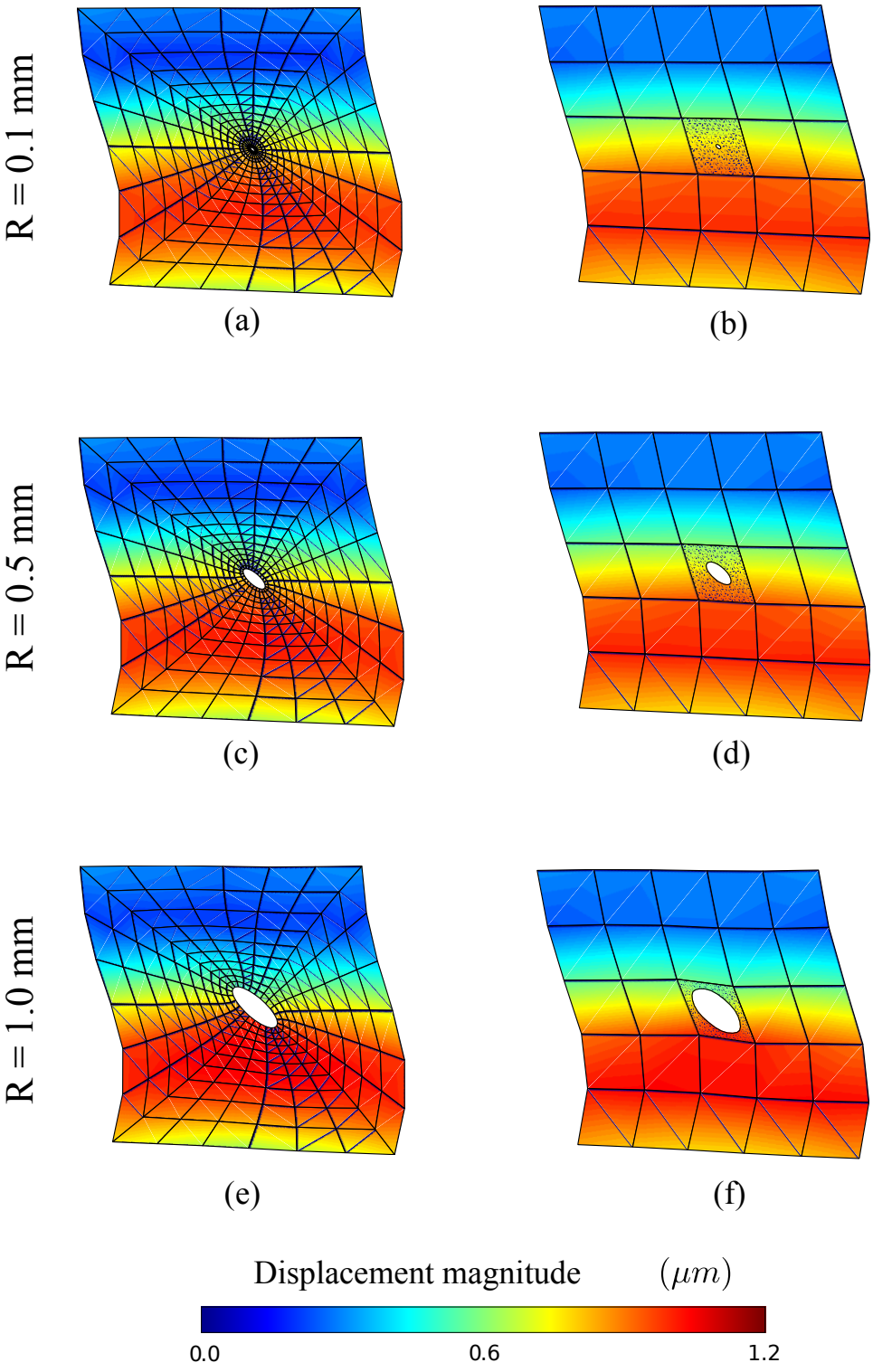

Figure 52: Deformation field in the refinement region around the hole after 20 μs: FEM results (a,c,e) and GMsFEM results (b,d,f).

A qualitative comparison between the FEM and GMsFEM solutions is shown in Fig. 52 that represents snapshots of the deformation field around the three defects. The solution on each multiscale element is projected onto the fine scale (triangular) mesh in order to facilitate its graphical visualization. Results indicate that both methods provide very similar results both in the exterior portion of the considered refinement region, and also in the interior region near the damage. From these results it is also possible to better appreciate the continuity of the solution across multiscale and adjacent quadrilateral elements.

4.3 Plate with surface crack

A damaged aluminum plate is modeled as a two-dimensional plane-strain domain and features a transverse crack emanating from the top surface, as shown in Fig. 53. Guided waves are generated at one end of the plate while a receiving sensor detects

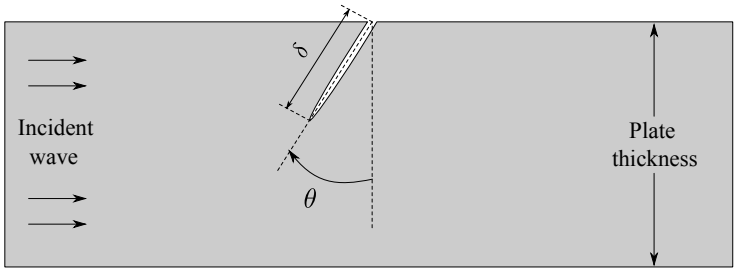

Figure 53: Schematic of a plate with an arbitrary-oriented crack.

the displacement at a point over the same side. Results are compared with a baseline configuration without damage so that changes in amplitude and phase of the received signal can be associated with the crack presence and extension. Simulations are repeated for different damage size and orientation in order to correlate the received signals with specific damage topologies. From a modeling standpoint this represents the major difficulty because each model requires a dedicated discretization that is often difficult to obtain using automatic mesh generation tools. In this section, different topologies are constructed with the proposed GMsFEM to conveniently model

the localized defect by means of a limited number of multiscale elements.

4.3.1 Multiscale model

As illustrated in Fig. 54, the considered aluminum plate features side length L=200 mm and thickness h=3 mm. The structure is excited by a uniform shear traction applied over a 2 mm long region near the left side of the plate. Resulting displacements are monitored by a virtual sensor located 25 mm away from the source (Fig. 54). The

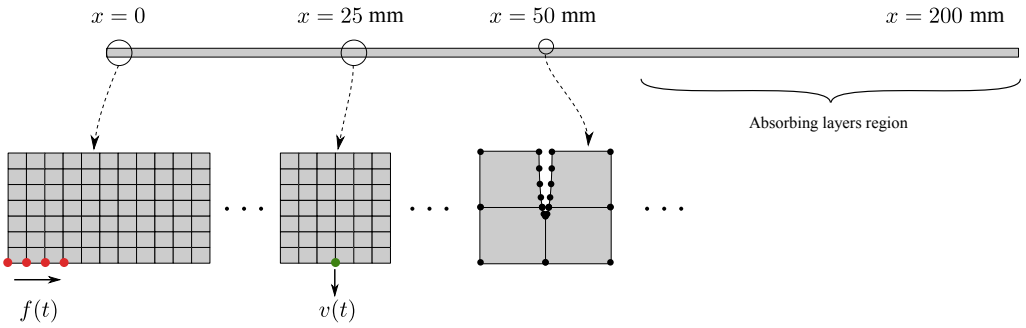

Figure 54: Multiscale model of the damaged plate.

input signal used to excite the system is a 4-cycle tone burst of center frequency of 200 kHz. The plate is discretized with 7 elements through the thickness, and 400 plane-strain elements along the plate's length. The presence of a transverse crack is modeled by means of a few number of multiscale elements in the vicinity of the small imperfection, while the remaining part of the computational grid is left undistorted, as shown in Fig. 54. The crack is represented as an elliptical inclusion with semi-minor axis equal to 0.05 mm, and parametrized in terms of the semi-major axis (δ) representing the defect depth, and the orientation (θ) with respect to the thickness direction (Fig. 53). For selected configurations, the problem is discretized by means of a reference FE mesh that uses the same discretization in the portion of the domain away from the crack, while a localized refinement region describes the defect's geometry.

4.3.2 Results

Numerical results are first presented when a $\delta = 1.0$ mm long crack is perpendicular to the plate's surface (i.e. $\theta = 0°$). Figure 57 shows selected snapshots of the wavefield which illustrate the interaction of the incident wave with the defect. The reflections

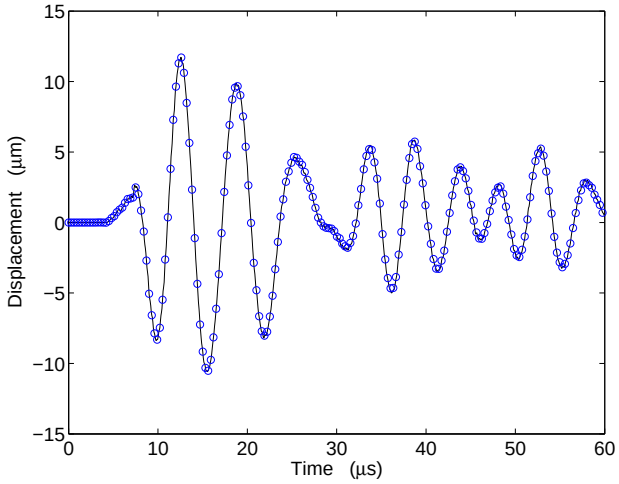

(a)

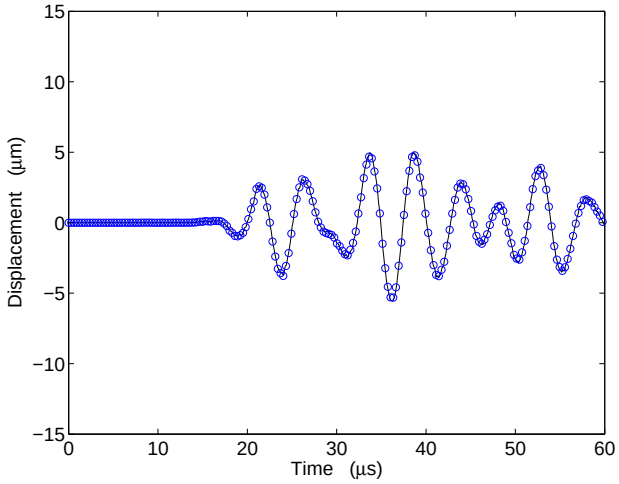

(b)

Figure 55: Comparison between the displacement u_x (a) and associated reflected signal (b) computed with GMsFEM (o-markers) and FEM (solid line) for a vertical crack of depth $\delta = 1.0$ mm.

are observed in the time histories of the longitudinal (u_x) and transverse (u_y) displacements recorded by the sensor, as illustrated in Figs. 55.a, and 56.a, respectively, and uniquely characterize the size and location of the defect. In order to retain only

such relevant information, the baseline signal is subtracted to the measured response, so that the time of arrival and the maximum amplitude of reflected waves can be easily identified as shown in Figs. 55.b, and 56.b. Also, results are presented in a

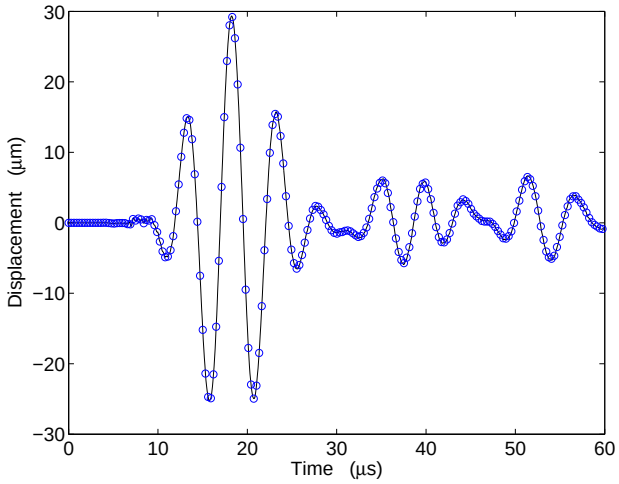

(a)

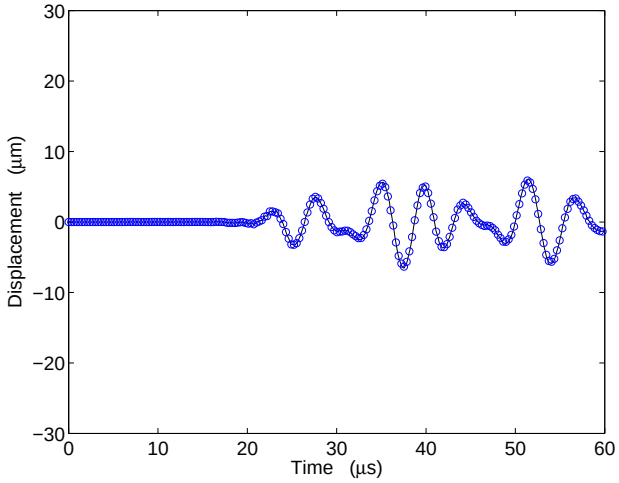

(b)

Figure 56: Comparison between the displacement u_y (a) and associated reflected signal (b) computed with GMsFEM (o-markers) and FEM (solid line) for a vertical crack of depth $\delta = 1.0$ mm.

comparative way in order to highlight the excellent agreement between GMsFEM and FEM solutions, showing how both methods correctly capture the wave pattern resulting from multiple reflections of the input signal with the stress-free surfaces of the panel and, at a smaller scale, with damage.

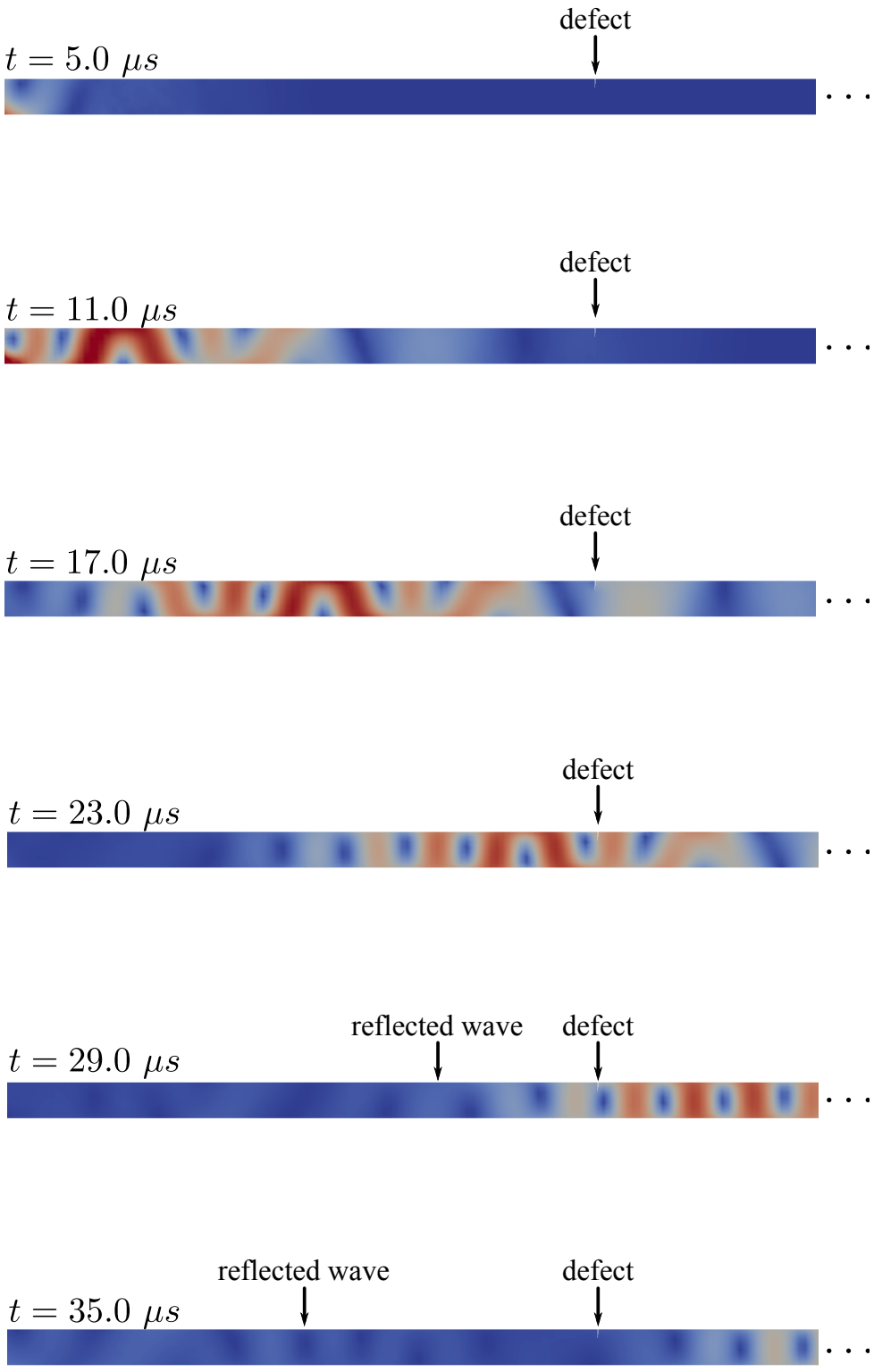

Figure 57: Displacement field computed for a vertical crack of depth $\delta = 1.0$ mm.

A measure of the scattered wavefield is provided by the reflection coefficient defined as:

$$\boldsymbol{\mathcal{R}} = [\mathcal{R}_x \quad \mathcal{R}_y]^T = \frac{\boldsymbol{u}^{ref}}{u^{inc}_{max}} \cdot 100 \tag{61}$$

where $\boldsymbol{u}^{ref} = [u_{x,\,max} \quad u_{y,\,max}]^{ref}$ is the maximum amplitude of the reflected signal, and u^{inc}_{max} is the amplitude of the incident wave. Such coefficient is presented in Fig. 58 as a function of the crack depth (δ) expressed as a percentage of the plate thickness. The computed results illustrate the increase of the reflection index with the

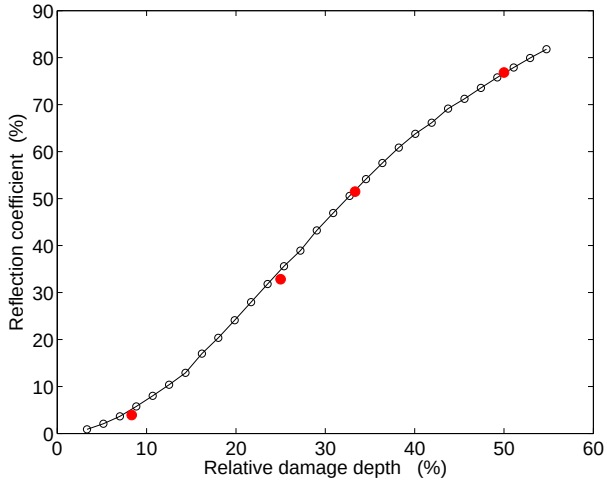

(a)

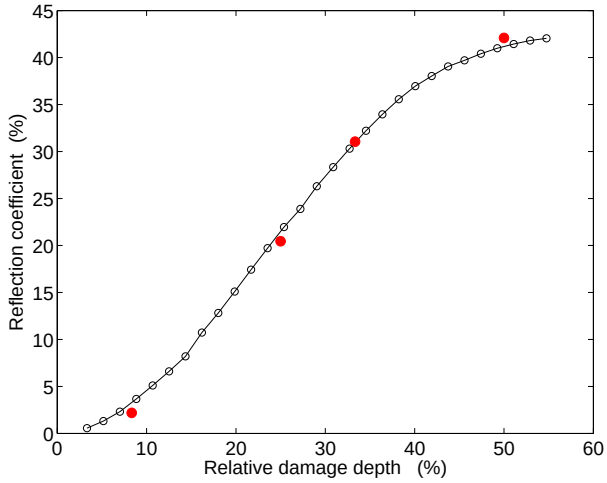

(b)

Figure 58: Reflection coefficients associated with u_x (a) and u_y (b) corresponding to a vertical defect of increasing depth (relative to plate thickness). The solid (red) markers denote FEM solutions computed for comparison purposes.

crack depth, and show the excellent agreement with the coefficients computed with selected FE meshes. Also, each point in Fig 58 is the result of a transient simulation involving a different geometry generated with the proposed multiscale elements. This operation, seamlessly accomplished by GMsFEM, is a challenging task when using standard FE packages due to the amount of work generally required to regenerate each model and remesh it. The proposed modeling tool allows to easily extend such results

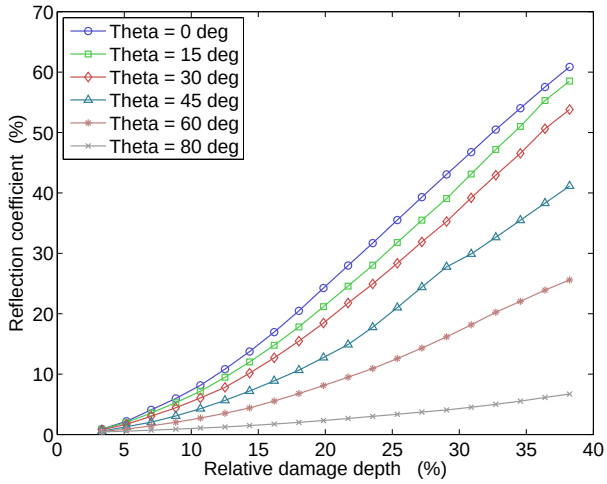

(a)

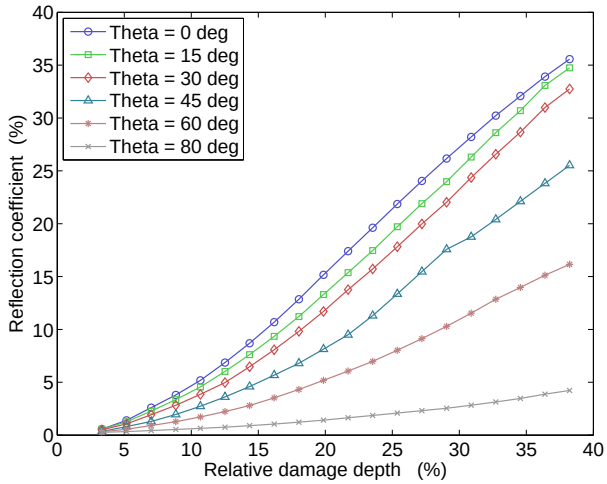

(b)

Figure 59: Reflection coefficients associated with u_x (a) and u_y (b) computed for different values of the orientation angle θ.

for arbitrarily oriented cracks. For instance, reflection coefficients associated with the two components of the wavefield (u_x) and (u_y) are illustrated in Fig. 59 showing the

gradual attenuation of reflected waves for increasing values of the orientation angle θ.

4.4 Scattering analysis from two-dimensional defects

In this section the proposed GMsFEM is applied to the scattering problem of incident waves from defects in a two-dimensional aluminum plate. Scattering diagrams are of particular interest for SHM and NDE applications since they contain a wealth of information about size, location, and relative orientation of damage with respect to the source point.

4.4.1 Configuration and multiscale finite element model

The computational domain consists of a square plate made of aluminum (E=71 GPa, ρ=2700 kg/m^3, and ν=0.3) with side length L=120 mm and a uniform thickness in plane stress. An elliptic void is located at the center of the considered domain. The

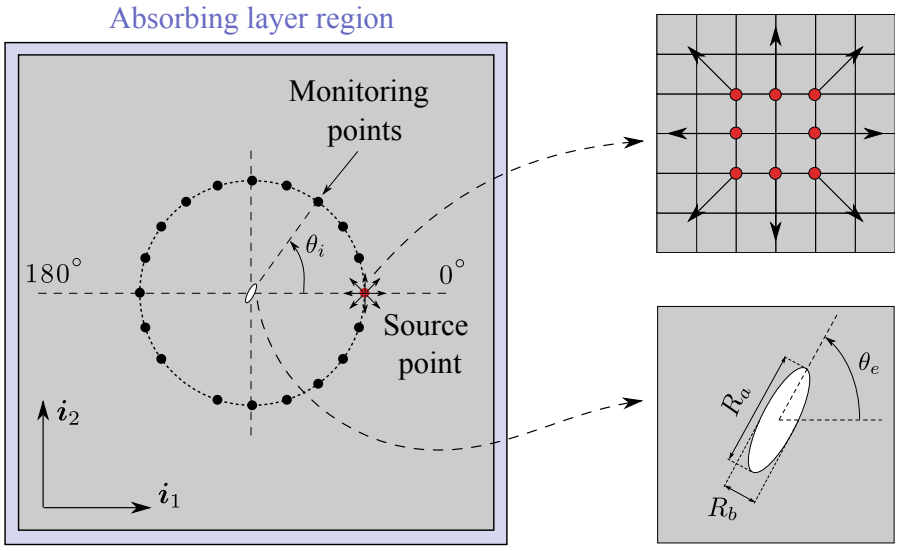

Figure 60: Schematic of the plate configuration considered for scattering analysis.

damage geometry is defined in terms of the ellipse's axes R_a, R_b, and the orientation angle θ_e. The structure is excited by a narrowband tone burst signal with central frequency of 300 kHz. In order to simulate the wavefield generated by a surface acoustic transducer, the 8-node point-like source configuration illustrated in Fig. 60

is adopted in the model. The defect is surrounded by a circular array of $N_t = 50$ transducers uniformly distributed along a circumference of radius $r_i = 24$ mm ($i = 1 \dots N_t$) (Fig. 60). Each transducer records the time history of the displacement that is then used to generate a directivity map of the scattered wavefield as a function of the angle θ_i, as discussed in the following section.

The computational domain is discretized using a regular grid of 200×200 plane stress elements with unit aspect ratio and a minimum of 15 nodes per wavelength. As shown in Fig. 61.a the output displacement is measured at selected nodes that most closely approximate the theoretical radial location. In this way, the maximum error induced by a sensor misalignment is of the order of the element side and is negligible for the purpose of the present analysis. The presence of defects at the center of the

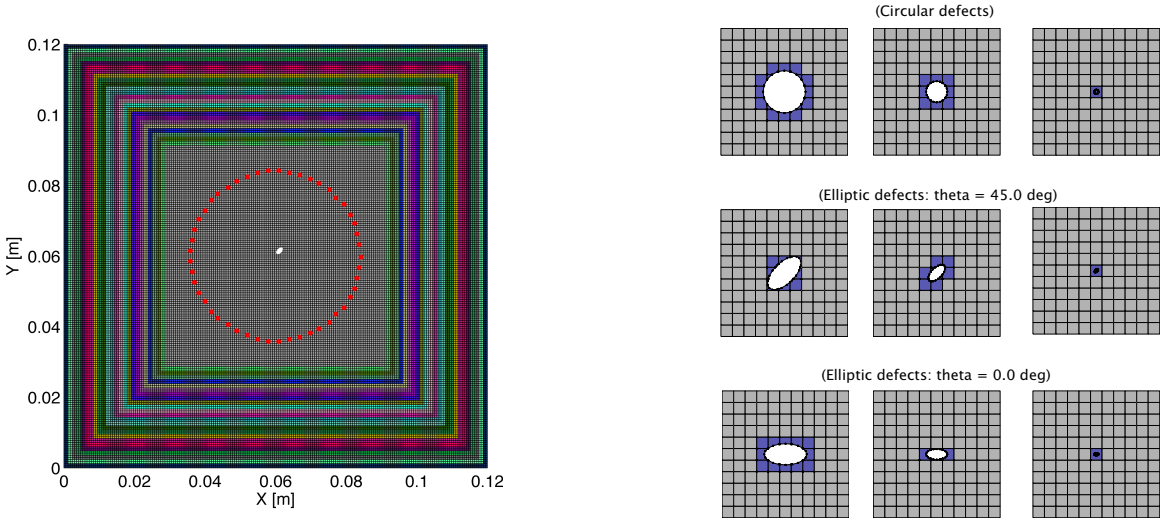

Figure 61: Multiscale FE mesh with absorbing layers and sensor location (a) and detail of the damage modeled using multiscale elements (b).

plate is modeled through a proper number of multiscale elements. Figure 61.b shows how the original uniform mesh is "*trimmed*" along the contour of the inclusion and additional nodes are added to the model to represent the new structural boundary. Since the considered multiscale elements are intrinsically compatible with adjacent

quadrilateral elements, the present approach does not alter the remaining portion of the FE discretization therefore minimizing mesh distortion, regardless of the size and shape of the inclusion.

For the calculation of the scattering coefficients it is necessary to eliminate, or at least reduce, wave reflections from the computational domain boundaries. A series of 25 damping layers (see Fig. 61.a,), with two elements per layer, are used along the external edges of the FE mesh to dampen the incoming and reflected waves. Within each layer a stiffness-proportional damping model is employed with damping values gradually increasing from the center to the outer regions of the model. The total number of damping layers and the maximum damping coefficient ($\beta_{max} = 4.0\,10^{-7}$) are chosen by a trial and error approach in order to reduce the amplitude of reflected waves of at least one order of magnitude with respect to the amplitude of the incoming signal.

4.4.2 Calculation of the scattering coefficients

The scattering coefficients are estimated from the information recorded by the sensors shown in Fig. 60. For instance, the displacement measured at the i^{th} sensor is $\boldsymbol{u}_i = \boldsymbol{u}(\theta_i) = [u_x,\ u_y]_i^T$ where u_x and u_y denote the components of the displacement vector resolved in the cartesian reference frame $(\boldsymbol{i}_1,\ \boldsymbol{i}_2)$ shown in Fig. 60, and the angle θ_i denotes the angular position of the i^{th} sensor. A differential displacement $\boldsymbol{u}_i^d = \boldsymbol{u}^d(\theta_i)$ is defined as:

$$\boldsymbol{u}_i^d = [u_x^d,\ u_y^d]_i^T = \boldsymbol{u}_i^{ref} - \boldsymbol{u}_i \qquad (i = 1, \ldots, N_t) \tag{62}$$

where $\boldsymbol{u}_i^{ref} = [u_x^{ref},\ u_y^{ref}]_i^T$ is the baseline (undamaged) signal at the i^{th} transducer. Due to the symmetry of the problem, the components of $\boldsymbol{u}_i^d$ are conveniently described in polar coordinates as:

$$\widehat{\boldsymbol{u}}_i^d = \boldsymbol{R}_i\ \boldsymbol{u}_i^d = [\widehat{u}_r^d \quad \widehat{u}_\theta^d]_i \tag{63}$$

where

$$\boldsymbol{R}_i = \begin{bmatrix} \cos\theta_i & \sin\theta_i \\ -\sin\theta_i & \cos\theta_i \end{bmatrix} \tag{64}$$

As described in [39], two scattering coefficients, one for each component of $\widehat{\boldsymbol{u}}_i^d$, can be defined as:

$$S_{P,i} = S_P(\theta_i) = \frac{\mathcal{H}[\widehat{u}_{r,i}^d(t_{H_{max}})]}{\mathcal{H}[\widehat{u}_{r,i}^{ref}(t_{H_{max}})]}$$

$$S_{S,i} = S_S(\theta_i) = \frac{\mathcal{H}[\widehat{u}_{\theta,i}^d(t_{H_{max}})]}{\mathcal{H}[\widehat{u}_{\theta,i}^{ref}(t_{H_{max}})]} \tag{65}$$

where

$$\mathcal{H}[f(t)] = \sqrt{f(t)^2 + F_{\mathcal{H}}(t)^2} \quad \text{and} \quad F_{\mathcal{H}}(t) = \frac{1}{\pi}\int_{-\infty}^{+\infty} \frac{f(s)}{s-t}\, ds \tag{66}$$

is the Hilbert transform of the real signal $f(t)$. Also, in Eq. (65), $t_{\mathcal{H}_{max}}$ denotes the time at which the Hilbert envelope is maximum, as schematically shown in Fig. 62. The scattering coefficients defined in Eq. (65) are computed at each angular location θ_i to illustrate the directivity of the wavefield scattered by the defect. Specifically,

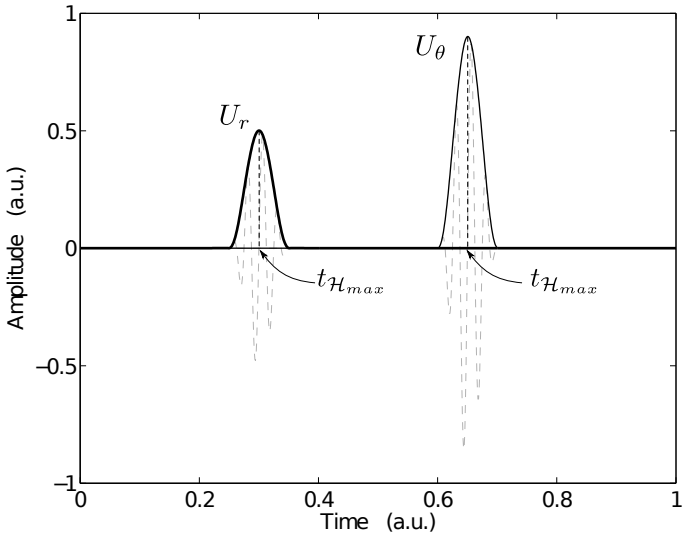

Figure 62: Example of the Hilbert envelope $\mathcal{H}[u(t)]$ of the radial (thick line) and tangential (thin line) components of the displacement field.

the coefficient S_P is computed using the radial component (u_r) of the scattered field

that represents the dominant displacement characterizing the scattered pressure (P) waves. Similarly, S_S is computed using the hoop displacements (u_θ), and therefore is associated to the scattered shear (S) waves.

4.4.3 Numerical results for elliptic inclusions

Numerical simulations are conducted for a series of configurations limited to significant variations of the damage parameters summarized in Table 3. The response of the undamaged structure is also computed to provide a baseline that is used to extract the scattering information from the incident wavefield. Note that at the given

Table 3: Summary of the considered damage configurations.

	Defect size I		Defect size II		Defect size III	
Label	R_a (mm)	R_b (mm)	R_a (mm)	R_b (mm)	R_a (mm)	R_b (mm)
A ($\theta_e = 0°$)	1.0	1.0	0.5	0.5	0.1	0.1
B ($\theta_e = 0°$)	1.0	0.5	0.5	0.25	0.1	0.05
C ($\theta_e = 45°$)	1.0	0.5	0.5	0.25	0.1	0.05
D ($\theta_e = 90°$)	1.0	0.5	0.5	0.25	0.1	0.05

excitation frequency (300 kHz) the wavelengths of the incident P- and S-waves are $\lambda_P = 18.2$ mm, and $\lambda_S = 10.2$ mm respectively. Such values are approximately one to two orders of magnitude smaller than the defect's sizes considered in this study (see Table 3), that define the multiscale nature of the problem.

The computed scattering coefficients are shown in Figs. 63 - 66 in terms of polar plots representing the amplitude of the reflected signal as a function of the angular coordinate θ. Such diagrams assume that the incident wave propagate along the $0° \rightarrow 180°$ direction (see Fig. 60). The results reveal that (reflected) P-waves tend to propagate along the $0° - 180°$ direction for defects A, B, and D, while when the crack elongates at 45° with respect to the incidence direction, waves are mostly scattered

perpendicular to the major defect side. Similar results, computed for S-waves, highlight a scattering pattern mostly focused along the $\pm 45^{\circ}$ with the exception of defect C characterized by S_S scattering diagrams that are rotated to reflect the different symmetry of the problem. Also, Figs. 63, 64, and 66, corresponding, respectively, to defects A, B, and D, feature scattering diagrams that preserve the symmetry of the problem. When the elliptic damage forms an angle with the direction of incoming wave (see Fig. 65), both P- and S-waves are scattered mainly along directions perpendicular to the principal axis of the inclusion. Results also reveal that the magnitude of the scattered field decreases almost quadratically as the damage size reduces, while the overall directionality pattern remains qualitatively the same. It is finally worth mentioning that all the present scattering data are computed without remeshing the entire computational domain. Instead, only the elements around the defect are updated to accommodate the different inclusions as illustrated in Fig. 61.b.

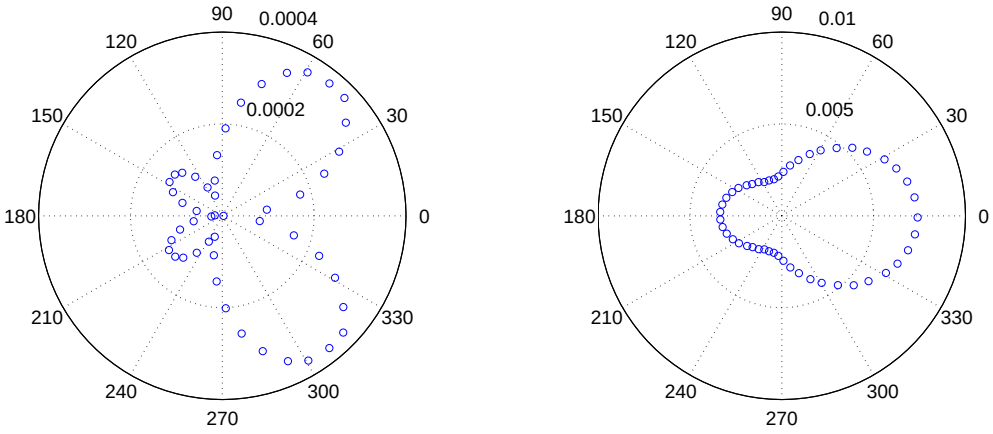

(a) S_S ($R_a = 0.1$ mm) (b) S_P ($R_a = 0.1$ mm)

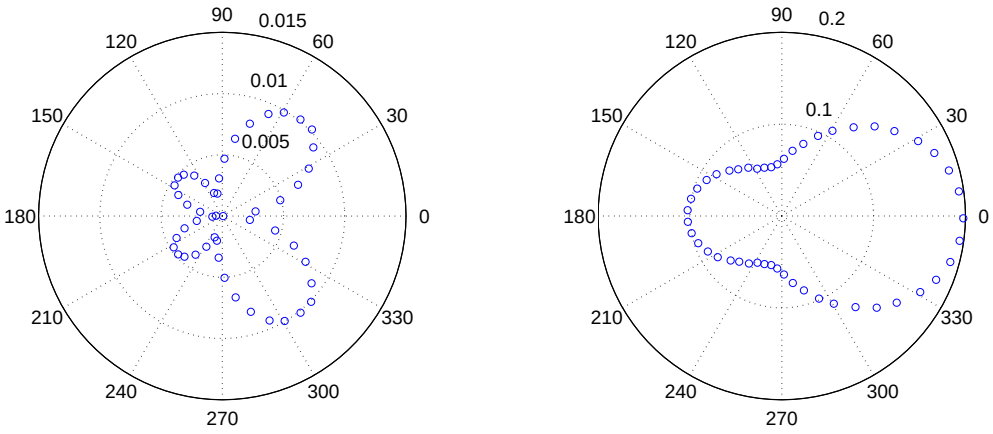

(c) S_S ($R_a = 0.5$ mm) (d) S_P ($R_a = 0.5$ mm)

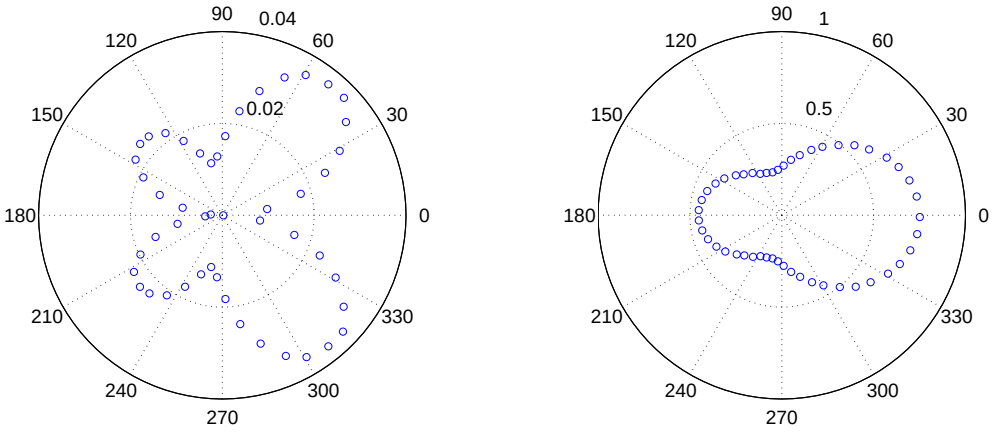

(e) S_S ($R_a = 1.0$ mm) (f) S_P ($R_a = 1.0$ mm)

Figure 63: Scattering plots from circular defects: $R_a = 0.1$ mm (a,b), $R_a = 0.5$ mm (c,d), and $R_a = 1.0$ mm (e,f).

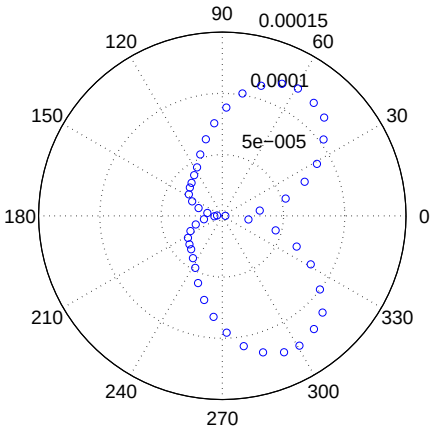

(a) S_S ($R_a = 0.1$ mm)

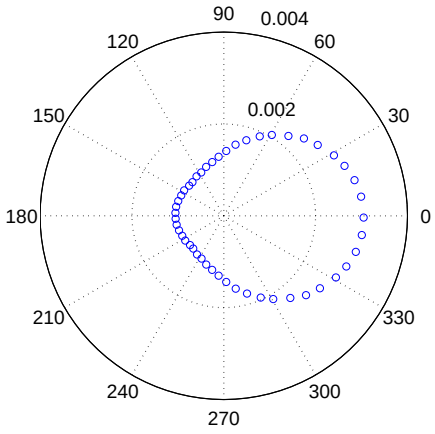

(b) S_P ($R_a = 0.1$ mm)

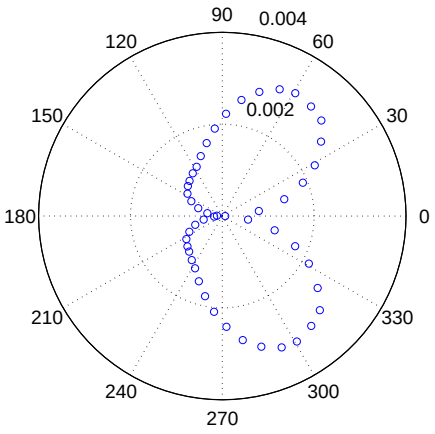

(c) S_S ($R_a = 0.5$ mm)

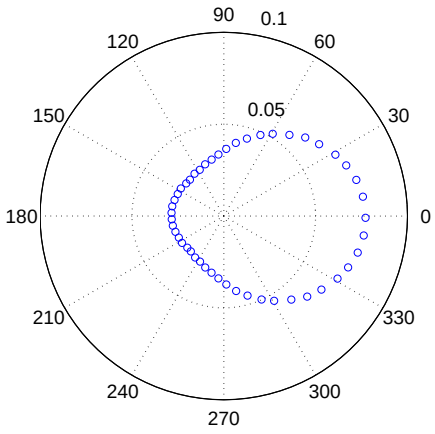

(d) S_P ($R_a = 0.5$ mm)

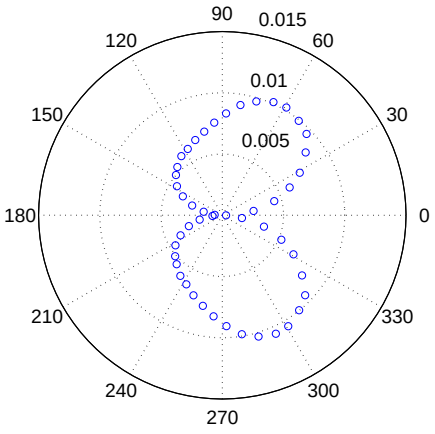

(e) S_S ($R_a = 1.0$ mm)

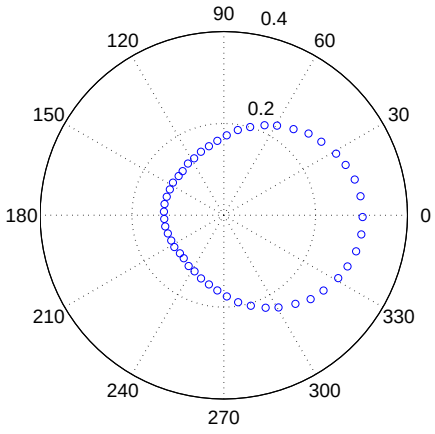

(f) S_P ($R_a = 1.0$ mm)

Figure 64: Scattering plots from elliptic defects with $\theta_e = 0°$: $R_a = 0.1$ mm (a,b), $R_a = 0.5$ mm (c,d), and $R_a = 1.0$ mm (e,f).

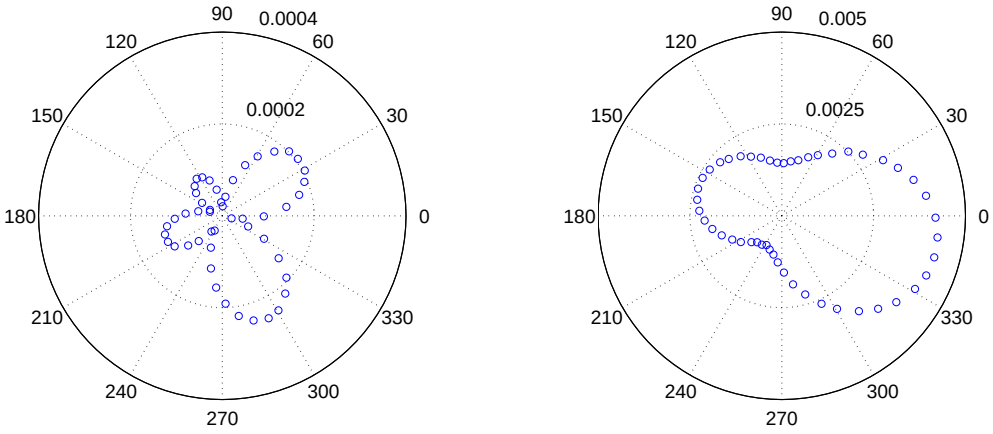

(a) S_S ($R_a = 0.1$ mm) (b) S_P ($R_a = 0.1$ mm)

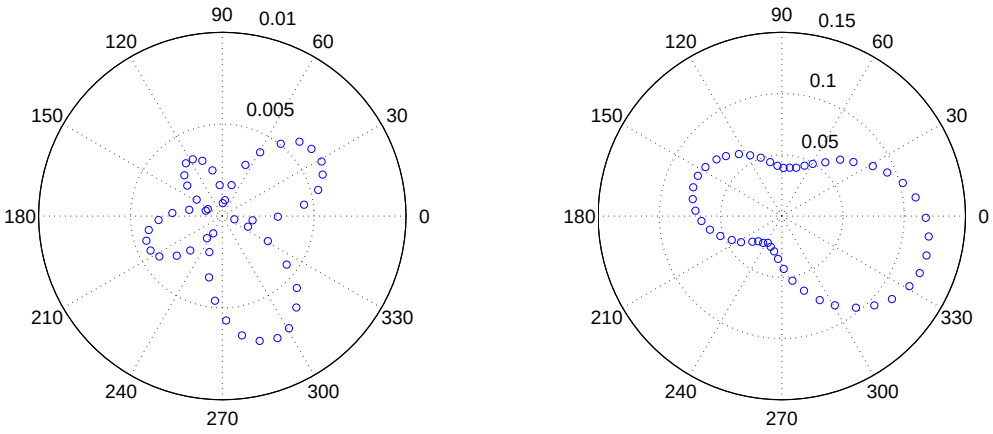

(c) S_S ($R_a = 0.5$ mm) (d) S_P ($R_a = 0.5$ mm)

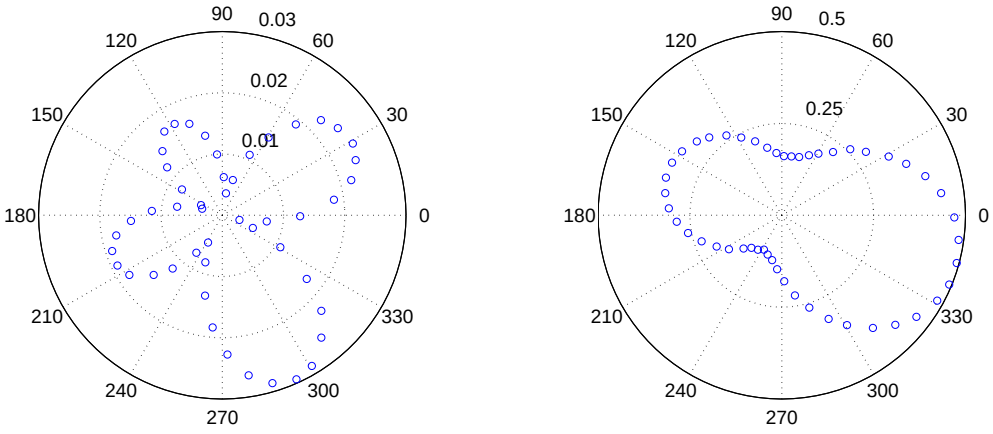

(e) S_S ($R_a = 1.0$ mm) (f) S_P ($R_a = 1.0$ mm)

Figure 65: Scattering plots from elliptic defects with $\theta_e = 45°$: $R_a = 0.1$ mm (a,b), $R_a = 0.5$ mm (c,d), and $R_a = 1.0$ mm (e,f).

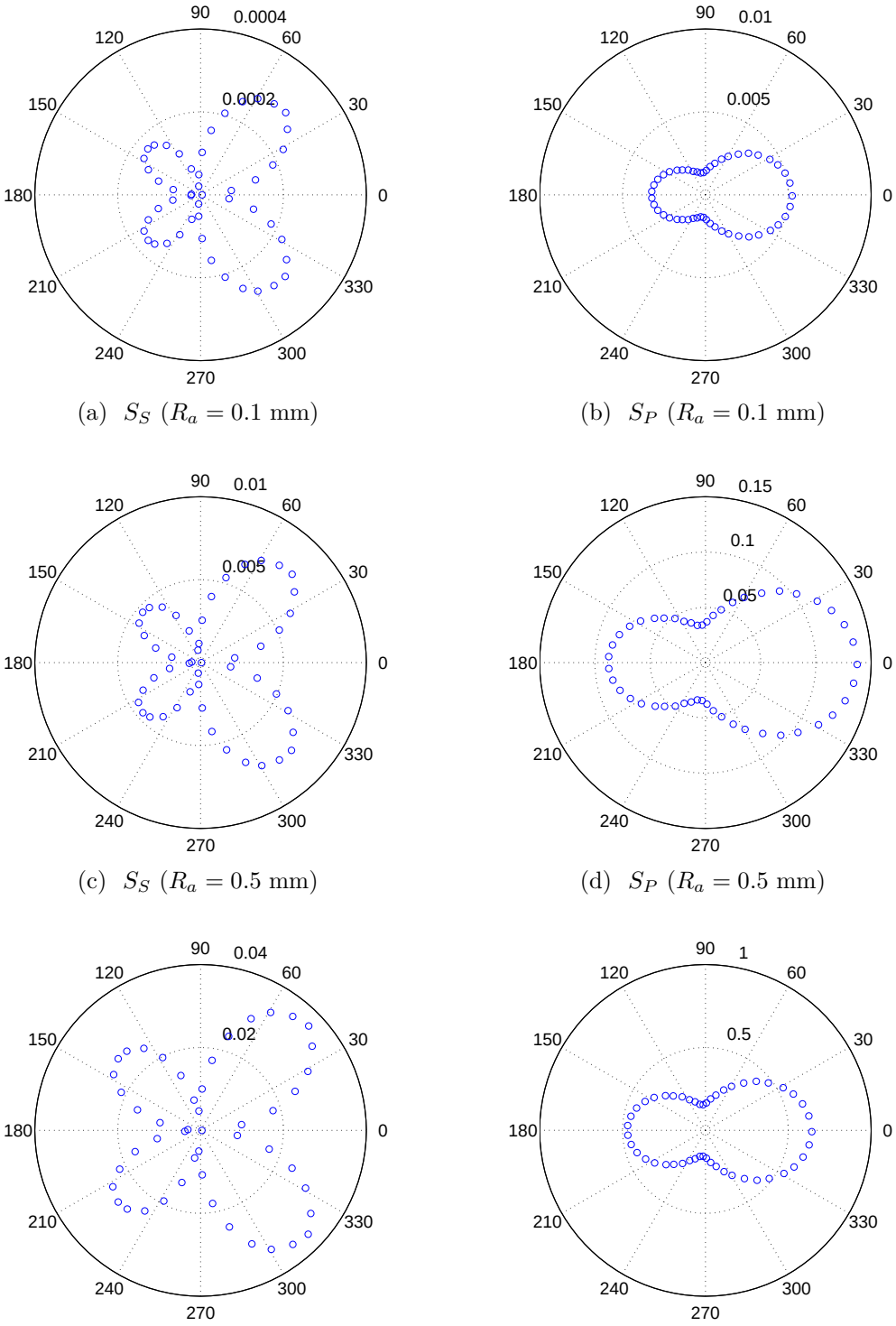

(a) S_S ($R_a = 0.1$ mm) (b) S_P ($R_a = 0.1$ mm)

(c) S_S ($R_a = 0.5$ mm) (d) S_P ($R_a = 0.5$ mm)

(e) S_S ($R_a = 1.0$ mm) (f) S_P ($R_a = 1.0$ mm)

Figure 66: Scattering plots from elliptic defects with $\theta_e = 90°$: $R_a = 0.1$ mm (a,b), $R_a = 0.5$ mm (c,d), and $R_a = 1.0$ mm (e,f).

4.5 Scattering from three-dimensional defects

In this section, the GMsFEM is exploited to study the scattering patterns of three-dimensional (3D) defects. A three-dimensional discretization is used to represent the propagation of all the fundamental antisymmetric (A_0), shear-horizontal (SH_0), and symmetric (S_0) Lamb wave modes that are not satisfactory approximated by means of two-dimensional plane-stress or plane-strain models. Furthermore a 3D model allows to represent part-depth defects and to investigate mode conversions occurring when either S_0, or A_0 incident waves are considered.

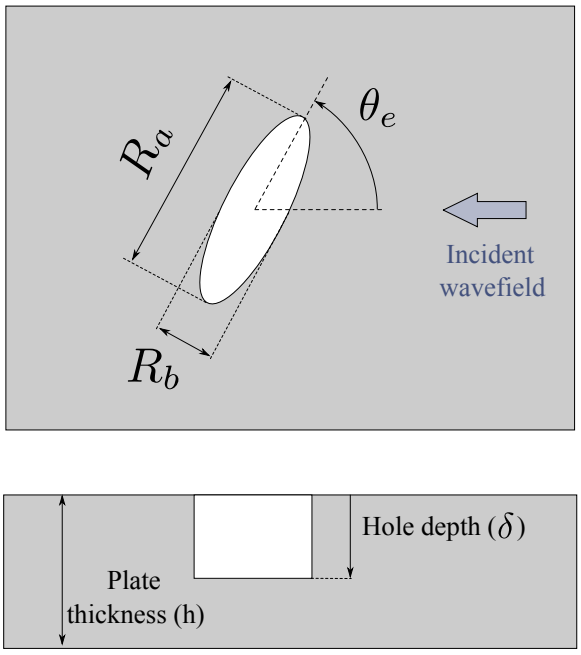

Figure 67: Schematic of the three-dimensional defect configuration.

The present study focuses on the analysis of part-depth elliptic defects in order to highlight the effects of different damage parameters on the scattering coefficients introduced in the previous section. Such information is essential for the development of reliable detection algorithms based, for example, on adaptive imaging techniques [91]. Analysis are conducted considering a 3 mm thick square aluminum plate ($L = 130$ mm) hosting a defect located at its center that partially extends through the plate's thickness, as shown in Fig. 67.

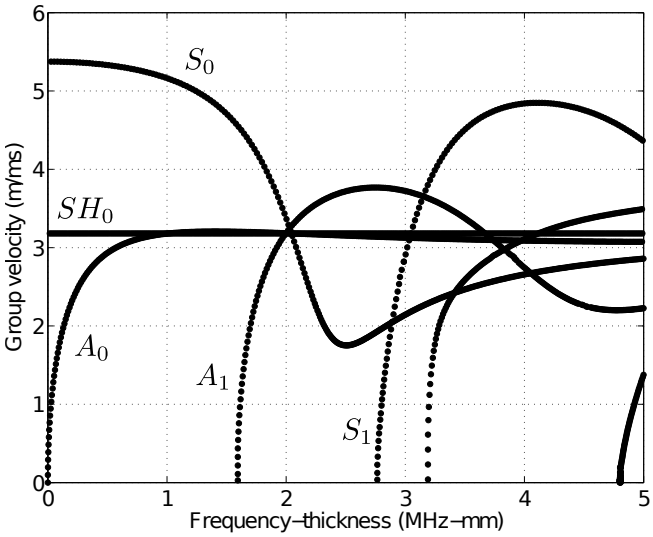

(a) Global view

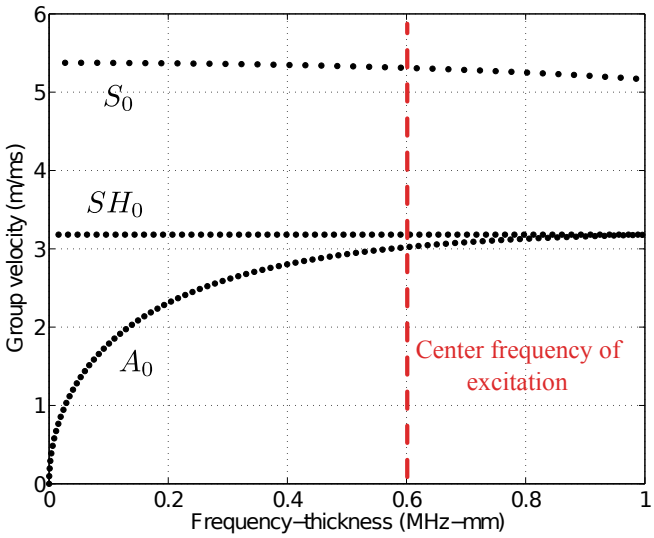

(b) Detail view

Figure 68: Group velocity curves for Lamb waves in an aluminum plate.

Both incident S_0 and A_0 waves are considered in this study. The former are commonly exploited for their relatively high group velocity and low dispersion that are particularly attractive for long range propagation SHM applications. Also, A_0 incoming waves are used for their higher sensitivity to partial-thickness and delamination type defects [81]. As shown in Fig. 68, the non-dispersive properties of S_0 waves tend to be more pronounced at low frequencies, while the A_0 mode is characterized by constant group velocity at higher frequencies. Increasing the frequency of

excitation may also increase the sensitivity to defects [82], with an upper limit given by the A_1 cut-off frequency of about 1.6 MHz-mm. For such reasons a compromise is in general required when choosing the frequency of excitation. In this work the plate is excited by a 5-cycle tone burst signal with center frequency of 600 kHz-mm, where both S_0 and A_0 modes are reasonably non-dispersive. At this frequency, the fundamental Lamb modes are characterized by wavelengths $\lambda_{A_0} = 10.0$ mm, $\lambda_{SH_0} = 15.9$ mm, and $\lambda_{S_0} = 26.8$ mm respectively, while the considered defects size ranges between 0.1 mm to 1.5 mm. The analysis of such small imperfections is of extreme importance to understand the structural behavior at the onset of damage but at the same time represents a critical modeling scenario since the element size is dictated by the small geometrical features of the defect rather than the shortest (A_0) wavelength.

4.5.1 Model description and validation of results

The adopted three-dimensional finite element model is illustrated in Fig. 69. The

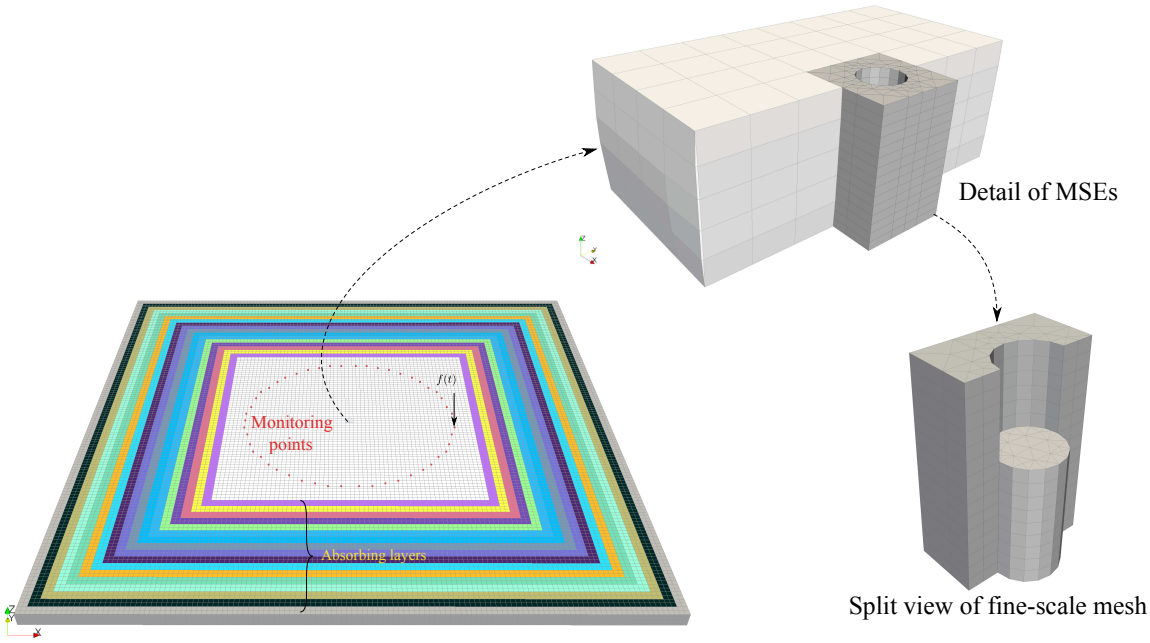

Figure 69: Numerical model of the 3D plate, and detail of the mesh around the defect.

proposed multiscale method allows using a relatively coarse numerical grid capable of

capturing the global wave motion in the homogeneous portion of the domain, while the presence of defects is modeled by means of a limited number of 3D multiscale elements. Specifically, the computational domain is discretized by means of 130×130×5 linear HEXA elements in order to largely satisfy the following condition:

$$\lambda_{min} > 7 \ \max\{\Delta x\} \tag{67}$$

where λ_{min} represents the shortest wavelength within the bandwidth of the signals, and $\max\{\Delta x\}$ is the largest element dimensions of the model. This criterion has been proposed by several authors [10, 116], and also confirmed by our own experience, to be effective for ensuring accurate prediction of the dispersion properties. Also, the number of elements through the thickness of the plate ensures an aspect ratio $\mathcal{AR} = \max\{\Delta x\}/\min\{\Delta x\} = 1.67$ that allows capturing the dispersion properties of the plate as suggested by [33]. Multiscale elements are used in the central portion of the domain to model the presence of irregular defects. As shown in Fig. 70, each multiscale element extends through the entire thickness of the plate because it is not possible, within the present framework, to impose inter-element compatibility between MSEs with non-quadrilateral interfaces (see Section 2.3.3). Also, Fig. 70 shows that within

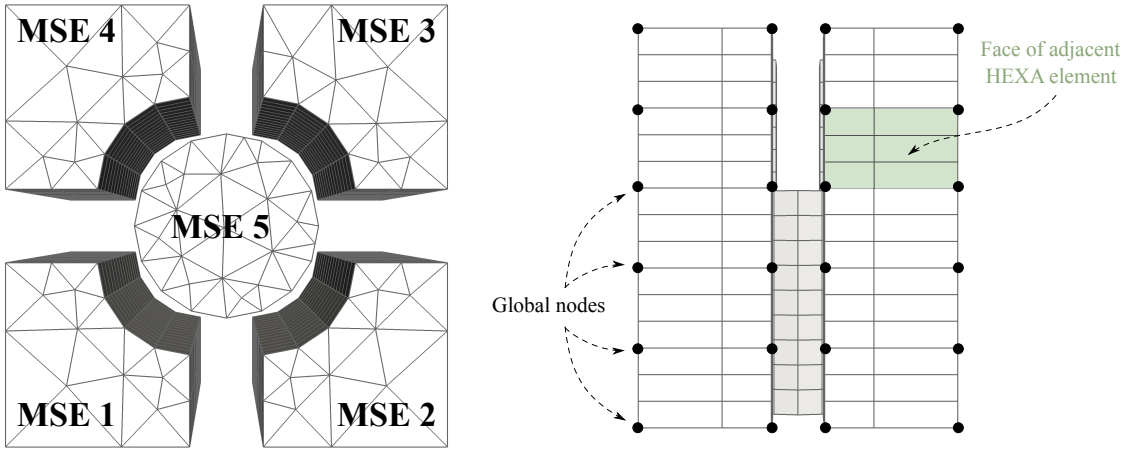

(a) Top view (b) Side view

Figure 70: Multiscale elements used to model a circular part-thickness hole with radius $R = 0.5$ mm.

each MSE a tetrahedral fine-scale mesh is adopted to exploit the modeling flexibility of triangular elements over the plate's surface while exactly satisfying displacement compatibility over the side faces adjacent to the neighboring HEXA elements (see Fig. 70.b).

In order to compute the scattering diagrams due to incident S_0 waves, the 8-node point-like source strategy presented in the previous section (Fig. 60) is adopted also for the 3D plate model considered herein. The only difference resides in the fact that in this case all the nodes through the thickness of the plate are uniformly excited as shown in Fig. 71.a to generate a perfectly symmetric loading condition. The effectiveness of such approach is verified by comparing the 3D Fourier Transform (FT) of the displacements recorded over one surface of the plate, with the prediction computed by the Semi Analytical Finite Element Method (SAFE) [1]. Details on the signal processing techniques adopted for the calculation of the 3D FT can be found in [92, 111]. The excellent overlap between the contour lines and the semi-analytical

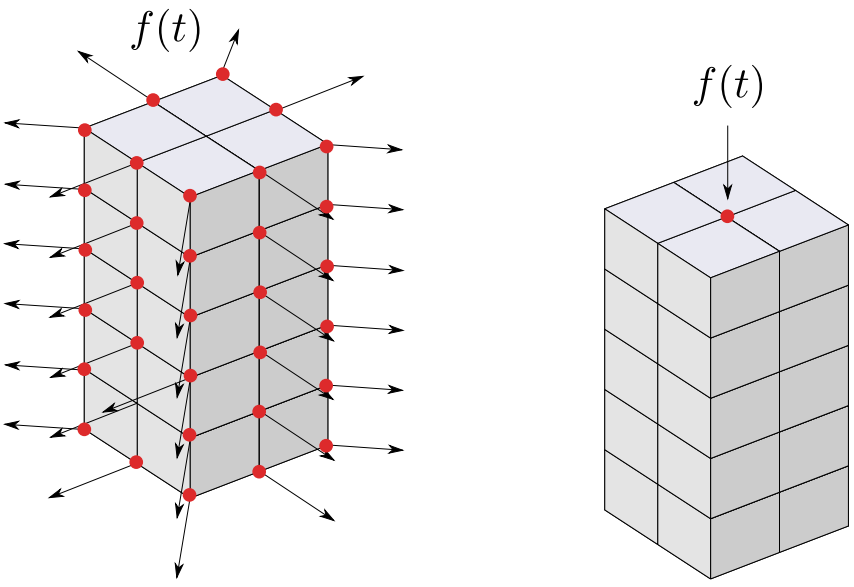

(a) In-plane (b) Out-of-plane

Figure 71: Three-dimensional point-like sources for S_0 (a) and A_0 (b) wave mode generation.

predictions of the S_0 mode are observed in Fig. 72 which illustrates how the adopted

excitation strategy is effectively capable of selecting the desired wave mode. Similar considerations hold when A_0 waves are generated. In this case a single out-of-plane force is applied at the desired node belonging to the top plate surface as shown in Fig. 71.b. This approach is simple and reliable for A_0 mode generation as confirmed by the comparative frequency/wavenumber analysis presented in Fig. 73.

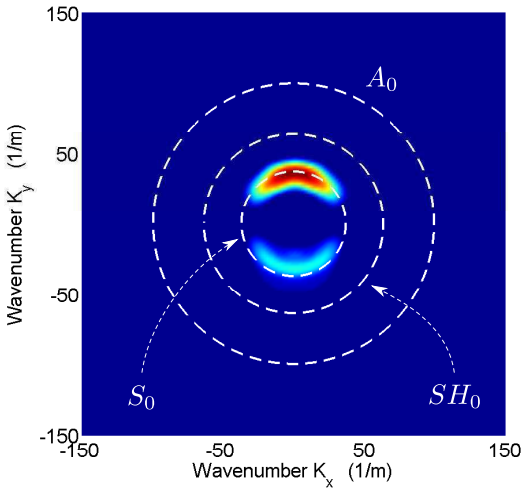

(a) Displacement U_x

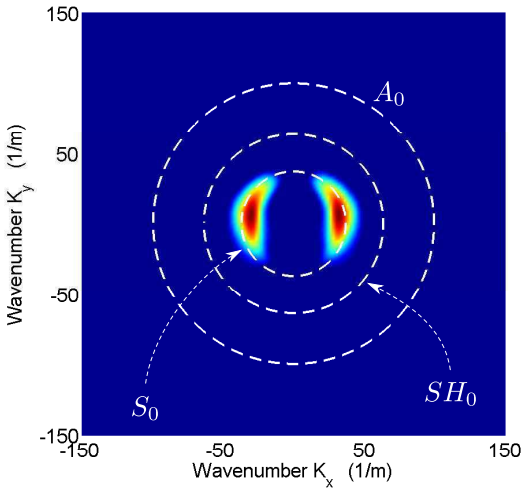

(b) Displacement U_y

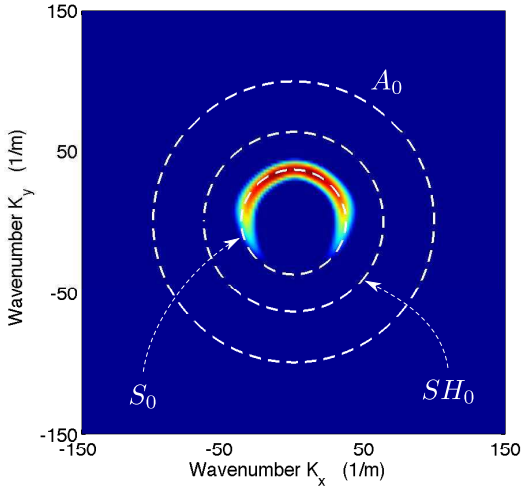

(c) Displacement U_z

Figure 72: Comparison between the analytical (dashed lines) and numerical dispersion curves of the undamaged plate computed for incident A_0 waves at 200 kHz.

Simulations are conducted using a multiscale FE code developed in-house. Although the code can handle both implicit and explicit time marching schemes, an

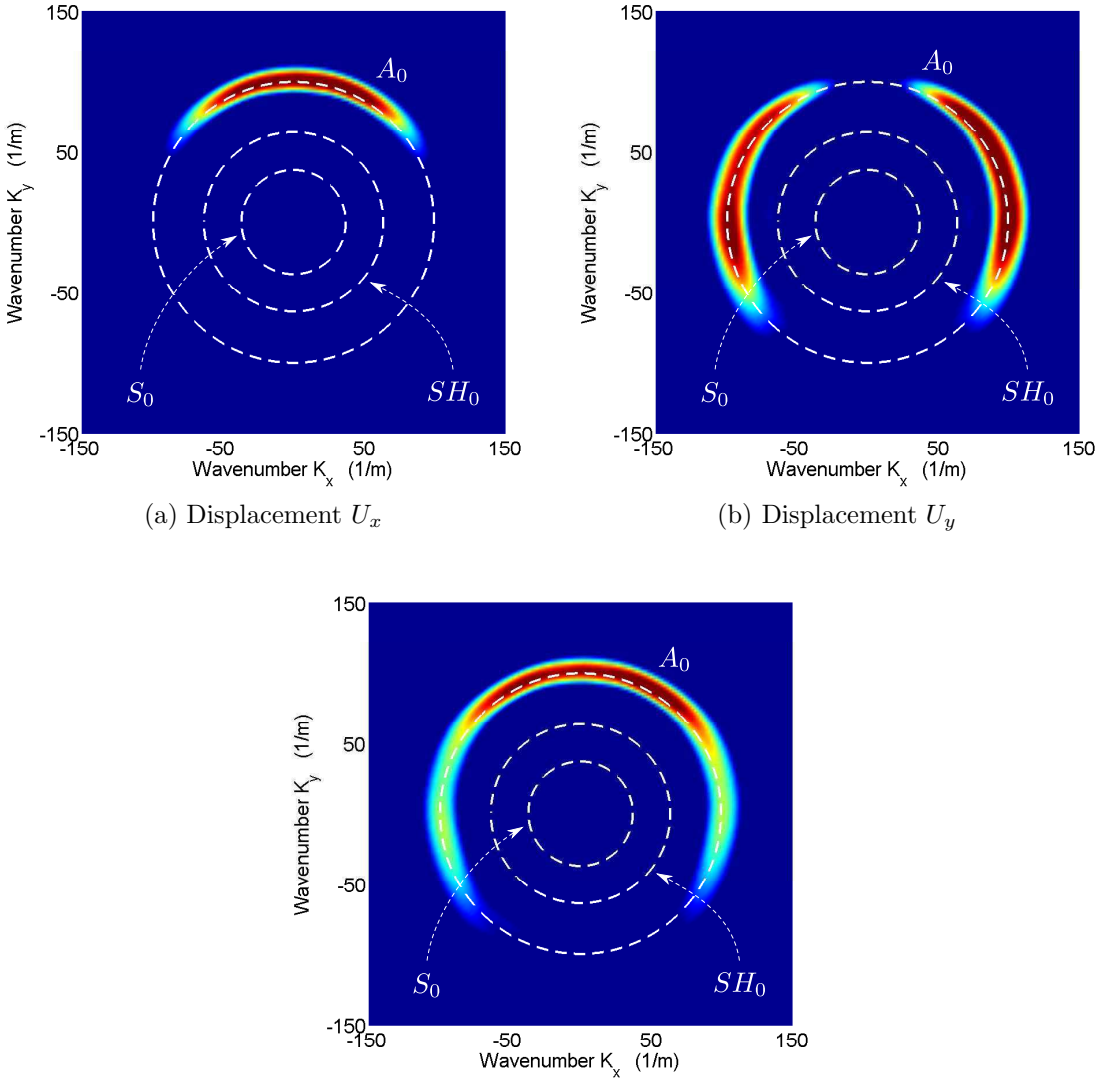

(a) Displacement U_x

(b) Displacement U_y

(c) Displacement U_z

Figure 73: Comparison between the analytical (dashed lines) and numerical dispersion curves of the undamaged plate computed for incident A_0 waves at 200 kHz.

implicit method of the Newmark family [101] is adopted because it allows for larger time steps regardless the high damping used within the absorbing layer region. The stiffness, damping and lumped mass matrices of the considered discretizations are conveniently allocated in sparse format by the 8 Gb RAM Linux machine adopted for calculations. The factorization of the effective stiffness matrix required in the time stepping algorithm is computed by means of the sparse direct solver MUMPS [11, 12].

The scattering coefficients are computed using the same procedure described in

the previous section. In the context of a 3D simulation three scattering coefficients are defined as:

$$S_{S0,\,i} = S_{S0}(\theta_i) = \frac{\mathcal{H}[\widehat{u}^{d}_{r,\,i}(t_{H_{max}})]}{\mathcal{H}[\widehat{u}^{ref}_{i}(t_{H_{max}})]} \tag{68}$$

$$S_{SH0,\,i} = S_{SH0}(\theta_i) = \frac{\mathcal{H}[\widehat{u}^{d}_{\theta,\,i}(t_{H_{max}})]}{\mathcal{H}[\widehat{u}^{ref}_{i}(t_{H_{max}})]} \tag{69}$$

$$S_{A0,\,i} = S_{A0}(\theta_i) = \frac{\mathcal{H}[\widehat{u}^{d}_{z,\,i}(t_{H_{max}})]}{\mathcal{H}[\widehat{u}^{ref}_{i}(t_{H_{max}})]} \tag{70}$$

i.e., one for each component of the wavefield recorded by the sensors. Specifically, the coefficient S_{S0} is calculated using the radial component of the scattered displacement that represents the dominant component of the S_0 Lamb mode. Similarly, S_{SH0}, and S_{A0} are computed using the hoop and vertical components of the displacement field, thus defining the SH_0, and A_0 Lamb modes respectively. The scattering coefficients in Eqs. 68 – 70 are normalized by $\widehat{u}^{ref}_{i}(t_{H_{max}})$ which denotes the dominant component of the incident wave. For instance, when S_0 incoming waves are considered, the scattering coefficients are normalized by the radial component of the incident wave, i.e., $\widehat{u}^{ref}_{i}(t_{H_{max}}) = \widehat{u}^{ref}_{r,\,i}(t_{H_{max}})$. Similarly, for incident A_0 signals the out-of-plane displacement $\widehat{u}^{ref}_{z,\,i}(t_{H_{max}})$ is used as a reference signal.

An initial study compares scattering results obtained with the proposed multiscale strategy with fully meshed FE solutions. GMsFEM calculations are conducted for incident S_0 waves and nine circular through-thickness defects with different radii ranging from 3.3% to 30% of the plate's thickness, while only three configurations are selected for the FE comparison. This choice is mostly dictated by the significant amount of modeling and simulation effort required by each FE model as described in Section 4.2. A concise representation of results is presented in Fig. 74 showing the maximum value of the scattering coefficients as a function of the defect radius. Due

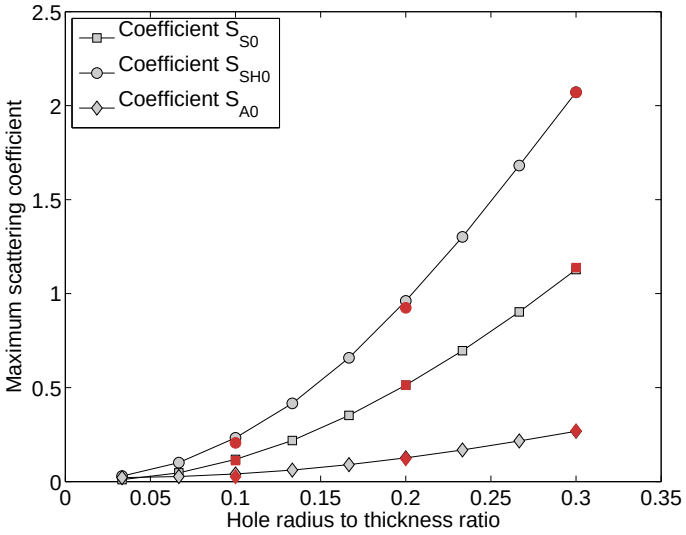

Figure 74: Maximum scattering coefficients as a function of the defect radius. The red solid markers indicate selected FE results presented for comparison.

to symmetry with respect to the plate mid-surface of both excitation and damage, components of the A_0 mode are not expected in the scattered filed. This is confirmed by results presented in Fig. 74 showing how the magnitude of S_{A0} is much smaller than the corresponding in-plane coefficients. The same figure also shows the close agreement between GMsFEM results and the selected FEM solutions. Also, Fig. 75 proposes a similar comparison over the entire angular range in order to illustrate how such agreement is not limited to the maximum value of each scattering coefficient, but is also observed for every spatial direction.

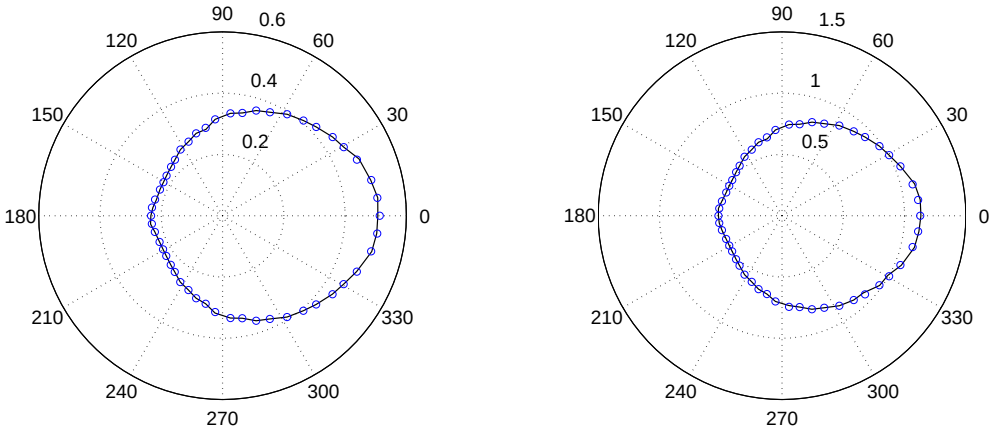

(a) S_{S0} (R=0.6 mm)

(b) S_{S0} (R=0.9 mm)

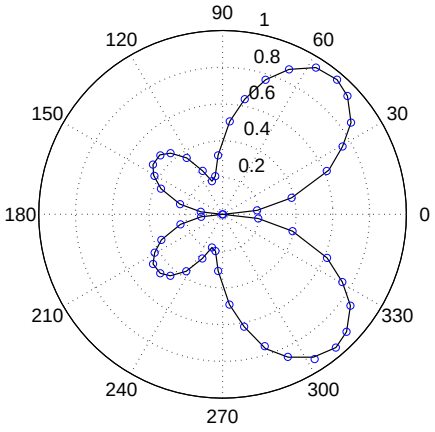

(c) S_{SH0} (R=0.6 mm)

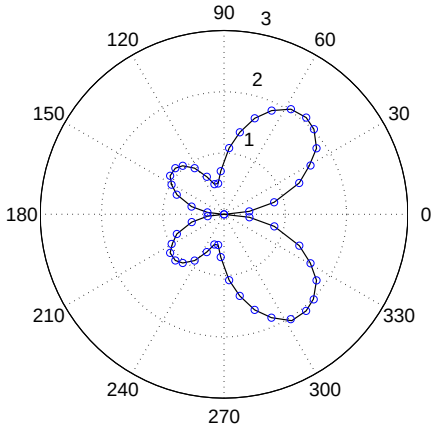

(d) S_{SH0} (R=0.9 mm)

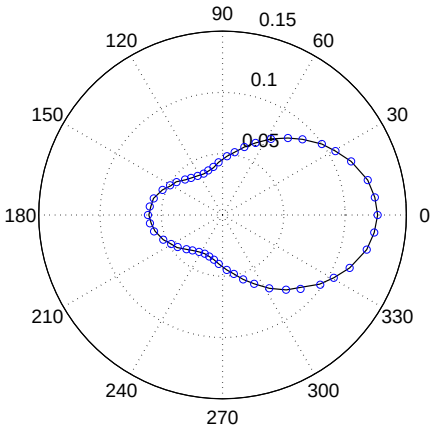

(e) S_{A0} (R=0.6 mm)

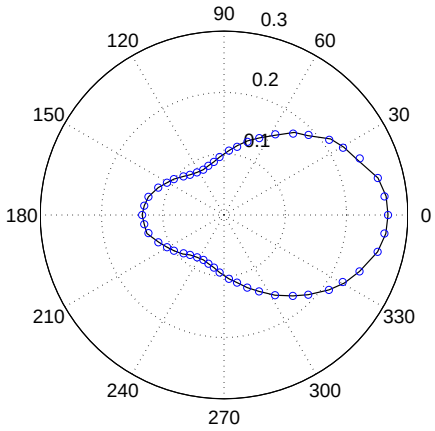

(f) S_{A0} (R=0.9 mm)

Figure 75: Comparison between the scattering diagrams computed with GMsFEM (o-markers) and FEM (solid line) for circular through-thickness defects.

4.5.2 Parametric analysis for incident S_0 waves

After the model validation described in the previous paragraph, GMsFEM is exploited to characterize the scattering patterns generated by the interaction between an incident S_0 mode at 200 kHz and elliptic defects of different size, orientation and depth. Specifically elliptic holes with major radii R_a = [0.3, 0.6, 0.9, 1.2, 1.5] mm are considered while the minor radius $R_b = 0.1$ mm is held constant in order to limit to a reasonable range the parameter space of analysis. In addition, the ellipse orientation with respect to the direction of incoming waves is varied such that θ_e = [0, 30, 60, 90] deg, while the following depths (relative to the plate thickness h) are considered δ/h = [1/5, 2/5, 3/5, 4/5]. Details of the fine-scale mesh used to model the considered configurations are shown in Fig. 76.

Results presented in Figs. 77, 78 and 79 show the variation of the scattering diagrams with respect to the defect orientation θ_e. For each diagram it is assumed that incident waves propagate from "right" to "left" along the 0 - 180 deg direction. For the sake of clarity, only a single damage configuration featuring $R_a = 0.9$ mm, and δ/h=1/5 is displayed. Results shown in Fig. 77, and 79 reveal that both S_0, and A_0 waves tend to be scattered along directions almost perpendicular to the major axis of the defect with extreme values occurring for $\theta_e = 0$ deg, and $\theta_e = 90$ deg in which waves are scattered at 90 deg and 0 deg respectively. The incident S_0 mode is in fact characterized by very little shearing components so that the scattering behavior is mostly affected by the reflection of the incident wave from the major axis of the defect. This interpretation is further corroborated by noting that the amplitude of the three scattering coefficients tend to gradually increase as the orientation angle θ_e approaches 90 deg that is when a larger portion of the damage length is exposed to the direction of the incident signal. Polar diagrams of the scattered shear wave (SH_0) are shown in Fig. 78. An interesting behavior is revealed in Fig. 78.a illustrating that defects elongated along the direction of the incoming signal tend to reflect shear

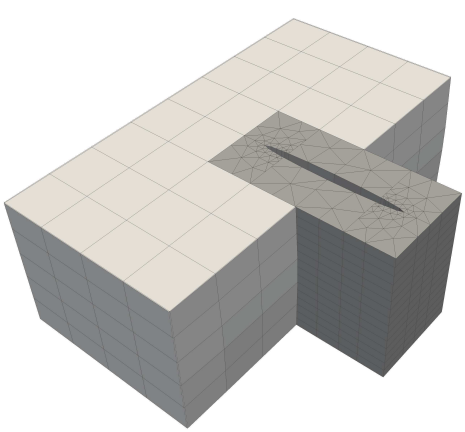

(a) $R_a = 1.5$ mm, $\theta_e = 0$ deg

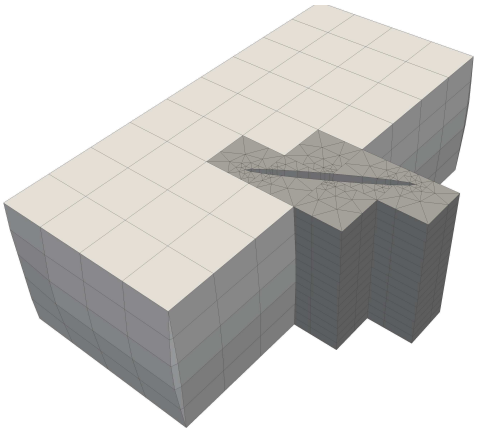

(b) $R_a = 1.5$ mm, $\theta_e = 30$ deg

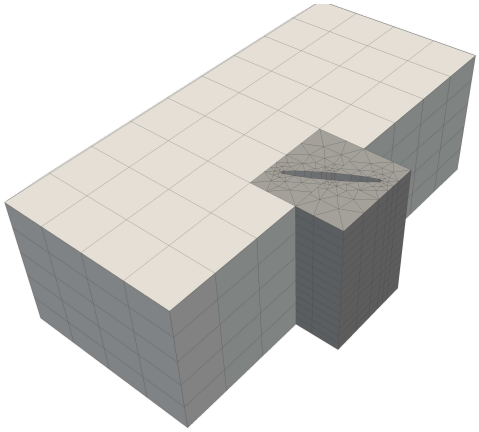

(c) $R_a = 0.9$ mm, $\theta_e = 30$ deg

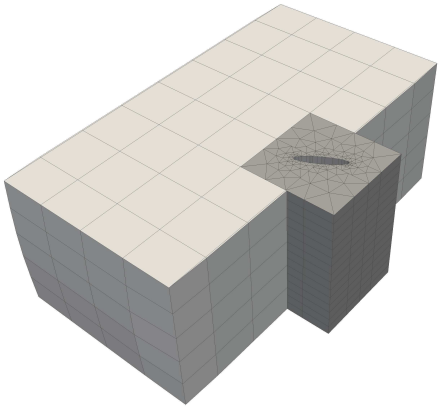

(d) $R_a = 0.5$ mm, $\theta_e = 30$ deg

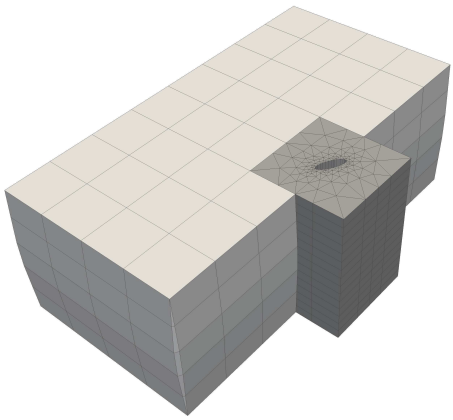

(e) $R_a = 0.3$ mm, $\theta_e = 60$ deg

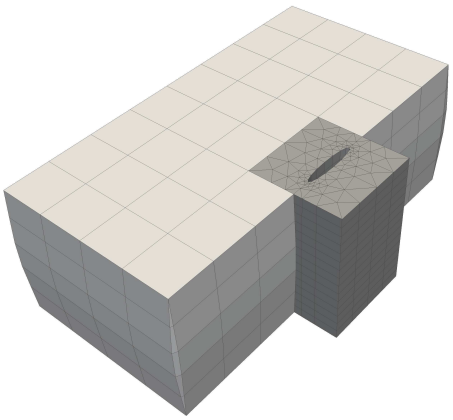

(f) $R_a = 0.6$ mm, $\theta_e = 90$ deg

Figure 76: Detail of multiscale elements used to model selected damage configurations.

waves "backwards" that is along the direction of incidence. This is fundamentally different from what was observed for holes with a more circular shape, which tend to scatter shear waves in the transverse direction with maxima occurring "forward" that is opposite to the direction of the incident wave as shown, for example, in Fig. 75.c,d or even for the 2D case in Figs. 63.a,c,e and 64.a,c,e. When the considered defect is oriented at an angle θ_e the classical four-lobed shape, typical of circular holes, is restored, as shown in Fig. 78.b,c,d.

The scattering diagrams for different values of R_a and fixed depth ($\delta/h = 2/5$) are illustrated in Fig. 80. The defect's radii are expressed in terms of the incident wavelength ($\lambda_{S0} = 26.8$ mm) to provide insights on the effects of the excitation frequency on directivity. As expected, the magnitude of the scattering plots reduces as the wavelength increases with respect to the characteristic length of the defect. This implies that a higher excitation frequency is required to maintain the same sensitivity to smaller defects. Results also indicate that the shape of the scattering plots is slightly affected by the size to wavelength ratio. Such a change is also partially related to the different eccentricity of the ellipse since, in this study, its minor axis $R_b = 0.1$ mm is held constant while R_a changes.

A combined representation of the effects of the defect's depth (δ), and size (R_a) on the scattering coefficients is shown in Fig. 81. Since such parameters do not significantly affect directionality, only the maximum amplitude of each coefficient is shown in a surface representation as a function of δ, and R_a. This analysis confirms the physical intuition such that the magnitude of the scattered wavefield increases for increasing values of the hole radius and depth that constitute a measure of the "severity" of damage. Specifically, results shown in Fig. 81.a,c indicate how the magnitude of S_0 and A_0 waves increases more rapidly for increasing values of R_a when $\delta/h > 60\%$ that is when the defect is deep relative to the plate thickness. A similar behavior is observed in Fig. 81.b showing that maximum scattering of SH_0

waves occurs both for high values of $R_a/h > 30\%$ and $\delta/h > 60\%$. A similar trend is observed for other orientation angles θ_e (not shown for clarity) confirming that the defect orientation θ_e primarily affects the directions of the scattered wavefield but has a minor influence on its magnitude.

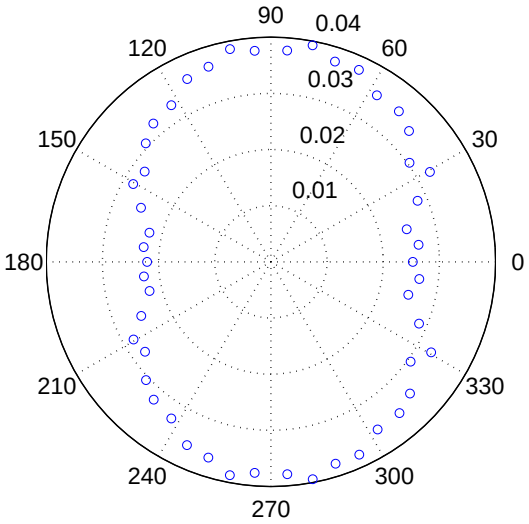

(a) S_{S0} ($\theta_e = 0$ deg)

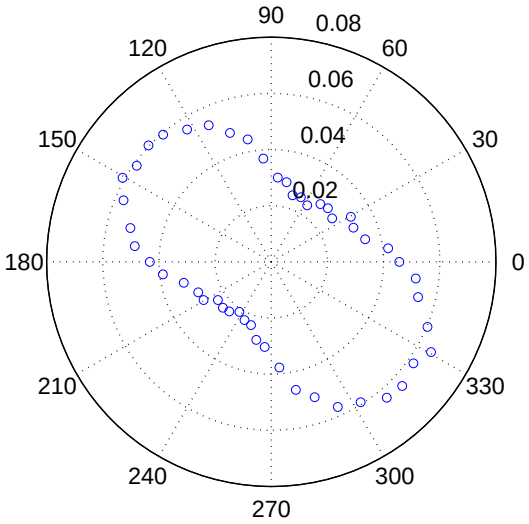

(b) S_{S0} ($\theta_e = 30$ deg)

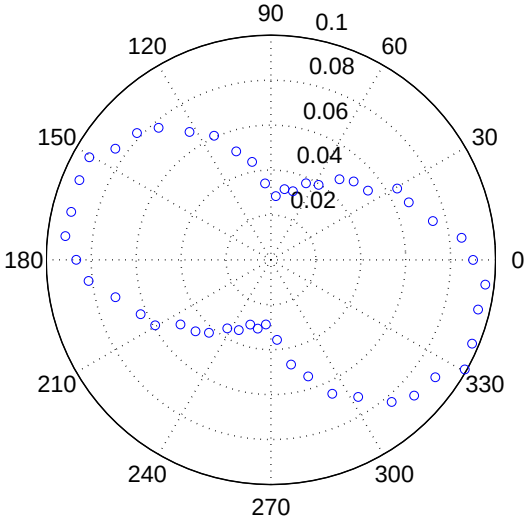

(c) S_{S0} ($\theta_e = 60$ deg)

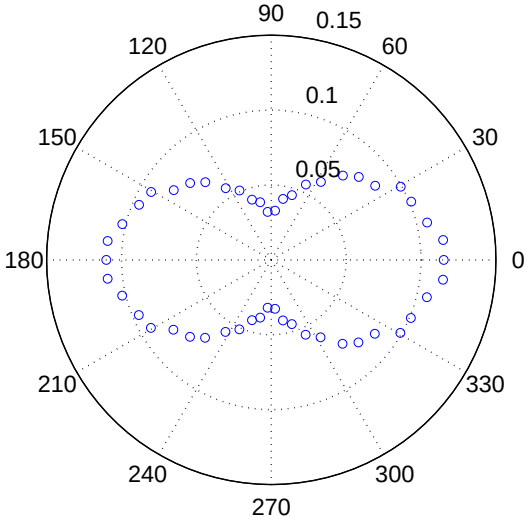

(d) S_{S0} ($\theta_e = 90$ deg)

Figure 77: Scattering diagrams (S_{S0}) computed for incident S_0 waves and elliptic defects ($R_a = 0.9$ mm, δ/h=1/5) with different orientation.

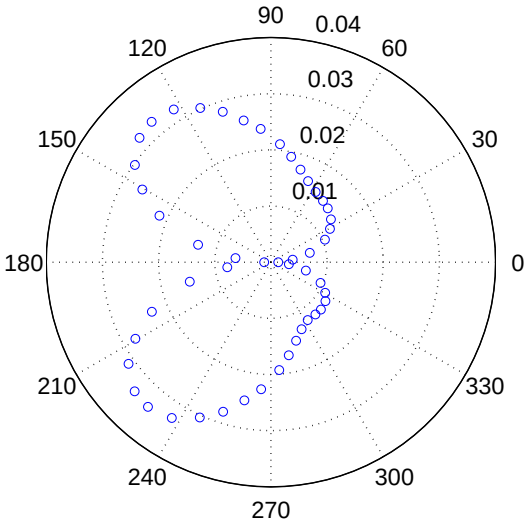

(a) S_{SH0} ($\theta_e = 0$ deg)

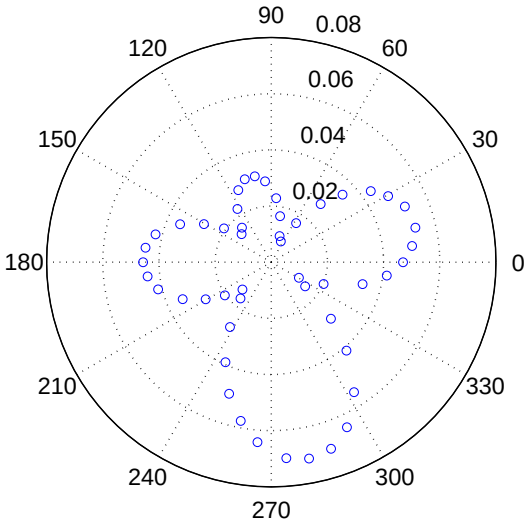

(b) S_{SH0} ($\theta_e = 30$ deg)

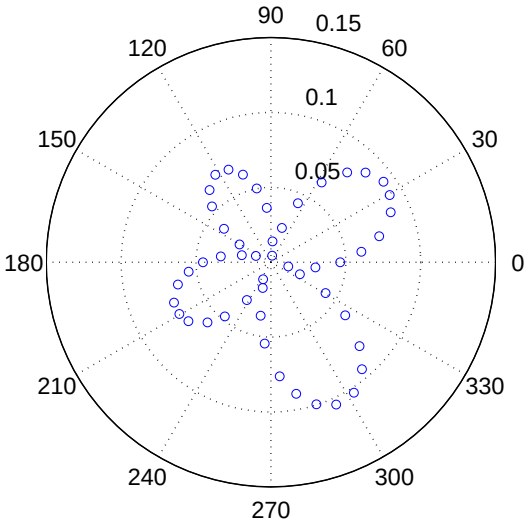

(c) S_{SH0} ($\theta_e = 60$ deg)

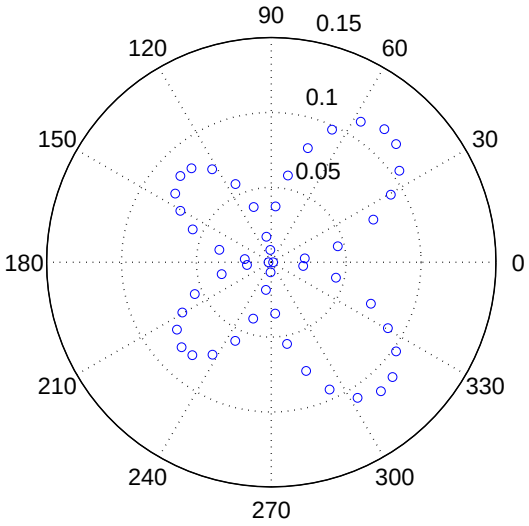

(d) S_{SH0} ($\theta_e = 90$ deg)

Figure 78: Scattering diagrams (S_{SH0}) computed for incident S_0 waves and elliptic defects ($R_a = 0.9$ mm, δ/h=1/5) with different orientation.

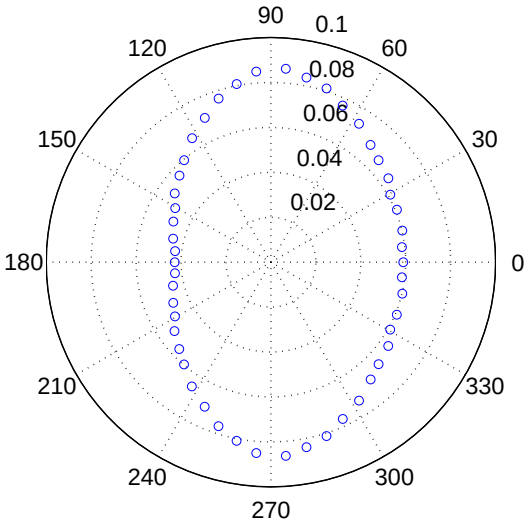

(a) S_{A0} ($\theta_e = 0$ deg)

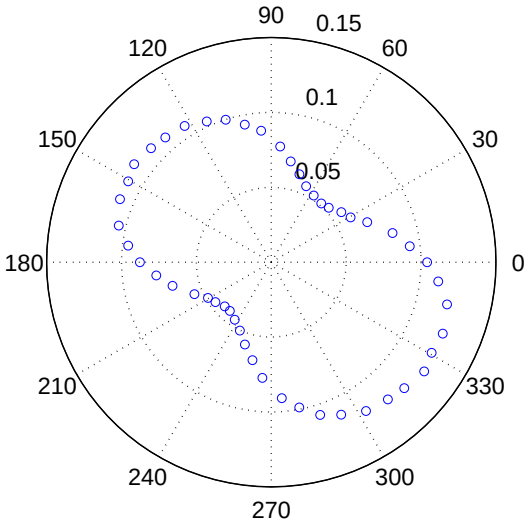

(b) S_{A0} ($\theta_e = 30$ deg)

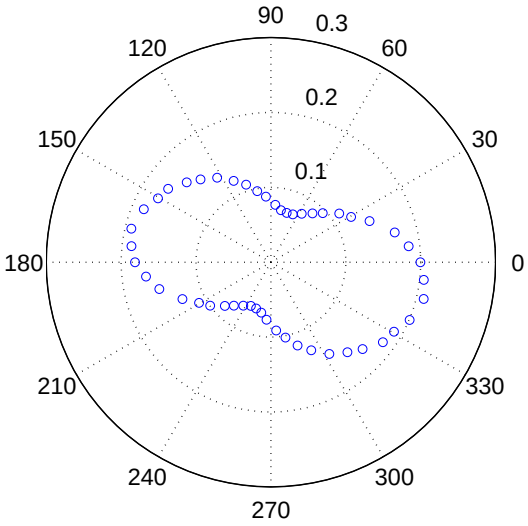

(c) S_{A0} ($\theta_e = 60$ deg)

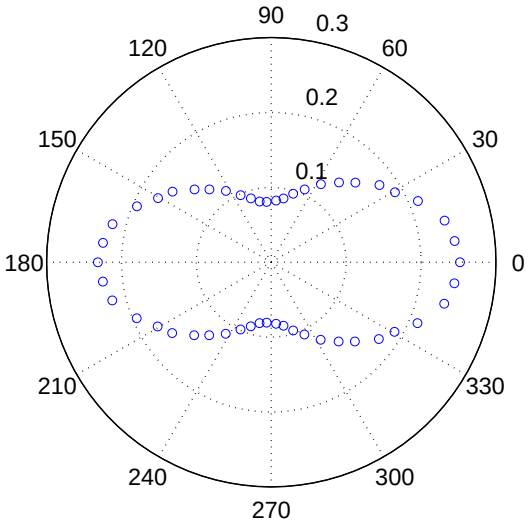

(d) S_{A0} ($\theta_e = 90$ deg)

Figure 79: Scattering diagrams (S_{A0}) computed for incident S_0 waves and elliptic defects ($R_a = 0.9$ mm, δ/h=1/5) with different orientation.

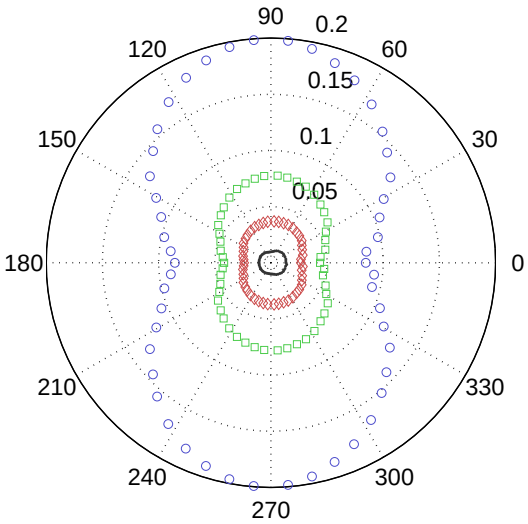

(a) S_{S0} ($\theta_e = 0$ deg)

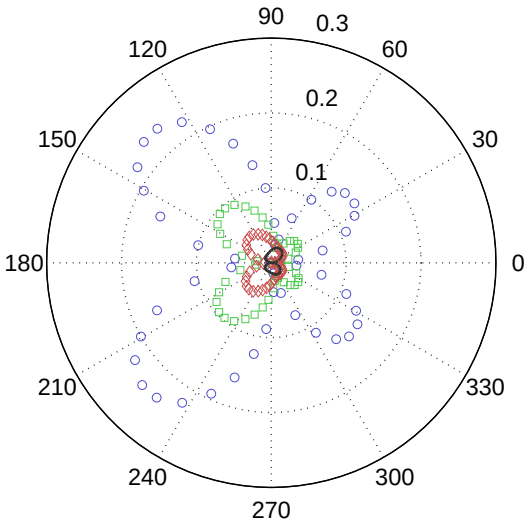

(b) S_{SH0} ($\theta_e = 0$ deg)

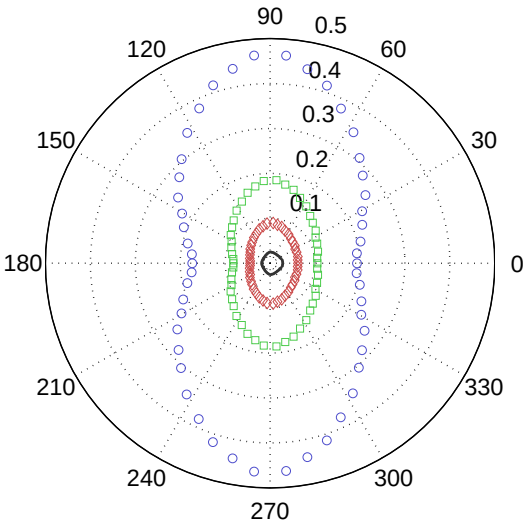

(c) S_{A0} ($\theta_e = 0$ deg)

Figure 80: Scattering coefficients computed for incident S_0 waves as a function of the defect's radius to wavelength ratio: 5.6% (blue-o-markers), 3.4% (green-□-markers), 2.2% (red-◇-markers), and 1.1% (gray-●-markers) with $\delta/h = 2/5$.

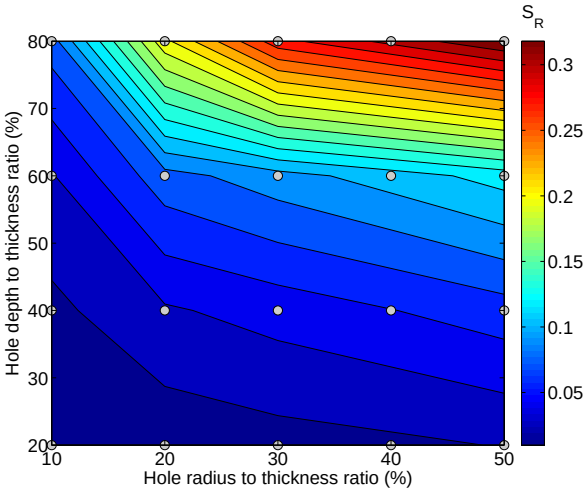

(a) S_{S0} ($\theta_e = 0$ deg)

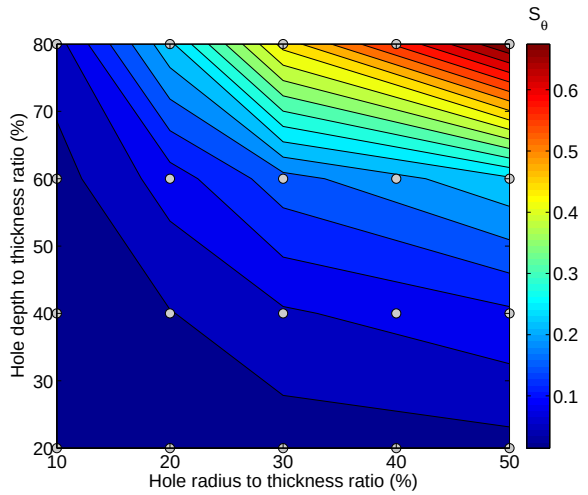

(b) S_{SH0} ($\theta_e = 0$ deg)

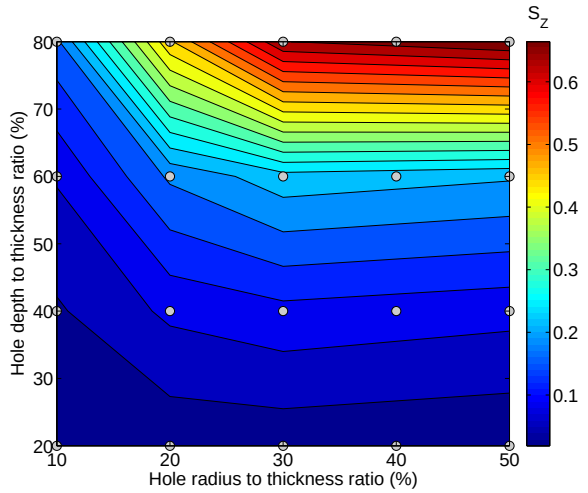

(c) S_{A0} ($\theta_e = 0$ deg)

Figure 81: Maximum scattering coefficients computed for incident S_0 waves and selected combinations of the defect's depth and size (highlighted with ∘-markers) and $\theta_e = 0$ deg.

4.5.3 Parametric analysis for incident A_0 waves

Scattering results for incident A_0 waves are presented considering the same damage configurations and parameter set adopted in the previous study. Whereas incident S_0 waves are characterized just by their dominant stress and displacement components in the direction of travel, the A_0 mode considered herein features significant shear stress and lateral dis- placement components. This plays an important role for the directivity of S_0 and A_0 waves whose diagrams are shown in Fig. 82 and 84 respectively. Contrary to the previous case of incident S_0 waves, it is interesting to notice how both the S_r and S_z diagrams shown in Fig. 82.a and 84.a (i.e. when $\theta_e = 0$) feature a more rounded pattern induced by the multiple components of the displacement field simultaneously impacting on the defect. As the orientation angle θ_e increases the directivity diagrams of the considered modes assume the classical double-lobed shape as observed also in the case of incident S_0 waves. The effect of an incident A_0 mode also influences the polar diagram of the scattered SH_0 mode (see Fig. 83) especially at $\theta_e = 0$ where two minor backward lobes appear indicating a partial transverse reflection of the scattered displacement.

Figure 85 shows the scattering diagrams computed for different values of R_a and fixed depth ($\delta/h = 2/5$) and orientation ($\theta_e = 0$ deg). Similarly to what previously observed, the magnitude of the scattered wavefield reduces for decreasing values of the damage's size to wavelength ratio. Instead, in this case the directivity shape appreciably changes. The A_0 signal is in fact characterized by a more complex mode shape compared to its symmetric counterpart [81], which increases the sensitivity to the defect's length and eccentricity.

The sensitivity of the scattered wavefield to the defect's size and depth is presented in Fig. 86 for an elliptical defect with $\theta_e = 90$ deg. Results obtained for other orientations (not shown for clarity) are qualitatively the same. The sensitivity of S_{S0} and S_{A0} are illustrated in Fig. 86.a,c which does not show much difference from

analogous results obtained when S_0 incident modes are considered as shown in Fig. 81. However, an interesting difference in observed in the behavior of the scattered SH_0. For instance Fig. 86.b shows that the sensitivity of the considered mode to the hole radius (R_a), significantly increases even for small defects characterized by $R_a/h > 10\%$ provided that $\delta/h > 60\%$. The same diagrams also reveal that the amplitude of the scattered SH_0 waves does not change much when $R_a/h > 30\%$ and $\delta/h > 60\%$.

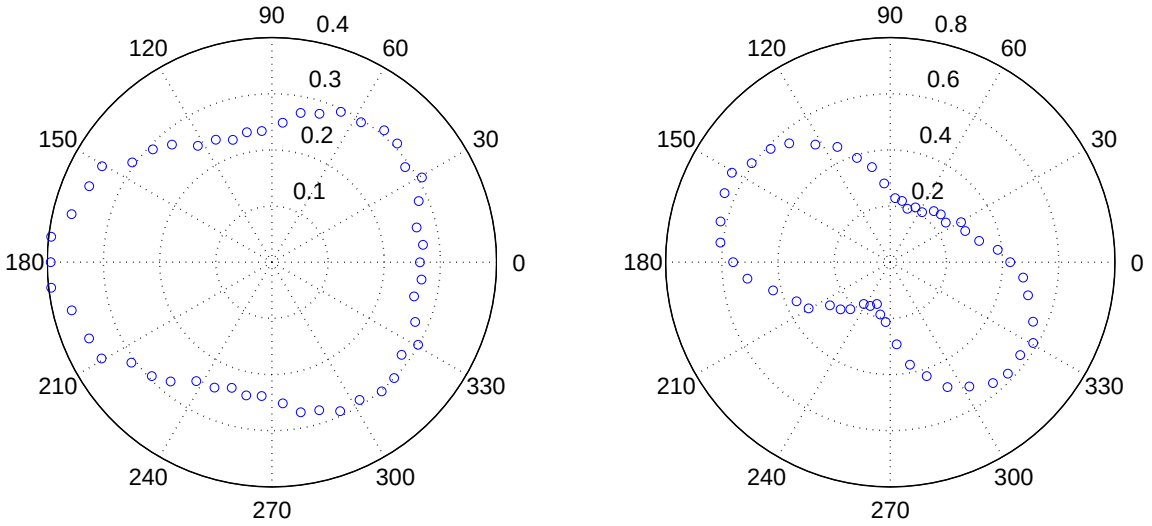

(a) S_{S0} ($\theta_e = 0$ deg)

(b) S_{S0} ($\theta_e = 30$ deg)

(c) S_{S0} ($\theta_e = 60$ deg)

(d) S_{S0} ($\theta_e = 90$ deg)

Figure 82: Scattering diagrams (S_{S0}) computed for incident A_0 waves and elliptic defects ($R_a = 0.9$ mm, δ/h=1/5) with different orientation.

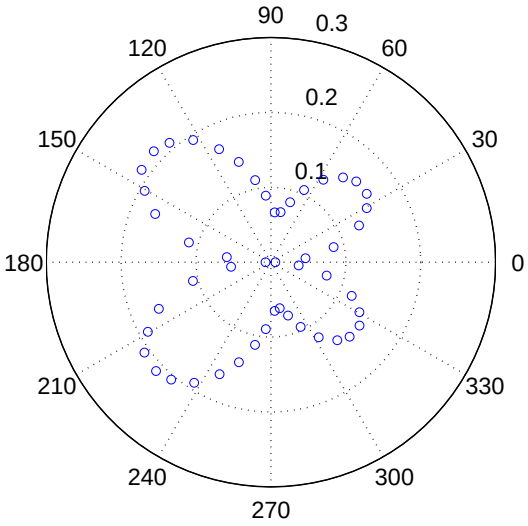

(a) S_{SH0} ($\theta_e = 0$ deg)

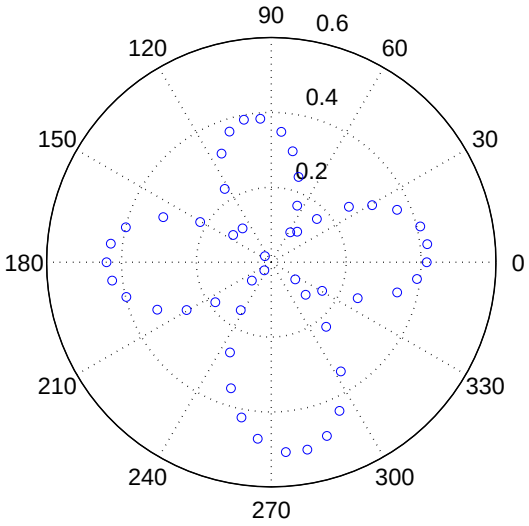

(b) S_{SH0} ($\theta_e = 30$ deg)

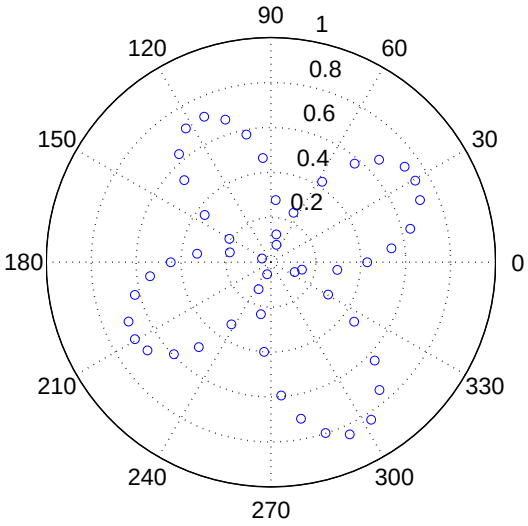

(c) S_{SH0} ($\theta_e = 60$ deg)

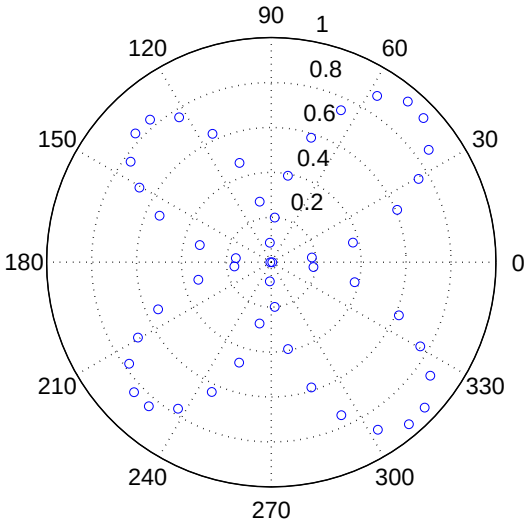

(d) S_{SH0} ($\theta_e = 90$ deg)

Figure 83: Scattering diagrams (S_{SH0}) computed for incident A_0 waves and elliptic defects ($R_a = 0.9$ mm, δ/h=1/5) with different orientation.

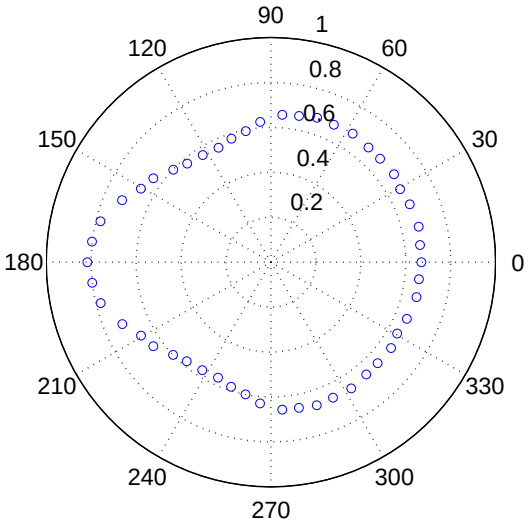

(a) S_{A0} ($\theta_e = 0$ deg)

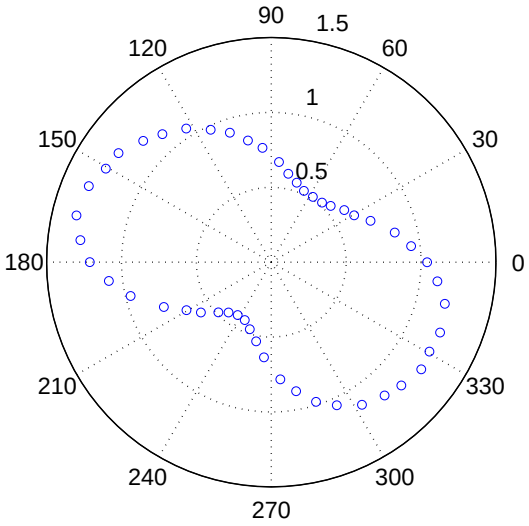

(b) S_{A0} ($\theta_e = 30$ deg)

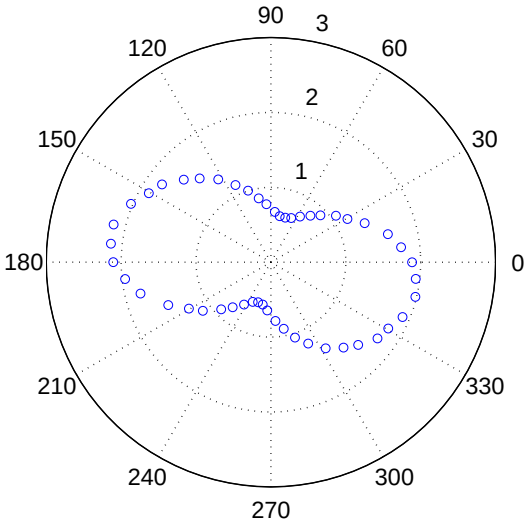

(c) S_{A0} ($\theta_e = 60$ deg)

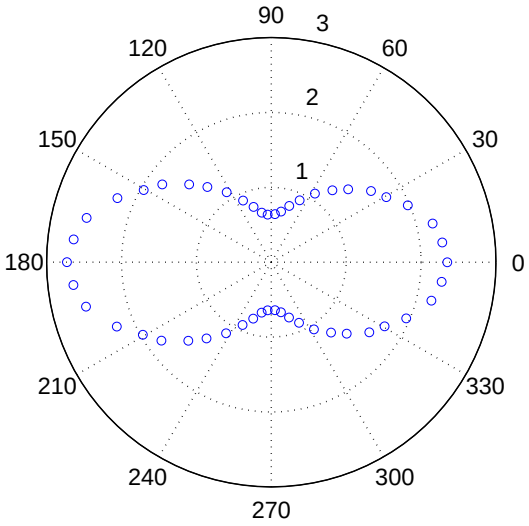

(d) S_{A0} ($\theta_e = 90$ deg)

Figure 84: Scattering diagrams (S_{A0}) computed for incident A_0 waves and elliptic defects ($R_a = 0.9$ mm, δ/h=1/5) with different orientation.

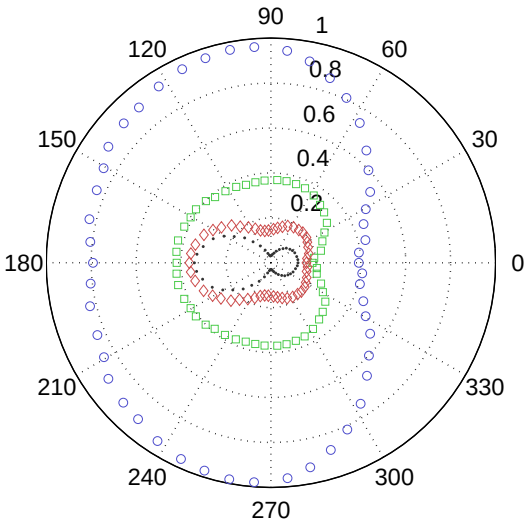

(a) S_{S0} ($\theta_e = 0$ deg)

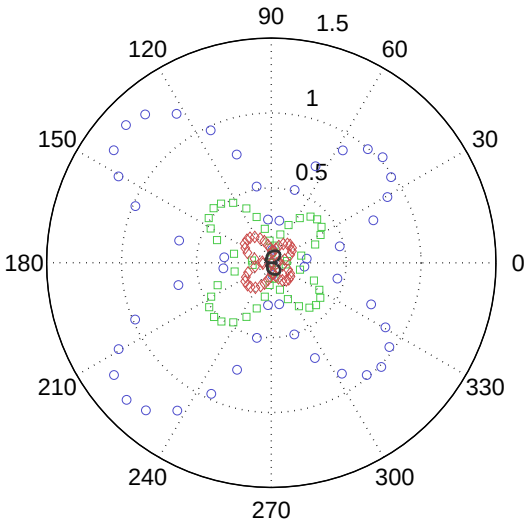

(b) S_{SH0} ($\theta_e = 0$ deg)

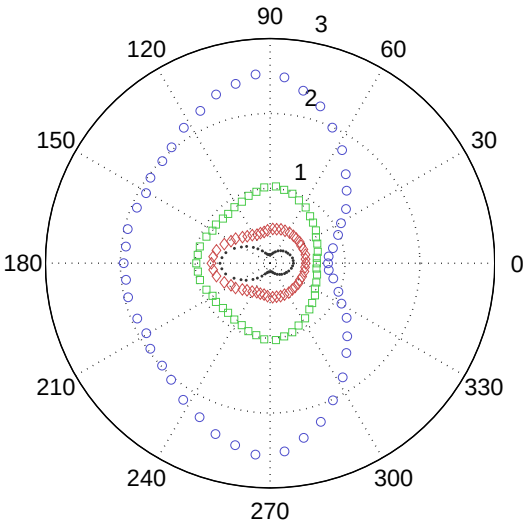

(c) S_{A0} ($\theta_e = 0$ deg)

Figure 85: Scattering coefficients computed for incident A_0 waves as a function of the defect's radius to wavelength ratio: 15% (blue-o-markers), 9% (green-□-markers), 6% (red-◇-markers), and 3% (gray-•-markers) with $\delta/h = 2/5$.

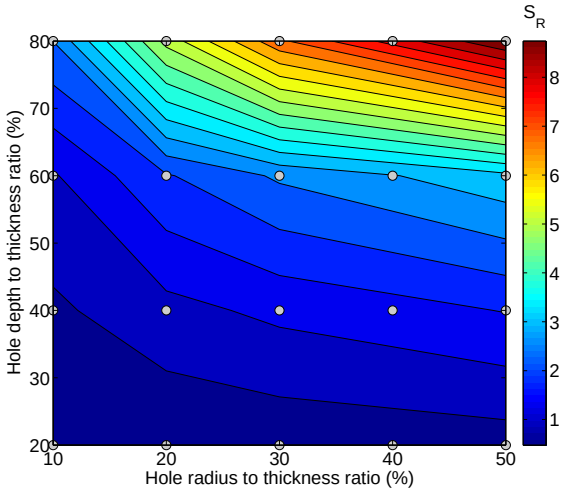

(a) S_{S0} ($\theta_e = 90$ deg)

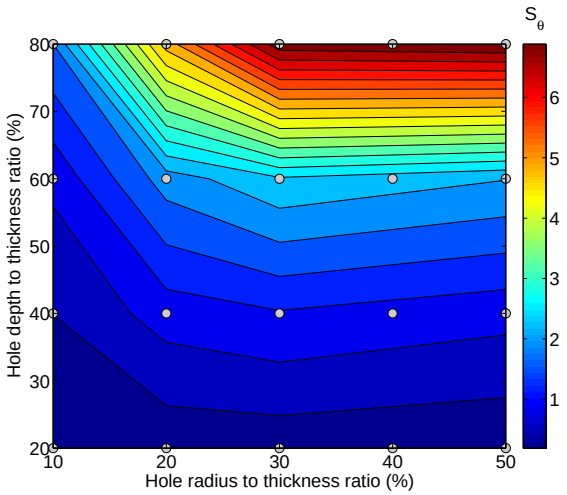

(b) S_{SH0} ($\theta_e = 90$ deg)

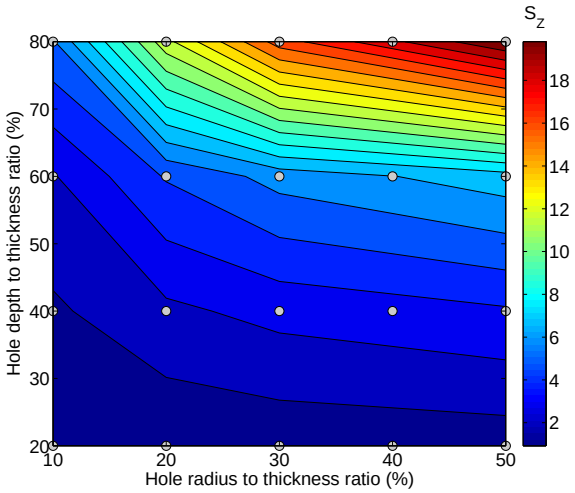

(c) S_{A0} ($\theta_e = 90$ deg)

Figure 86: Maximum scattering coefficients computed for incident A_0 waves and selected combinations of the defect's depth and size (highlighted with ∘-markers) and $\theta_e = 90$ deg.

4.6 Conclusions

In this chapter, GMsFEM is used to investigate the interaction between elastic waves and defects of different nature. A first illustrative example shows how the proposed method allows to model small defects without requiring overly-refined or *ah hoc* meshes by simply exploiting the modeling flexibility offered by the proposed multi-node elements. Multiscale elements' ability to guarantee compatible solutions with adjacent elements also allows incorporating irregular defects without compromising the quality of the numerical grid surrounding the damaged area. Comparison with analogous FE solutions of transient simulations shows excellent agreement of results for defects of different size, all modeled by means of one single MSE. Successive analyses characterize the wavefield scattered by small defects in otherwise homogeneous metallic plates. Two-dimensional simulations are first exploited to investigate the behavior of plates with both in-plane and through-thickness defects. Analyses involving simple configurations compare and validate the obtained results with FE solutions. Parametric studies for varying defect geometries are also conducted in order to characterize the structural response of damaged components in terms of wave reflection coefficients and scattering directivity diagrams. The final section is devoted to the analysis of wave scattering from elliptic defects in a three-dimensional plate. Emphasis is given on the interaction between incident S_0 and A_0 waves with defects much smaller than the incoming wavelength. Such cases, often characterized by defects approaching the length scale of the underlying discretization, provide a suitable scenario for the application of the proposed multiscale strategy. Multiscale elements allow in fact for the correct geometrical representation of damage without over-stiffening the model since the characteristic wavelengths of deformation are larger than the spatial scale of the discretization. One of the advantages observed in the application of GMsFEM to damage modeling are related to the reduction of the number of nodes explicitly retained in the model. This clearly reduces the memory and CPU time

required for simulations, even if some extra computational time is required for the calculation of multiscale shape functions. The proposed method also allows systematically modeling complex geometries without requiring a complete remeshing of the entire computational domain. This aspect is definitely a major advantage of GMsFEM especially when several parametric analyses need to be carried out.

CHAPTER V

CONCLUSIONS AND FUTURE WORK

5.1 Summary

This research investigates the development and application of a geometric multiscale finite element method (GMsFEM) for the analysis of wave propagation in heterogeneous media. The proposed methodology extends the current multiscale modeling capabilities by combining the idea of multi-node elements to the concept of numerical shape functions proper of MsFEM methods. Multiscale shape functions for arbitrarily-shaped elements are derived through the minimization of the global energy of the problem. The resulting interpolation operator is used to project the fine-scale mass and stiffness matrices onto the space of the macroscopic model. This allows describing both the elastic and inertial properties of multiscale elements in terms of a limited number of nodal information. The problem of multiscale elements' conformity is addressed by means of a formalism that identifies conditions on the fine-scale mesh which guarantee uniqueness of displacements across the element boundaries. The results of this analysis can be summarized as follows:

- Multiscale shape functions computed with quadrilateral-faced elements, such as hexahedral or wedge elements, are conforming if the edges of the local grid are aligned to the natural coordinates of the inter-element boundary,
- Multiscale shape functions computed with fine-scale tetrahedral elements are never conforming with adjacent hexahedral elements,
- Numerical errors due to incompatible shape functions tend to zero as the fine-scale mesh is refined.

The proposed multiscale method is first applied for the calculation of the dispersion properties of periodic solids. According to the unit cell analysis approach, the representative volume element is discretized by means of both multiscale and regular finite elements, and the dispersion relations of the periodic medium are determined as the solution of an eigenvalue problem with periodic boundary conditions. Numerical examples show how the proposed GMsFEM allows discretizing the computational domain using a limited number of global information describing only the relevant geometrical features of the cell. Results predicted with GMsFEM are in good agreement with the corresponding fine-scale solution in frequency ranges where the wavelength of deformation is of the order of the unit cell or larger. Conventional mesh refinements can be exploited to capture the behavior of the system at higher frequencies that is typically characterized by local deformation patterns within the unit cell. The GMsFEM is also used to investigate the anisotropic behavior of periodic structural lattices, and the dispersion properties of a phononic stubbed plate. In the latter example, both low- and high- frequency results are validated by means of experimental measurements.

The GMsFEM is finally applied to investigate the interaction between elastic waves and defects in metallic plates. Multiscale elements are exploited to seamlessly model holes that are smaller than the incoming wavelength without requiring mesh refinements and distortion. Defects with different size and shape are also modeled without requiring a complete remeshing of the domain. Transient simulations of wave propagation in two- and three-dimensional plate-like structures are used to compute the wavefield scattered by the defects. Parametric studies conducted for varying damage geometries correlate the defect's geometry to the directivity patterns for both incident symmetric (S_0) and anti-symmetric (A_0) Lamb waves.

5.2 Research contributions

The research presented in this thesis provides the following unique contributions:

- Formulation and implementation of a Geometric Multiscale Finite Element Method (GMsFEM) for transient wave simulations in heterogeneous structures
- Derivation of the compatibility conditions required for the implementation of the method in three dimensions
- Application of GMsFEM for the calculation of the dispersion properties of periodic solids, structural lattices, and phononic crystals
- Application of GMsFEM to the problem of wave scattering from partial-depth elliptic defects in homogeneous metallic plates
- Parametric study of the scattering directivity diagrams associated to defects of different size and geometry

5.3 Future work

1. **Analysis of delamination in composites**

   In recent years, the use of fiber-reinforced composite laminates has steadily increased in many fields of engineering including aerospace, civil, maritime, and automotive. Composite panels are particularly attractive for their high stiffness to weight ratio, and high corrosion resistance. Compared with traditional metallic materials, composites are also characterized by several damage and failure mechanisms such as delamination, matrix cracking, and fiber breakage. The analysis of wave scattering due to such defects in composite laminates represents a rather unexplored branch of research in SHM. The application of wave-based inspection techniques to laminated composites represents a challenging task due to their anisotropic nature and multilayer characteristics. In

order to provide predictive results, numerical models must reflect such properties as well as a proper description of the damage topology. Typical defects are represented by delamination due to impacts or cyclic stresses that generate irregular regions of disbond between the laminae. In this context, the proposed multiscale method could be exploited to model the actual shape of damage present in three-dimensional plate models.

2. **Application to structural elements**

   In this thesis the proposed multiscale procedure is only applied to continuum elements. However, the same formalism can be extended to formulate multiscale elements describing the behavior of plate or shell structures typically analyzed by means of specialized structural elements. Whereas the numerical formulation of the method remains virtually the same, technical difficulties related to the implementation of efficient and reliable triangular elements at the fine-scale level may arise. The formulation of multiscale plate or shell elements with defects would allow modeling not only damage or material heterogeneities but also the presence, for example, of rivet holes and other structural details that are often the source of high stress concentration factors.

3. **Dynamic enrichment shape functions**

   Ample opportunities for further research are provided by the shortcomings of the method described in the previous section. In particular, the proposed set of multiscale shape functions could be complemented by an additional enrichment basis containing information regarding the dynamic properties of the element. For instance, the enrichment basis could be sought among the space of eigensolutions of the constrained fine-scale problem, or alternatively obtained by means of dynamic condensation procedures [105]. This would allow for larger elements

capable of capturing local dynamic deformations, but the need to satisfy inter-element compatibility still limits the range of possible applications. Also, for the analysis of periodic solids, Bloch eigenmodes could be exploited as additional basis functions for the calculation of the element matrices. Clearly this choice would facilitate the calculation of the dispersion relations based on the unit cell approach, but difficulties would arise for the formulation of compatible elements to be used for the analysis of assemblies of finite size. Finally, a new frontier for multiscale analysis could be sparked by the use of experimentally measured dynamic shape functions. Such possibility is currently under investigation under the support of an NSF grant.

4. **Multiscale nonlinear and fracture mechanics**

   The design of engineering components that exploit materials under extreme working conditions demands an increasing understanding of their nonlinear behavior. The implementation of both material and geometrical nonlinearities would significantly broaden the range of possible applications of the developed multiscale methodology. This would include, among others, strength and stability analysis of heterogeneous materials and structures, with possible applications in areas such as fracture mechanics. To this end, it is particularly interesting the possibility of exploiting the fine-scale mesh as a means to compute both multiscale shape functions and the new directions of crack growth. Also, numerical modeling of crack propagation would definitely benefit by the implementation of an adaptivity scheme whereby multiscale elements are automatically generated along the direction of crack growth.

5. **Extension to multi-physics modeling**

   In several engineering applications multi-physics couplings are exploited as the enabling mechanisms to achieve unique design goals. For instance, piezoelectric

devices coupled with electrical networks have been exploited as sub-wavelength resonators for the design of tunable acoustic metamaterials. Also, small piezoelectric disks are commonly used as sensors or actuators for the generation of guided waves in metallic and composite plates. The numerical modeling, within a finite element framework, of such components could avail of the definition of "active" multiscale elements whose implementation can be straightforwardly derived from the proposed formulation. Also, the implementation of MSEs with embedded coupling with micro-scale fluid cavities could be exploited for the design of phononic porous media with sound absorption properties, and additional impedance effects useful for elastic wave steering.

5.4 Concluding remarks

The focal point of this research is represented by the developed GMsFEM. Inspired by the research on multiscale FE methods, the concept of numerical shape functions is extended to multi-node elements with arbitrary shape that are used to model multiscale features occurring at the geometrical level. The GMsFEM formulation proposed herein highlights the similarity between the aforementioned class of multiscale FE methods and the static condensation approach. Whereas the proposed methodology extends the panorama of possible applications of static model reduction, it also inevitably inherits some of its major drawbacks. For instance, one is associated to the approximate description of the inertial properties of multiscale elements that are expressed by means of an interpolation or "reduction" operator based on the elastic properties of the fine-scale. Also, the linearity constraints used to ensure inter-element compatibility may overestimate the stiffness of the element. The interplay between these two aspects requires multiscale elements with a number of global nodes that captures the correct deformation mechanism of the MSE. This makes the GMsFEM particularly appealing when the wavelength of deformation is large compared to the

size of a single MSE since a few number of coarse-scale nodes is sufficient to describe the dynamic behavior of the system. Increasing the number of global information explicitly retained in the MSE extends the frequency range of application of the method but also increases its computational cost.

The GMsFEM is found particularly convenient to study the effective anisotropic properties of a structural lattice – both in terms of wave velocities and for transient simulations in the time domain. The proposed method is also well suited to investigate the interaction between elastic waves and defects that are smaller than, or of the same order as, the incident wavelength. In such cases MSEs are used to model the damage without requiring mesh refinements, and parametric studies for defects of different size and geometries can be conducted without remeshing the entire domain.

APPENDIX A

DERIVATION OF THE GEOMETRIC INTERPRETATION OF INTER-ELEMENT COMPATIBILITY

Consider the affine map $\mathcal{M}_3$ introduced in Fig. 9. Such isoparametric transformation maps the element (a,b,c,d) expressed in the (r, s) space into the master, or reference, element in the (ξ, η) space. The point $P(r_p, s_p)$ is transformed accordingly into $\bar{P}(\overline{\xi}_p, \overline{\eta}_p)$ that is in general different from the point $P(\xi_p, \eta_p)$ resulting from the transformation $\mathcal{M}_2$.

By definition, the test function ϕ evaluated at point $P(r_p, s_p)$ can be written as:

$$\phi_p = \overline{\boldsymbol{h}}(\overline{\xi}_p, \overline{\eta}_p)^T \boldsymbol{\phi}_\alpha \tag{71}$$

where $\boldsymbol{\phi}_\alpha = [\phi_a, \phi_b, \phi_c, \phi_d]$, defines the value of the test function ϕ at the four corners (a,b,c,d) of the fine-scale element.

As mentioned in Section 2.3.1, $\boldsymbol{\phi}_\alpha = \boldsymbol{\mathcal{H}}\,\boldsymbol{\phi}$ where $\boldsymbol{\mathcal{H}}$ is a matrix of known coefficients used to impose the constraints on the nodes of the fine-scale mesh, and $\boldsymbol{\phi} = [\phi_1, \phi_2, \phi_3, \phi_4]$. Also, recall that the isoparametric map $\mathcal{M}_1$ allows writing the test function ϕ_p as:

$$\phi_p = \boldsymbol{h}(r_p, s_p)^T \boldsymbol{\phi} \tag{72}$$

Substituting Eq. (72) into Eq. (71) gives:

$$\boldsymbol{h}(r_p, s_p)^T \boldsymbol{\phi} = \overline{\boldsymbol{h}}(\overline{\xi}_p, \overline{\eta}_p)^T \boldsymbol{\mathcal{H}}\,\boldsymbol{\phi} \tag{73}$$

Clearly, Eq. (73) must hold for every values of the test function $\boldsymbol{\phi}$ which implies that:

$$\boldsymbol{h}(r_p, s_p)^T = \overline{\boldsymbol{h}}(\overline{\xi}_p, \overline{\eta}_p)^T \boldsymbol{\mathcal{H}} \quad \text{or} \quad \boldsymbol{h}(r_p, s_p) = \boldsymbol{\mathcal{H}}^T \overline{\boldsymbol{h}}(\overline{\xi}_p, \overline{\eta}_p) \tag{74}$$

It is easy to recognize that Eq. (74) coincides with the compatibility condition expressed by Eq. (25) in Section 2.3.1 if and only if $\xi_p = \overline{\xi}_p \quad \text{and} \quad \eta_p = \overline{\eta}_p$. This demonstrates that the inter-element compatibility condition given by Eq. (25) is equivalent to requiring that the point $\bar{P}$ coincides with point P in the (ξ, η) space.

APPENDIX B

ERROR FUNCTION COEFFICIENTS OF $\mathcal{E}^{\square}$, AND $\mathcal{E}^{\triangle}$

$$
\begin{aligned}
A_1 = &(r_a\,s_a - r_a\,s_b - r_b\,s_a + r_a\,s_c + r_b\,s_b + r_c\,s_a - r_a\,s_d - r_b\,s_c - \\
&\ r_c\,s_b\ - r_d\,s_a + r_b\,s_d + r_c\,s_c + r_d\,s_b - r_c\,s_d - r_d\,s_c + r_d\,s_d)\ \xi_p^2 + \\
&-2\ (r_a\,s_a - r_b\,s_b - r_a\,s_d + r_b\,s_c + r_c\,s_b - r_d\,s_a - r_c\,s_c + r_d\,s_d)\ \xi_p + \\
&(r_a\,s_a + r_a\,s_b + r_b\,s_a - r_a\,s_c + r_b\,s_b - r_c\,s_a - r_a\,s_d - r_b\,s_c - \\
&\ r_c\,s_b\ - r_d\,s_a - r_b\,s_d + r_c\,s_c - r_d\,s_b + r_c\,s_d + r_d\,s_c + r_d\,s_d)
\end{aligned} \tag{75}
$$

$$
A_2 = (r_a\,s_a - r_a\,s_b - r_b\,s_a + r_b\,s_b - r_c\,s_c + r_c\,s_d + r_d\,s_c - r_d\,s_d)\,(1 - \xi_p^2) \tag{76}
$$

$$
\begin{aligned}
A_3 = &(r_a\,s_a - r_a\,s_b - r_b\,s_a - r_a\,s_c + r_b\,s_b - r_c\,s_a + r_a\,s_d + r_b\,s_c + \\
&\ r_c\,s_b + r_d\,s_a - r_b\,s_d + r_c\,s_c - r_d\,s_b - r_c\,s_d - r_d\,s_c + r_d\,s_d)\ \xi_p^2 + \\
&+2\ (r_a\,s_a - r_b\,s_b - r_a\,s_d + r_b\,s_c + r_c\,s_b - r_d\,s_a - r_c\,s_c + r_d\,s_d)\ \xi_p \\
&(r_a\,s_b - 3\,r_a\,s_a + r_b\,s_a + r_a\,s_c - 3\,r_b\,s_b + r_c\,s_a + r_a\,s_d + r_b\,s_c + \\
&\ r_c\,s_b + r_d\,s_a + r_b\,s_d - 3\,r_c\,s_c + r_d\,s_b + r_c\,s_d + r_d\,s_c - 3\,r_d\,s_d)
\end{aligned} \tag{77}
$$

$$
B_1 = r_a\,s_a - r_a\,s_c - r_c\,s_a + r_c\,s_c \tag{78}
$$

$$
\begin{aligned}
B_2 = &(r_a\,s_b - 2\,r_a\,s_a + r_b\,s_a + r_a\,s_c + r_c\,s_a - r_b\,s_c - r_c\,s_b)\ \xi_p + \\
&-(r_a\,s_a - r_a\,s_c - r_c\,s_a + r_c\,s_c)
\end{aligned} \tag{79}
$$

$$
B_3 = (r_a\,s_a - r_a\,s_b - r_b\,s_a + r_b\,s_b)\ (\xi_p - 1)\,\xi_p \tag{80}
$$

REFERENCES

[1] Aalami, B., "Waves in prismatic guides of arbitrary cross section," *Journal of Applied Mechanics*, vol. 40, p. 1067, 1973.

[2] Aarnes, J., "On the use of a mixed multiscale finite element method for greaterflexibility and increased speed or improved accuracy in reservoir simulation," *Multiscale Modeling & Simulation*, vol. 2, p. 421, 2004.

[3] Aarnes, J., Krogstad, S., and Lie, K., "A hierarchical multiscale method for two-phase flow based upon mixed finite elements and nonuniform coarse grids," *Multiscale Modeling and Simulation*, vol. 5, no. 2, p. 337, 2006.

[4] Achenbach, J., *Wave propagation in elastic solids*. North-Holland Netherlands, 1984.

[5] Adams, R., Comyn, J., and Wake, W., *Structural adhesive joints in engineering*. Springer, 1997.

[6] Al-Nassar, Y., Datta, S., and Shah, A., "Scattering of lamb waves by a normal rectangular strip weldment," *Ultrasonics*, vol. 29, no. 2, pp. 125–132, 1991.

[7] Alleyne, D. and Cawley, P., "A two-dimensional fourier transform method for the measurement of propagating multimode signals," *The Journal of the Acoustical Society of America*, vol. 89, p. 1159, 1991.

[8] Alleyne, D. and Cawley, P., "The interaction of lamb waves with defects," *Ultrasonics, Ferroelectrics and Frequency Control, IEEE Transactions on*, vol. 39, no. 3, pp. 381–397, 1992.

[9] Alleyne, D. and Cawley, P., "Optimization of lamb wave inspection techniques," *Ndt & E International*, vol. 25, no. 1, pp. 11–22, 1992.

[10] Alleyne, D., Lowe, M., and Cawley, P., "The reflection of guided waves from circumferential notches in pipes," *Journal of Applied Mechanics*, vol. 65, p. 635, 1998.

[11] Amestoy, P. R., Duff, I. S., Koster, J., and L'Excellent, J.-Y., "A fully asynchronous multifrontal solver using distributed dynamic scheduling," *SIAM Journal on Matrix Analysis and Applications*, vol. 23, no. 1, pp. 15–41, 2001.

[12] Amestoy, P. R., Guermouche, A., L'Excellent, J.-Y., and Pralet, S., "Hybrid scheduling for the parallel solution of linear systems," *Parallel Computing*, vol. 32, no. 2, pp. 136–156, 2006.

[13] Armero, F. and Garikipati, K., "An analysis of strong discontinuities in multiplicative finite strain plasticity and their relation with the numerical simulation of strain localization in solids," *International Journal of Solids and Structures*, vol. 33, no. 20, pp. 2863–2885, 1996.

[14] Babuska, I., "Homogenization and its application- mathematical and computational problems(partial differential equation solutions for diffusion and composite material analysis)," *Numerical solution of partial differential equations-III*, pp. 89–116, 1976.

[15] Babuska, I., "The computational aspects of the homogenization problem," *Computing Methods in Applied Sciences and Engineering, 1977, I*, pp. 309–316, 1979.

[16] Babuska, I., Banerjee, U., and Osborn, J., "Generalized finite element methods: main ideas, result sand perspective," *International Journal of Computational Methods*, vol. 1, pp. 67–103, 2004.

[17] Babuška, I. and Osborn, J., "Generalized finite element methods: their performance and their relation to mixed methods," *SIAM Journal on Numerical Analysis*, pp. 510–536, 1983.

[18] Bakhvalov, N., Panasenko, G., and Eglit, M., "The effective properties of structures and composites with inclusions in the form of walls and rods," *Computational mathematics and mathematical physics*, vol. 36, no. 12, pp. 1701–1706, 1996.

[19] Balasubramanyam, R., Quinney, D., Challis, R., and Todd, C., "A finite-difference simulation of ultrasonic lamb waves in metal sheets with experimental verification," *Journal of Physics D: Applied Physics*, vol. 29, p. 147, 1996.

[20] Belytschko, T. and Black, T., "Elastic crack growth in finite elements with minimal remeshing," *International Journal for Numerical Methods in Engineering*, vol. 45, no. 5, pp. 601–620, 1999.

[21] Belytschko, T. and Fish, J., "Embedded hinge lines for plate elements," *Computer methods in applied mechanics and engineering*, vol. 76, no. 1, pp. 67–86, 1989.

[22] Belytschko, T., Fish, J., and Bayliss, A., "The spectral overlay on finite elements for problems with high gradients," *Computer Methods in Applied Mechanics and Engineering*, vol. 81, no. 1, pp. 71–89, 1990.

[23] Belytschko, T., Fish, J., and Engelmann, B., "A finite element with embedded localization zones," *Computer Methods in Applied Mechanics and Engineering*, vol. 70, no. 1, pp. 59–89, 1988.

[24] Belytschko, T., Moës, N., Usui, S., and Parimi, C., "Arbitrary discontinuities in finite elements," *International Journal for Numerical Methods in Engineering*, vol. 50, no. 4, pp. 993–1013, 2001.

[25] Bensoussan, A., Lions, J., and Papanicolaou, G., *Asymptotic analysis for periodic structures*, vol. 5. North Holland, 1978.

[26] Bloch, F., "Über die quantenmechanik der elektronen in kristallgittern," *Z. Physik*, no. 52, pp. 555–600, 1928.

[27] Bond, L., "Numerical techniques and their use to study wave propagation and scattering- a review," *Elastic waves and ultrasonic nondestructive evaluation*, pp. 17–27, 1990.

[28] Bragg, W., "The diffraction of short electromagnetic waves by a crystal," in *Proceedings of the Cambridge Philosophical Society*, vol. 17, pp. 43–57, 1913.

[29] Brasile, S., Casciaro, R., and Formica, G., "Multilevel approach for brick masonry walls-part i: A numerical strategy for the nonlinear analysis," *Computer Methods in Applied Mechanics and Engineering*, vol. 196, no. 49-52, pp. 4934–4951, 2007.

[30] Brillouin, L., *Wave propagation in periodic structures electric filters and crystal lattices*. Dover Publications Inc., 1946.

[31] Casadei, F. and Ruzzene, M., "Frequency domain bridging method for wave propagation simulations in damaged structures," *Wave motion*, vol. 49, no. 6, 2012.

[32] Casadei, F., Ruzzene, M., Dozio, L., and Cunefare, K., "Broadband vibration control through periodic arrays of resonant shunts: experimental investigation on plates," *Smart Materials and Structures*, vol. 19, p. 015002, 2010.

[33] Ce, M., "Finite element modeling of guided wave propagation in composite laminates for structural health monitoring applications," Master's thesis, Politecnico di Milano, 2012.

[34] Chen, W. and Fish, J., "A dispersive model for wave propagation in periodic heterogeneous media based on homogenization with multiple spatial and temporal scales," *Journal of applied mechanics*, vol. 68, p. 153, 2001.

[35] Chen, Z. and Hou, T., "A mixed multiscale finite element method for elliptic problems with oscillating coefficients," *Mathematics of Computation*, vol. 72, no. 242, pp. 541–576, 2003.

[36] Cho, Y. and Rose, J., "A boundary element solution for a mode conversion study on the edge reflection of lamb waves," *The Journal of the Acoustical Society of America*, vol. 99, p. 2097, 1996.

[37] Cho, Y. and Rose, J., "An elastodynamic hybrid boundary element study for elastic guided wave interactions with a surface breaking defect," *International journal of solids and structures*, vol. 37, no. 30, pp. 4103–4124, 2000.

[38] Cook, R. D., Malkus, D. S., Plesha, M. E., and Witt, R. J., *Concepts and Applications of Finite Element Analysis*. John Wiley & Sons, 2007.

[39] Diligent, O., Grahn, T., Boström, A., Cawley, P., and Lowe, M., "The low-frequency reflection and scattering of the s lamb mode from a circular through-thickness hole in a plate: Finite element, analytical and experimental studies," *The Journal of the Acoustical Society of America*, vol. 112, p. 2589, 2002.

[40] Diligent, O. and Lowe, M., "Reflection of the s lamb mode from a flat bottom circular hole," *The Journal of the Acoustical Society of America*, vol. 118, p. 2869, 2005.

[41] DOLBOW, J. and BELYTSCHKO, T., "A finite element method for crack growth without remeshing," *Int. J. Numer. Meth. Engng*, vol. 46, pp. 131–150, 1999.

[42] Efendiev, Y., Ginting, V., Hou, T., and Ewing, R., "Accurate multiscale finite element methods for two-phase flow simulations," *Journal of Computational Physics*, vol. 220, no. 1, pp. 155–174, 2006.

[43] Farhat, C., Harari, I., and Franca, L., "The discontinuous enrichment method," *Computer methods in applied mechanics and engineering*, vol. 190, no. 48, pp. 6455–6479, 2001.

[44] Fish, J. and Belsky, V., "Multi-grid method for periodic heterogeneous media part 2: Multiscale modeling and quality control in multidimensional case," *Computer Methods in Applied Mechanics and Engineering*, vol. 126, no. 1-2, pp. 17–38, 1995.

[45] Fish, J. and Belytschko, T., "Elements with embedded localization zones for large deformation problems," *Computers & Structures*, vol. 30, no. 1-2, pp. 247–256, 1988.

[46] Fish, J. and Chen, W., "Higher-order homogenization of initial/boundary-value problem," *Journal of engineering mechanics*, vol. 127, no. 12, pp. 1223–1230, 2001.

[47] Fish, J. and Chen, W., "Higher-order homogenization of initial/boundary-value problem," *Journal of engineering mechanics*, vol. 127, no. 12, pp. 1223–1230, 2001.

[48] Fish, J. and Chen, W., "Rve-based multilevel method for periodic heterogeneous media with strong scale mixing," *Journal of engineering mathematics*, vol. 46, no. 1, pp. 87–106, 2003.

[49] Fish, J., Chen, W., and Nagai, G., "Non-local dispersive model for wave propagation in heterogeneous media: multi-dimensional case," *International Journal for Numerical Methods in Engineering*, vol. 54, no. 3, pp. 347–363, 2002.

[50] Fish, J., Chen, W., and Nagai, G., "Non-local dispersive model for wave propagation in heterogeneous media: one-dimensional case," *International Journal for Numerical Methods in Engineering*, vol. 54, no. 3, pp. 331–346, 2002.

[51] Fish, J. and Wagiman, A., "Multiscale finite element method for a locally nonperiodic heterogeneous medium," *Computational mechanics*, vol. 12, no. 3, pp. 164–180, 1993.

[52] Fromme, P., *Defect detection in plates using guided waves*. PhD thesis, Swiss Federal Institute of Technology, 2001.

[53] Galan, J. and Abascal, R., "Numerical simulation of lamb wave scattering in semi-infinite plates," *Journal of Sound Numerical Methods in Engineering*, vol. 53, no. 3, pp. 1145–1173, 2002.

[54] George, P., *Automatic mesh generation: applications to finite element methods*. John Wiley & Sons, Inc., 1992.

[55] Ghosh, S., Lee, K., and Raghavan, P., "A multi-level computational model for multi-scale damage analysis in composite and porous materials," *International Journal of Solids and Structures*, vol. 38, no. 14, pp. 2335–2385, 2001.

[56] Gibson, L. and Ashby, M., *Cellular solids: structure and properties*. Cambridge Univ Pr, 1999.

[57] Gifford Jr, N. and Hilton, P., "Stress intensity factors by enriched finite elements," *Engineering Fracture Mechanics*, vol. 10, no. 3, pp. 485–496, 1978.

[58] Gonella, S. and Ruzzene, M., "Bridging scales analysis of wave propagation in heterogeneous structures with imperfections," *Wave Motion*, vol. 45, no. 4, pp. 481–497, 2008.

[59] Guedes, J. and Kikuchi, N., "Preprocessing and postprocessing for materials based on the homogenization method with adaptive finite element methods," *Computer Methods in Applied Mechanics and Engineering*, vol. 83, no. 2, pp. 143–198, 1990.

[60] Guyan, R., "Reduction of stiffness and mass matrices," *AIAA journal*, vol. 3, no. 2, p. 380, 1965.

[61] Hou, T. and Wu, X., "A multiscale finite element method for elliptic problems in composite materials and porous media," *Journal of computational physics*, vol. 134, no. 1, pp. 169–189, 1997.

[62] Hou, T., Wu, X., and Cai, Z., "Convergence of a multiscale finite element method for elliptic problems with rapidly oscillating coefficients," *Math. Comp.*, vol. 227, no. 68, pp. 913–943, 1999.

[63] Hussein, M., "Reduced bloch mode expansion for periodic media band structure calculations," *Proceedings of the Royal Society A: Mathematical, Physical and Engineering Science*, vol. 465, no. 2109, pp. 2825–2848, 2009.

[64] Ibrahimbegović, A. and Markovič, D., "Strong coupling methods in multiphase and multi-scale modeling of inelastic behavior of heterogeneous structures," *Computer methods in applied mechanics and engineering*, vol. 192, no. 28, pp. 3089–3107, 2003.

[65] Ihlenburg, F. and Babuska, I., "Solution of helmholtz problems by knowledge-based fem," *Computer Assisted Mechanics and Engineering Sciences*, vol. 4, pp. 397–416, 1997.

[66] Jirousek, J. and Wroblewski, A., "T-elements: state of the art and future trends," *Archives of Computational Methods in Engineering*, vol. 3, no. 4, pp. 323–434, 1996.

[67] Kadowaki, H. and Liu, W., "Bridging multi-scale method for localization problems," *Computer methods in applied mechanics and engineering*, vol. 193, no. 30-32, pp. 3267–3302, 2004.

[68] Kanouté, P., Boso, D., Chaboche, J., and Schrefler, B., "Multiscale methods for composites: a review," *Archives of Computational Methods in Engineering*, vol. 16, no. 1, pp. 31–75, 2009.

[69] Karim, M., Awal, M., and Kundu, T., "Elastic wave scattering by cracks and inclusions in plates: in-plane case," *International journal of solids and structures*, vol. 29, no. 19, pp. 2355–2367, 1992.

[70] Khelif, A., Aoubiza, B., Mohammadi, S., Adibi, A., and Laude, V., "Complete band gaps in two-dimensional phononic crystal slabs," *Physical Review E*, vol. 74, no. 4, p. 046610, 2006.

[71] Kita, E. and Kamiya, N., "Trefftz method: an overview," *Advances in Engineering Software*, vol. 24, no. 1, pp. 3–12, 1995.

[72] Koshiba, M., Karakida, S., and Suzuki, M., "Finite-element analysis of lamb wave scattering in an elastic plate waveguide," *IEEE transactions on sonics and ultrasonics*, vol. 31, no. 1, pp. 18–25, 1984.

[73] Laghrouche, O. and Bettess, P., "Short wave modelling using special finite elements," *Journal of Computational Acoustics*, vol. 8, no. 1, pp. 189–210, 2000.

[74] Langley, R., "The response of two-dimensional periodic structures to point harmonic forcing," *Journal of sound and vibration*, vol. 197, no. 4, pp. 447–469, 1996.

[75] Lions, J., "Some methods of resolution of free surface problems," in *Proceedings of the Fifth International Conference on Numerical Methods in Fluid Dynamics June 28–July 2, 1976 Twente University, Enschede*, pp. 1–31, Springer, 1976.

[76] Liu, G. and Achenbach, J., "A strip element method for stress analysis of anisotropic linearly elastic solids," *Journal of applied mechanics*, vol. 61, p. 270, 1994.

[77] Liu, G. and Achenbach, J., "Strip element method to analyze wave scattering by cracks in anisotropic laminated plates," *Journal of applied mechanics*, vol. 62, p. 607, 1995.

[78] Liu, G., Xi, Z., Lam, K., and Shang, H., "A strip element method for analyzing wave scattering by a crack in an immersed composite laminate," *Journal of applied mechanics*, vol. 66, p. 898, 1999.

[79] Liu, W., Park, H., Qian, D., Karpov, E., Kadowaki, H., and Wagner, G., "Bridging scale methods for nanomechanics and materials," *Computer methods in applied mechanics and engineering*, vol. 195, no. 13-16, pp. 1407–1421, 2006.

[80] Liu, W., Zhang, Y., and Ramirez, M., "Multiple scale finite element methods," *International Journal for Numerical Methods in Engineering*, vol. 32, no. 5, pp. 969–990, 1991.

[81] Lowe, M., Cawley, P., Kao, J., and Diligent, O., "The low frequency reflection characteristics of the fundamental antisymmetric lamb wave a from a rectangular notch in a plate," *The Journal of the Acoustical Society of America*, vol. 112, p. 2612, 2002.

[82] Lowe, M. and Diligent, O., "Low-frequency reflection characteristics of the s lamb wave from a rectangular notch in a plate," *The Journal of the Acoustical Society of America*, vol. 111, p. 64, 2002.

[83] MacNeal, R. and Harder, R., "A proposed standard set of problems to test finite element accuracy," *Finite Elements in Analysis and Design*, vol. 1, no. 1, pp. 3–20, 1985.

[84] Martinsson, P., *Fast multiscale methods for lattice equations*. PhD thesis, University of texas at Austin, 2002.

[85] Martinsson, P. and Movchan, A., "Vibrations of lattice structures and phononic band gaps," *The Quarterly Journal of Mechanics and Applied Mathematics*, vol. 56, no. 1, p. 45, 2003.

[86] Martinsson, P. and Rodin, G., "Asymptotic expansions of lattice green's functions," *Proceedings of the Royal Society of London. Series A: Mathematical, Physical and Engineering Sciences*, vol. 458, no. 2027, p. 2609, 2002.

[87] McDevitt, T., *Elastodynamics and Wave Propagation in Periodic Structures*. PhD thesis, University of Michigan, 1998.

[88] McDevitt, T., Hulbert, G., and Kikuchi, N., "Plane harmonic wave propagation in three-dimensional composite media," *Finite elements in analysis and design*, vol. 33, no. 4, pp. 263–282, 1999.

[89] McDevitt, T., Hulbert, G., and Kikuchi, N., "An assumed strain method for the dispersive global-local modeling of periodic structures," *Computer methods in applied mechanics and engineering*, vol. 190, no. 48, pp. 6425–6440, 2001.

[90] Melenk, J. and Babuška, I., "The partition of unity finite element method: basic theory and applications," *Computer methods in applied mechanics and engineering*, vol. 139, no. 1, pp. 289–314, 1996.

[91] Michaels, J., Hall, J., and Michaels, T., "Adaptive imaging of damage from changes in guided wave signals recorded from spatially distributed arrays," in *Proceedings of SPIE*, vol. 7295, pp. 729515–1, 2009.

[92] Michaels, T., Michaels, J., and Ruzzene, M., "Frequency–wavenumber domain analysis of guided wavefields," *Ultrasonics*, vol. 51, no. 4, pp. 452–466, 2011.

[93] Mohammadi, S., Eftekhar, A., Khelif, A., Hunt, W., and Adibi, A., "Evidence of large high frequency complete phononic band gaps in silicon phononic crystal plates," *Applied Physics Letters*, vol. 92, no. 22, pp. 221905–221905, 2008.

[94] Moser, F., Jacobs, L., and Qu, J., "Modeling elastic wave propagation in waveguides with the finite element method," *NDT & E International*, vol. 32, pp. 225–234, 1999.

[95] Mote Jr, C., "Global-local finite element," *International Journal for Numerical Methods in Engineering*, vol. 3, no. 4, pp. 565–574, 1971.

[96] Moulin, E., Assaad, J., Delebarre, C., and Osmont, D., "Modeling of lamb waves generated by integrated transducers in composite plates using a coupled finite element–normal modes expansion method," *The Journal of the Acoustical Society of America*, vol. 107, p. 87, 2000.

[97] Movchan, A., Movchan, N., and Haq, S., "Localised vibration modes and stop bands for continuous and discrete periodic structures," *Materials Science and Engineering: A*, vol. 431, no. 1-2, pp. 175–183, 2006.

[98] Murakami, H., "A mixture theory for wave propagation in angle-ply laminates, part 1: theory," *Journal of applied mechanics*, vol. 52, p. 331, 1985.

[99] Murakami, H. and Akiyama, A., "A mixture theory for wave propagation in angle-ply laminates, part 2: application," *Journal of applied mechanics*, vol. 52, p. 338, 1985.

[100] Murakami, H. and Hegemier, G., "A mixture model for unidirectionally fiber-reinforced composites," *Journal of applied mechanics*, vol. 53, p. 765, 1986.

[101] Newmark, N., "A method of computation for structural dynamics," *J. Eng. Mech.*, vol. 85, pp. 67–94, 1959.

[102] Noor, A., "Global-local methodologies and their application to nonlinear analysis," *Finite Elements in Analysis and Design*, vol. 2, no. 4, pp. 333–346, 1986.

[103] Oden, J., Vemaganti, K., and Moës, N., "Hierarchical modeling of heterogeneous solids," *Computer Methods in Applied Mechanics and Engineering*, vol. 172, no. 1-4, pp. 3–25, 1999.

[104] Palencia, E., *Non-homogeneous media and vibration theory*. Springer-Verlag, 1980.

[105] Paz, M., "Dynamic condensation," *AIAA journal*, vol. 22, no. 5, pp. 724–727, 1984.

[106] Pennec, Y., Djafari-Rouhani, B., Larabi, H., Vasseur, J., and Hladky-Hennion, A., "Low-frequency gaps in a phononic crystal constituted of cylindrical dots deposited on a thin homogeneous plate," *Physical Review B*, vol. 78, no. 10, p. 104105, 2008.

[107] Phani, A., Woodhouse, J., and Fleck, N., "Wave propagation in two-dimensional periodic lattices," *J. Acoustical Soc. Am.*, vol. 4, no. 119, pp. 1995–2005, 2006.

[108] Plum, E., Zhou, J., Dong, J., Fedotov, V., Koschny, T., Soukoulis, C., and Zheludev, N., "Metamaterial with negative index due to chirality," *Physical Review B*, vol. 79, no. 3, p. 035407, 2009.

[109] Psarobas, I. E., *Phononic crystals: sonic band-gap materials*. Zeitschrift fur Kristallographie, 2005.

[110] Rose, J., "A baseline and vision of ultrasonic guided wave inspection potential," *J. Pressure Vessel Technology*, vol. 124, no. 3, pp. 273–282, 2002.

[111] Ruzzene, M., "Frequency-wavenumber domain filtering for improved damage visualization," *Smart Materials and Structures*, vol. 16, no. 6, p. 2116, 2007.

[112] Ruzzene, M. and Scarpa, F., "Directional and band-gap behavior of periodic auxetic lattices," *physica status solidi (b)*, vol. 242, no. 3, pp. 665–680, 2005.

[113] Ruzzene, M., Scarpa, F., and Soranna, F., "Wave beaming effects in two-dimensional cellular structures," *Smart materials and structures*, vol. 12, p. 363, 2003.

[114] Senesi, M., Xu, B., and Ruzzene, M., "Experimental characterization of periodic frequency-steerable arrays for structural health monitoring," *Smart Materials and Structures*, vol. 19, p. 055026, 2010.

[115] Simo, J., Oliver, J., and Armero, F., "An analysis of strong discontinuities induced by strain-softening in rate-independent inelastic solids," *Computational Mechanics*, vol. 12, no. 5, pp. 277–296, 1993.

[116] Simulia Inc., *Abaqus Analysis User's Manual. Version 6.11-1.*

[117] Spadoni, A., Ruzzene, M., Gonella, S., and Scarpa, F., "Phononic properties of hexagonal chiral lattices," *Wave Motion*, vol. 46, no. 7, pp. 435–450, 2009.

[118] Staszewski, W., Boller, C., and Tomlinson, G., *Health monitoring of aerospace structures*. Wiley Online Library, 2004.

[119] Strouboulis, T., Copps, K., and Babuska, I., "The generalized finite element method: an example of its implementation and illustration of its performance," *International Journal for Numerical Methods in Engineering*, vol. 47, no. 8, pp. 1401–1417, 2000.

[120] Strouboulis, T., Copps, K., and Babuška, I., "The generalized finite element method," *Computer Methods in Applied Mechanics and Engineering*, vol. 190, no. 32, pp. 4081–4193, 2001.

[121] Sukhovich, A., Jing, L., and Page, J., "Negative refraction and focusing of ultrasound in two-dimensional phononic crystals," *Physical Review B*, vol. 77, no. 1, p. 014301, 2008.

[122] Sun, C., Achenbach, J., and Herrmann, G., "Continuum theory for a laminated medium," ASME, American Society of Mechanical Engineers, 1968.

[123] Verdict, G., Gien, P., and Burger, C., "Finite element study of lamb wave interactions with holes and through thickness defects in thin metal plates," in *Review of Progress in Quantitative Nondestructive Evaluation. Vol. 11B*, vol. 11, pp. 97–104, 1992.

[124] Wagner, G. and Liu, W., "Coupling of atomistic and continuum simulations using a bridging scale decomposition," *Journal of Computational Physics*, vol. 190, no. 1, pp. 249–274, 2003.

[125] Wolfe, J., *Imaging phonons: acoustic wave propagation in solids*. Cambridge Univ Pr, 1998.

[126] Worden, K., Manson, G., and Allman, D., "Experimental validation of a structural health monitoring methodology: Part i. novelty detection on a laboratory structure," *Journal of Sound and Vibration*, vol. 259, no. 2, pp. 323–343, 2003.

[127] Wu, T., Huang, Z., Tsai, T., and Wu, T., "Evidence of complete band gap and resonances in a plate with periodic stubbed surface," *Applied Physics Letters*, vol. 93, p. 111902, 2008.

[128] Wu, T.-C., Wu, T.-T., and Hsu, J.-C., "Waveguiding and frequency selection of lamb waves in a plate with a periodic stubbed surface," *Phys. Rev. B*, vol. 79, p. 104306, 2009.

[129] Zgonc, K. and Achenbach, J., "A neural network for crack sizing trained by finite element calculations," *NDT & E International*, vol. 29, no. 3, pp. 147–155, 1996.

[130] Zhang, H., Wu, J., and Fu, Z., "Extended multiscale finite element method for mechanical analysis of periodic lattice truss materials," *International Journal for Multiscale Computational Engineering*, vol. 8, no. 6, 2010.

[131] Zhang, H., Wu, J., Lü, J., and Fu, Z., "Extended multiscale finite element method for mechanical analysis of heterogeneous materials," *Acta Mechanica Sinica*, vol. 26, no. 6, pp. 899–920, 2010.

[132] Zhang, H., Wu, J., and Lv, J., "A new multiscale computational method for elasto-plastic analysis of heterogeneous materials," *Computational Mechanics*, pp. 1–21, 2012.

[133] Zhao, X. and Rose, J., "Boundary element modeling for defect characterization potential in a wave guide," *International journal of solids and structures*, vol. 40, no. 11, pp. 2645–2658, 2003.